

Hydrodynamics and Transient Heat Transfer Characteristics in Fluidized and Spouted Beds

Steven L. Brown

Thesis submitted to the Faculty of the
Virginia Polytechnic Institute and State University
in partial fulfillment of the requirements for the degree of

Master of Science
in
Mechanical Engineering

Brian Y. Lattimer, Chair
Srinath V. Ekkad
Mark A. Pierson

June 21, 2012
Blacksburg, VA

Keywords: Fluidization, Heat Transfer, Hydrodynamics, Multiple Jets, Spouted Bed

Hydrodynamics and Transient Heat Transfer Characteristics in Fluidized and Spouted Beds

Steven L. Brown

Abstract

Hydrodynamics and heat transfer characteristics found in fluidization were studied in a small scale laboratory fluidized bed. Experiments were designed to capture field data on multiple slit jet gas distributor systems for the validation of computational models. Localized data was quantified through the use of several novel non-intrusive experimental measurement techniques. The analyses provide a unique study that connects full field-of-view multiphase flow dynamics with transient heat transfer distributions.

The gas-solid hydrodynamics were captured through three non-invasive measurement techniques, viz. Particle Image Velocimetry (PIV), Digital Image Analysis (DIA), and pressure drop spectral analysis. The effects of inlet gas flowrate, Geldart B and D classified particle types, and the number inlet gas slit jets were investigated. Frequency analysis of a differential pressure signal resulted in the classification of four difference flow regimes. The coupling of PIV with DIA captured particle velocity, solid circulation rates, average cycle times, dead zone sizes, jet merging effects, gas void fraction distributions, and maximum expanded bed heights.

The heat transfer in fluidized and spouted beds containing a heated inlet gas source was studied through transient heat transfer measurements and analyses. Innovative experimental procedures were introduced to quantify bed-to-wall and gas-to-particle heat transfer characteristics. Two techniques were developed to overcome the spatial, time varying, and instrumental intrusive limitations often found in multiphase flow heat transfer studies. Infrared thermography was utilized along with derived discrete differential equations, and an inverse heat conduction analysis to solve for transient localized heat flux profiles and heat transfer coefficient distributions. As a result new data containing increased spatial resolution is presented on gas, wall, and particle temporal maps. Computations based from the thermal gradients quantified bed-to-wall heat flux profiles, gas-to-particle heat transfer coefficients, and localized rates of energy stored.

Acknowledgements

I would like express my sincere appreciation and thanks to my advisor Dr. Brian Lattimer for his guidance and encouragement in this work. I am also thankful to Dr. Srinath Ekkad, Dr. Mark Pierson, and Dr. Mary Kasarda for serving on my advisory committee. Their knowledge and support were unwavering over my graduate research. I would like to further express my gratitude all my teachers, friends, and colleagues for sharing their advice and insightful discussions.

I must also thank the Virginia Tech department of Mechanical Engineering, the Institute for Critical Technology and Applied Science (ICTAS), and the EXTREME Lab for the opportunity carry out the work in this thesis. My appreciation also goes to Dr. Francine Battaglia, Dr. Danesh Tafti, Dr. Uri Vandsburger, and fellow colleague in the Advanced Fuel Gasification Program for sharing their expertise.

Finally, I would like to express great thanks to my family. Their patience, support, and most of all, their never ending love has been most valuable throughout my life.

Contents

Abstract	iii
Acknowledgements	iii
Contents	iv
List of Figures	viii
List of Tables	xii
Chapter 1, General Introduction	1
1. Gas-Solid Fluidization	2
2. Motivation and Objective	3
3. Outline of Thesis.....	4
References.....	5
Chapter 2, Experimental Hydrodynamics of Multiple Jet Systems in a Fluidized and Spouted Bed	6
Abstract	6
1. Introduction.....	7
2. Experimental Setup.....	9
3. Measurement Techniques	11
3.1 Particle Image Velocimetry (PIV)	11
3.2 Digital Image Analysis (DIA).....	12
3.3 Bulk Solid Fractions	12
3.4 Solid Volume Fraction.....	13
3.5 Pressure Drop Spectral Analysis.....	14
4. Results and Discussion	15
4.1 Flow Regimes and Minimum Fluidization	15
4.2 Pressure Drop Spectral Analysis.....	18
4.3 Void Fraction Correlation	19

4.4 Fluidized Bed Void Fraction.....	20
4.5 Spouting Bed Void Fraction	21
4.5.1 Spout Zone	21
4.5.2 Annulus Region	22
4.5.3 Fountain Region.....	24
4.6 Dead Zones	25
4.7 Solid Circulation Rates	26
4.8 Fountain Heights.....	28
5. Conclusion	31
Acknowledgements.....	32
References.....	32
Figures and Tables	40
Chapter 3, Transient Bed-to-Wall Heat Flux Measurements in Fluidized and Spouted Beds	56
Abstract.....	56
1. Introduction.....	57
2. Experimental Setup.....	59
3. Data Analysis	61
4. Uncertainty Analysis.....	65
5. Variable Impact Discussion	65
5.1 Heat Flux Terms	65
5.1.1 Energy Stored.....	66
5.1.2 Lateral Conduction.....	66
6. Experimental Results and Discussion.....	68
6.1 Transient Heat Transfer Distribution	68
6.2 Flow Regimes	70

6.2.1 Single Jet.....	70
6.2.2 Double Jets.....	71
7. Conclusion	71
Acknowledgements.....	72
References.....	72
Figures and Tables	76
Chapter 4, Transient Gas-to-Particle Heat Transfer Measurements in Fluidized and Spouted Beds	87
Abstract.....	87
1. Introduction.....	88
2. Experimental Setup.....	90
3. Data Acquisition	91
3.1 Infrared Measurements	91
3.2 Emissivity and Transmission Calibration	92
3.3 Measurement Procedure.....	92
4. Data Analysis	93
5. Results and Discussion	94
5.1 Transient Temperature Distributions	94
5.2 Energy Stored	97
5.3 Gas-to-Particle Heat Transfer	98
5.3.1 Heat Transfer Coefficients.....	99
5.3.2 Heat Transfer Correlations.....	99
6. Conclusion	102
Acknowledgements.....	103
References.....	103

Figures and Tables 106

Chapter 5, Conclusions and Recommendations.....114

 1. Conclusions..... 115

 2. Recommendations..... 116

Appendix A, Additional Figures.....118

Appendix B, Publications and Presentations120

List of Figures

Chapter 2:

Figure 1: Schematic of the 2-D flat bottom rectangular column setup with dimensions in mm.	40
Figure 2: Diagram of the experimental setup.....	41
Figure 3: Corrected intensity, I_{cor} , averaged along the vertical height of the bed for 3G550 at $1.6\text{ }umf$ to define the expanded bed height.	42
Figure 4: Mean Prewitt high pass filtered PIV images of the various flow regimes: a) Fixed Bed, b) Internal Spout, c) Jet Fluidized, and d) Jet Spouting.	42
Figure 5: Differential pressure measurements for G550 using the pressure drop method to define the onset of the minimum fluidization velocity, umf	43
Figure 6: Differential pressure measurements for G750 using the pressure drop method to define the onset of the minimum fluidization velocity, umf	43
Figure 7: Dominant frequencies in the power spectrum from the differential pressure measurements used to classify the flow regimes: a) Fixed Bed and Internal Spout, b) Transition Jet Fluidized, c) Jet Fluidized, d) Jet Transition Spouting, and e) Jet Spouting.	44
Figure 8: Effect of superficial gas velocity on the dominant frequencies for the G550 multiple jet systems.	45
Figure 9: Expanded bed heights, h_{exp} , and bulk solid fractions, ϵ_s, b , for Case I and II as a function of G550 inlet gas velocities for: a) a single jet, b) double jet, and c) triple jet system.	46
Figure 10: Solid volume fraction, ϵ_s , correlation for G550 and G750 particulates classified in the jet fluidized regime in comparison to Equation 3.4.1.....	47
Figure 11: Localized mean gas void fraction, ϵ_f , distributions at $1.6\text{ }umf$, for: a) 1G550, b) 2G550, c) 3G550, d) 1G750, e) 2G750, and f) 3G750.....	48
Figure 12: Localized mean gas void fraction, ϵ_f , distributions at $3.0\text{ }umf$, for: a) 1G550, b) 2G550, c) 3G550, d) 1G750, e) 2G750, and f) 3G750.....	49
Figure 13: Instantaneous single jet I_{cor} image showing the annulus, spout, and fountain regions.	50
Figure 14: Axial gas void fraction, ϵ_f , distributions at $2.0\text{ }umf$ and a bed height of 19.2 mm above the distributor plate for one, two, and three jet G750 systems.	50

Figure 15: Axial gas void fraction, ϵ_f , distributions in the fountain region at 3.1 umf and bed heights of 104.7 mm, 110.0 mm, and 120.4 mm for 1G750.	51
Figure 16: Cross sectional averaged gas void fractions, ϵ_f , in the fountain region at 2.8 umf , 3.0 umf , and 3.1 umf	51
Figure 17: Mean Prewitt high passed filtered image over-laid with corresponding annulus velocity vectors at 3.1 umf	52
Figure 18: Dead zone mass fractions, η_{dz} , for G550 and G750 in one, two, and three jet systems.	52
Figure 19: Solid, $mtot$, and volumetric, $Vtot$, circulation rates for 1G550 and 1G750 in comparison with counter-current model of Equation 4.7.3	53
Figure 20: Average particle cycle times compared between neglecting and accounting for total dead zone mass.	53
Figure 21: Effect of superficial gas velocity on fountain height expansion ratios, η_{Hf} , A , defined from the top of the annulus, for G550 and G750 systems.	54
Figure 22: Experimental fountain height compared with the force balance analyses of Equations 4.8.3 and 4.8.4.	54
 Chapter 3:	
Figure 1: Schematic of the 2-D flat bottom rectangular column setup with dimensions in mm.	76
Figure 2: Diagram of the experimental setup.	77
Figure 3: Transient inlet air temperature ramp at 3 umf for a single jet with glass particles of $D_p = 550 \mu m$	78
Figure 4: Differential control volume for the paint layer and stainless steel plate.	78
Figure 5: Normalized bed-to-wall heat flux data a) without filtration and b) with filtration for a single jet fluidized bed.	79
Figure 6: Mean Prewitt high pass filtered PIV images illustrating an a) internal spout, b) multiple jet fluidized bed, and c) a single jet spouting bed.	80
Figure 7: Effects of neglecting lateral conduction and the paint layer on Equation 3.2 in a single jet, G550, fluidized bed at 1.6 umf and $t = 19$ seconds.	81
Figure 8: Instantaneous PIV image illustrating the various regions in a spouted bed.	82

Figure 9: Mean error in neglecting lateral conduction over a 60 second time span in a single jet, G550, spouted bed at 3 umf .	82
Figure 10: Transient time series bed-to-wall heat flux distributions of a single jet, G550, spouted bed at 3 umf .	83
Figure 11: Heat Flux interrogation areas: center (1), mid (2), and outer-wall (3) regions.	83
Figure 12: Normalized bed-to-wall heat flux distributions for a single jet system over 60 seconds.	84
Figure 13: Normalized bed-to-wall heat flux distributions for a double jet system over 60 seconds.	85
 Chapter 4:	
Figure 1: Schematic of the 2-D flat bottom rectangular column setup with dimensions in mm.	106
Figure 2: Diagram of the experimental setup.	107
Figure 3: Infrared camera calibration curve for the coupled particle emissivity and transmission of the sodium chloride optical window.	108
Figure 4: Transient inlet air temperature ramp for the spouted, fluidized, and fixed bed regimes.	108
Figure 5: Instantaneous void fraction data for the a) fluidized, and b) spouted regime.	109
Figure 6: Instantaneous particle time line temperature distribution in a fixed bed with an internal spout at 0.7 umf .	109
Figure 7: Instantaneous particle time line temperature distribution in a fluidized bed at 1.6 umf .	110
Figure 8: Instantaneous particle time line temperature distribution in a spouted bed at 3.0 umf .	110
Figure 9: 60 second time averaged dimensionless gas and particle temperature distribution in the spouted bed at 3.0 umf .	111
Figure 10: Instantaneous rates of energy stored in the particles under a fluidized regime at 1.6 umf .	111
Figure 11: Instantaneous rates of energy stored in the particles under a spouted regime at 3.0 umf .	112

Figure 12: 60 second time averaged gas-to-particle heat transfer coefficients per axial cross-sectional height in a spouted regime at 3.0 umf 112

Appendix:

Figure 1: Three dimensional illustration of the pseudo 2-D experimental bed examined. 118

Figure 2: Image of the inlet gas distribution system used in the hydrodynamic experiments of Chapter 2. 119

List of Tables

Chapter 2:

Table 1. Properties of experimental fluidized bed media. 55

Table 2. Minimum fluidization velocities found in literature for glass Geldart B and D particle classifications. 55

Chapter 3:

Table 1: Material properties. 86

Table 2: Properties of experimental fluidized bed media. 86

Table 3: Instrument resolution and material uncertainties. 86

Chapter 4:

Table 1: Properties of experimental fluidized bed media. 113

Chapter 1

General Introduction

The basic principles needed to understand gas-solid fluidization are given in this chapter. These fundamentals provide a background for the work performed in this thesis. The advantages of fluidization are described along with common industrial applications. The motivation and objective for this research are stated and an outline for the thesis is given.

1. Gas-Solid Fluidization

Fluidization is the process of transforming static, discrete solid particles into a dynamic structure that behaves like a fluid. This is accomplished by directing a gas or fluid upward through a bed of packed solid particles. The particles will begin to rearrange themselves to provide reduced resistance to the gas flow. With increased gas velocity the particles will overcome gravitational and frictional forces within the bed. At this point, the solids become suspended in the gas and behave like a fluid. The lowest gas flowrate required to achieve this phenomenon is called the minimum fluidization velocity. This process has many advantages in industrial applications.

Gas-solid fluidized beds are well known for their high mass transfer with vigorous mixing and high velocity distributions. A large surface area exists between the solids and gas. This allows for an increased heat transfer rate within the bed. Low temperature gradients result in homogenous gas distributed beds. As a consequence, the bed has a higher internal thermal conductivity allowing for high rates of heat transfer to immersed objects and bed walls.

The pattern to which the gas flow enters the bed of solids is controlled by the distributor plate. Local hydrodynamics of a fluidized bed are strongly dependent upon the design of this plate. Traditional fluidized beds consist of a porous plate distributor allowing for homogenous gas distribution. Contrarily, the use of a narrow slit jet results in increased gas concentration per a unit area. Thus, a localized high solid particulate entrainment rate can be achieved. At low gas flow rates a slit jet can exhibit fluidization characteristics. Further increasing the gas flowrate of a slit jet leads to a region comprised of an upward dilute phase core penetrating through the total height of the solid packed bed. This is a variation of fluidization known as spouting. This flow regime is beneficial when processing coarse, crystalline, or heat sensitive materials (Botterill, 1975).

Fluidized and spouted beds are found in a wide variety of multiphase flow industrial applications. The petroleum industry is well known for using these methods in catalytic cracking (FCC) (Mertinkat et al., 1999). This method breaks down hydrocarbons of high molecular weight found in crude oils through the use of a fluidized catalyst. The vigorous mixing and near isothermal capabilities of a fluidized bed also allows them to be used in coal and biomass gasification (Tsuji and Uemaki, 1994). Reacting carbonaceous materials at high temperatures

without combustion make it possible to produce synthesis gas. Fluidization is also utilized in granulation processes (Palis and Kienle, 2012), such as in the pharmaceutical or fertilizer industry. Other applications for fluidization vary from chemical processing, drying, mixing, coating, and pyrolysis.

2. Motivation and Objective

The advantages of gas-solid fluidization are well known in the previously mentioned industrial applications for its intense mixing ability and uniform temperature dispersal. Yet, many complications and obstacles exist when trying to scale up laboratory sized beds for industrial sized applications (Schouten et al., 1996). Detailed equations can be used to predict gas-solid hydrodynamic and thermal models. However, the numbers of calculations needed to characterize every parameter in a full-sized industrial scale bed is beyond the computational power of today. Instead, detailed information on dynamic structure of a small scaled fluidized bed can be used to help characterize larger scaled models.

Two types of Computational Fluid Dynamic (CFD) models are currently being developed to predict the gas-solid interactions in multiphase flow. The first is Discrete Particle Models (DPM). This model uses Newton's second law to account for the velocity distribution of each particle and the volume averaged Navier-Stokes equation to model the gas flow. Once DPM is developed, the established particle interaction closure relations can be applied to the second CFD model, Eulerian-Eulerian or Two Fluid Models (TFM). This model is based on the kinetic theory of granular flow by modeling the gas-solid phases as an interpenetrating continuum. Currently this model appears to have high potential for simulating industrial scale systems (Hernández-Jiménez et al., 2011). However, in order to further the development of TFM, the gas-solid interaction closure laws must first be supplied through DPM (Deen et al., 2007).

It is important to validate the DPM with quantifiable, accurate, and detailed experiments. CFD models are designed to provide computational data with high spatial resolution. Field data which is not limited to a few discrete measurement points is most often desired. In this research, several types of experiments were conducted to characterize the hydrodynamics between the two phases and the transient heat transfer characteristics. A pseudo two-dimensional laboratory size bed with multiple slit jets, shown in Appendix A, was examined due to the extensive

computational effort of DPM simulations and the limitation for visual observation. Each type of measurement was specifically designed to be non-intrusive to the gas-solid flow.

The parameters investigated were the effects of a multiple slit jet system, fluidization regimes, particle size, inlet gas velocity, and inlet gas temperature. A combination of Particle Image Velocimetry (PIV), Digital Image Analysis (DIA), pressure drop spectral analysis, and infrared thermography is utilized as non-invasive multiphase capturing techniques to quantify flow patterns and transient heat transfer characteristics.

3. Outline of Thesis

The thesis consists of a series of submitted journal articles. Each article provides details on specific aspects of the author's research.

The dynamics of a gas-solid system needs to be quantified for the validation of DPM. Therefore, Chapter 2 presents an experimental study to capture detailed hydrodynamics in a pseudo two-dimensional bed. The effects of multiple gas jet systems were measured by coupling three non-intrusive measurement techniques. Particle Image Velocimetry (PIV) was used to capture particle velocity data. Digital Image Analysis (DIA) was also applied to compute local gas void fractions, solid circulation rates, average bed cycle times, and maximum expanded bed heights. In addition, various flow regimes are identified through the use of pressure drop spectral analysis.

Detailed fluidization heat transfer characteristics are also required for CFD validations. Chapter 3 discusses an innovative measuring technique designed to overcome the spatial, time varying, and instrumental intrusive limitations of heat transfer measurements found in multiphase flow experiments. The 2-D bed hydrodynamics characterized in Chapter 2 are used with a non-invasive infrared thermometry measurement technique to capture bed-to-wall heat transfer characteristics. Attention is paid to the importance of the experimental design and to the data processing technique. Transient bed-to-wall heat flux distributions are mapped in the multiple jet system under spouted, fluidized, and fixed bed conditions.

Another important parameter to quantify in fluidization is particle temperature distributions. A novel infrared thermography technique is applied to capture gas-to-particle heat transfer characteristics in Chapter 4. The infrared energy is captured at a high spatial resolution, which does not disrupt the gas-solid flow, and was capable of capturing transient bed conditions.

Two-dimensional full field views of particle temperatures are mapped along with the rates of energy stored in the particulates. A discrete differential equation is introduced to compute gas temperature distributions and used to quantify convective gas-to-particle heat transfer coefficients. New spatially detailed heat transfer coefficients are introduced and compared to existing heat transfer models.

An overall conclusion on the findings from the multiphase hydrodynamics and heat transfer studies are then given in Chapter 5. A list of future recommendation for quantifying the gas-solid dynamics in fluidization is proposed. This is followed by the Appendix containing additional figures and a list of the author's publications and presentations relative to this work.

References

- Botterill, J.S.M., 1975. Fluid-bed heat transfer : gas-fluidized bed behaviour and its influence on bed thermal properties. Academic Press, London; New York.
- Deen, N.G., Van Sint Annaland, M., Van der Hoef, M.A., Kuipers, J.A.M., 2007. Review of discrete particle modeling of fluidized beds. *Chem Eng Sci* 62, 28-44.
- Hernández-Jiménez, F., Sánchez-Delgado, S., Gómez-García, A., Acosta-Iborra, A., 2011. Comparison between two-fluid model simulations and particle image analysis & velocimetry (PIV) results for a two-dimensional gas–solid fluidized bed. *Chem Eng Sci* 66, 3753-3772.
- Mertinkat, J., Kirsten, A., Predel, M., Kaminsky, W., 1999. Cracking catalysts used as fluidized bed material in the Hamburg pyrolysis process. *Journal of Analytical and Applied Pyrolysis* 49, 87-95.
- Palis, S., Kienle, A., 2012. Stabilization of continuous fluidized bed spray granulation with external product classification. *Chem Eng Sci* 70, 200-209.
- Schouten, J.C., Vander Stappen, M.L.M., Van Den Bleek, C.M., 1996. Scale-up of chaotic fluidized bed hydrodynamics. *Chem Eng Sci* 51, 1991-2000.
- Tsuji, T., Uemaki, O., 1994. Coal-Gasification in a Jet-Spouted Bed. *Can J Chem Eng* 72, 504-510.

Chapter 2

Experimental Hydrodynamics of Multiple Jet Systems in a Fluidized and Spouted Bed

Abstract

The coupling of Particle Image Velocimetry and Digital Image Analysis was used to quantify the gas-solid hydrodynamics in a 2-D flat bottom bed. Multiple jets systems were investigated pertaining to fluidized and spouting dynamics. Pressure drop spectral analysis resulted in the classification of four different flow regimes: Fixed Bed, Internal Spout, Jet Fluidized, and Jet Spouting. The effects of inlet gas flowrate, Geldart B and D classified particle types, and multiple jet systems were investigated for void fraction distributions and solid circulation rates. An increase in particulate size resulted in increasing jet diameters, solid circulation rates, and spouting fountain heights due to the enlarged momentum exchange rates. Gas voidage in the annulus was found higher than a loosely packed bed, contrary to the typical notion. Additionally, the common assumption of implementing additional jets did not always directly pertain to a decrease in total bed dead zones due to jet merging effects.

Submitted for review to the International Journal of Multiphase Flow, June 2012

Corresponding Author: Steven L. Brown

Co-Author: Brian Y. Lattimer

1. Introduction

Gas-solid fluidized beds are well known for their advantages in solid phase mixing, and intensive heat and mass transfer distribution which allow for near isothermal conditions. Fluidized and spouting beds have wide spread applications in multiphase processing, combustion, gasification (Tsuji and Uemaki, 1994; Yin et al., 2002), granulation (Palis and Kienle, 2012), catalytic pyrolysis (Bilbao et al., 1989) and chemical processing (Fayed and Otten). Advanced Computational Fluid Dynamic (CFD) programs are being developed to predict the dynamics of these systems. With the modern advancements in computational power, these multiphase flow models need to be fully validated with quantifiable, accurate, and detailed experiments.

Traditional fluidized beds consist of porous plate distributors allowing for homogenous gas distribution. Contrarily, spouting beds can provide high particulate entrainment through the use of a narrow slit jet. The resulting increased gas concentration per a unit area produces two well defined regions under stable spouting conditions. These regions entail an upward dilute phase core consisting of the gas-solid mixture and a quasi-static granular downward flow resulting from gravitational forces (Liu et al., 2008a). The ease of pressure measurements has allowed for time series (Sasic et al., 2006) and frequency domain analyses (Bi, 2007) to classify the various transitional flow regimes. However, even these experiments need to be validated through flow dynamic capturing measurements.

An early mathematical model of spouting was derived from a force balance analysis (Thorley et al., 1959) for predicting particle velocities. A mass and momentum balance equation was later applied to a cylindrical spout bed for equating solid circulation rates and axial voidage (Lefroy, 1969). The Euler equation has also been utilized to model gas-solid flow patterns in a spouted bed (Littman et al., 1985). The early experimental work of Mathur and Gishler (1955) used cine-photography to capture particle distributions and compute particle velocities in a cylindrical half column. Since then advancing measurement techniques have been applied to try to quantify gas-solid interactions.

Particle velocities have been captured through piezoelectric probes (Zhou et al., 1995) and fibre optics in spouted (He et al., 1994a) and fluidized (Morooka et al., 1980) beds. Resistance probes (Burgess and Calderbank, 1975) and other internal sensors have been utilized

to provide information on particle trajectories, average cycle time, void distributions, velocity vectors, etc. However these probes remain invasive to the flow.

Non-intrusive measurements techniques have consisted of laser (Sung and Burgess, 1987) and X-ray (Franka et al., 2007) measurements. Furthermore, Positron Emission Particle Tracking (PEPT) was performed by Roy et al. (1994) and van Buijtenen et al. (2011b) by tracking a limited number of particles at one time and computing solid circulation regimes from a statistical analysis. These techniques have provided beneficial data but are often limited by a field of view and consequently can be unsuitable for the precise full field validation of computational models.

A whole field optical technique was applied by Lim et al. (1990). In their study Digital Image Analysis (DIA) was applied to a two dimensional fluidized bed to capture bubble distribution characteristics. Later Goldschmidt et al. (2003) utilized a high speed color camera to capture the segregation rates of binary particles. The more recent studies of Bokkers et al. (2004) and Link et al. (2004) have applied Particle Image Velocimetry (PIV) in order to measure full field particle profiles in 2-D gas-solid fluidized beds. Typically PIV is used in fluid flow characterization but have been progressively used as an effective non-intrusive measurement technique in granular flow systems.

Combining PIV with DIA has made it possible to characterize entire 2-D field optical measurements with velocity profiles. This technique was applied to characterize the bubble and dense phases by Sánchez-Delgado et al. (2010) in a two dimensional fluidized bed. A similar setup was used by Laverman et al. (2008) with the combination of PIV and DIA to correct for the raining of particulates through the roof of the bubbles in time-averaged emulsion phase velocity profiles. More recent studies have successfully applied these techniques to quantify particle and jet interaction in the fluidized grid-zone region (Agarwal et al., 2011b). In addition to fluidized beds, this coupled measurement technique has also been applied to single jet spout fluidized (Link et al., 2004; van Buijtenen et al., 2011a) and single jet spouted beds (Liu and Litster, 1991; Zhao et al., 2008).

Laboratory scale fluidized bed have mainly focused on single vertical (Ruoyo et al., 1996; Sutanto et al., 1985) and horizontal (Hong et al., 1997; Wang et al., 2010) oriented jet spouts. However, there is a lack of experimental data within the literature pertaining to multiple jet systems to support the CFD validation of Euler-Lagrangian based simulations such as

Discrete Particle Model (DPM). Therefore the work in this study investigates the hydrodynamics of a single and multiple jet system. It combines the benefits of PIV, DIA, and pressure frequency analysis to yield detailed information about the gas-particulate dynamics under jet fluidized and spouting regimes. A two dimensional bed was examined due to the extensive computational effort of DPM simulations and the limitation for visual observation.

In addition to producing a study for DPM validation, a comparison between the flat-bottom rectangular column bed of this study and the single jet spouting beds commonly found in literature is given. Much contradiction can be found over gas void fraction distribution in jet spouted beds. It has been a common assumption that the void fraction within the annulus of a spouting bed is equal to that of a loosely packed bed (Mathur and Gishler, 1955; Thorley et al., 1959). However, Lim and Mathur (1974) found the annulus voidage to decrease with higher spouting gas velocities, while He et al. (1994a) concluded the void fraction is greater than a loosely packed bed. Again, the findings of Grbavcic et al. (1976) show a slight difference in void fraction per annulus locations. This makes it necessary to reexamine the voidage distributions using modern PIV and DIA in single and multiple spouts.

The paper is organized by first giving a detailed schematic of the experimental setup and explanation of the measurement techniques. This is followed by time series and pressure drop spectral analyses used to classify the dynamics of the bed into multiple flow regimes. A localized void fraction relationship is derived and is used with PIV velocity data to compute solid circulation rates. A comparison between annular and fountain spout geometries of a rectangular flat bottom bed to the typical studied conical based bed is then given.

2. Experimental Setup

The experiments were conducted in a pseudo-2D fluidized bed, shown in Figure 1, with cross-sectional dimensions of $W = 56.4$ mm, $D = 4.95$ mm and overall bed height, H , of 280 mm. The depth of the bed was six to nine times that of the particle diameters tested to prevent particle bridging effects (Grace and Li, 2010; Link et al., 2005) while the ratio of D/W was kept minimal to simulate a quasi-2D behavior. The 2-D assumption was experimentally examined by Freitas et al. (2004b) in a single jet slot-rectangular bed by varying the ratio of D/W . Significant particle mixing occurred in the third direction as the ratio increased. However, the work of Rao

et al. (2010) showed that this ratio needs to remain large enough to avoid particle bridging and excessive friction effects from the wall.

A schematic of the setup is given in Figure 2. The base entailed of a stainless steel distributor plate with three evenly spaced selectable slit jets of 1.6 mm wide by the full depth of the bed. The back and side walls consisted of Polymethyl-Methacrylate coated in a high emissivity paint to promote light absorption and ensure surface flatness, while the front wall comprised of high optical clarity glass. The area surrounding the freeboard was encompassed by a black body box to prevent external lighting reflections. Direct homogenous illumination was provided by two 500 Watt halogen lamps spaced at 45° angles from the front wall.

Compressed air was used as the fluidization gas and was controlled by a 50 SLPM ALICAT (Model # MC-50SLPM-D) mass flow controller with an accuracy of ($\pm 0.4\%$ reading, + 0.2% FS). The gas was first passed through a humidifier to reduce electrostatic effects. Then it was channeled through a plenum chamber and controlled by three rapidly responding solenoid valves providing the ability for various jet selections.

The pressure drop across the bed was measured with a Setra (Model # 264) differential pressure transducer (range of 0 – 25,000 Pa $\pm 0.25\%$ FS). The pressure taps were located at the jet inlets and in the freeboard, 174 mm upstream of the distributor plate. The differential pressure signal was sampled for 60 seconds at 250 Hz, well above the dominant frequency of a fluidized (Bi, 2007; van Ommen et al., 2011) or spout (Link et al., 2005) bed. The signal was then filtered through a low pass filter at 25 Hz to satisfy the Nyquist criterion, remove dc bias, and take away any noise associated with surrounding AC equipment. A 32 bit National Instrument cDAQ-9174 chassis was used with NI-9213 and NI-9205 cards to monitor individual inlet slot jet temperatures, pressures, and air flow rates.

The top of the distributor plate was covered by a fine mesh screen and the bed was filled with glass particles. Two types of particles were examined to explore the effects of particle size, fluidization velocity, and the number of slit jets used at the distributor plate. The particles pertained to the Geldart B and C classification with mean diameters, D_p , of 550 μm and 750 μm respectfully. The gas to solid void fraction ratio was experimentally determined for a packed bed and was found to be 0.38, which is in close comparison with the theoretical value of 0.4.

The minimum fluidization velocity, u_{mf} , for each particle type was then found by taking the bed past three times the estimated fluidization velocity, and then dropping the mass flowrate.

A period of 5 minutes was allowed before taking each data set. This measurement technique was applied to one, two, and three jet studies. The resulting minimum fluidization velocity, per a particle type, was found to be in close comparison. A single corresponding value for u_{mf} and the physical particle properties are given in Table 1.

3. Measurement Techniques

Three non-invasive techniques were applied in order to quantify the non-reacting hydrodynamics of the gas and solid interactions. Each technique is introduced in this section.

3.1 Particle Image Velocimetry (PIV)

PIV is a laser based imaging technique that combines the accuracy of non-intrusive measurements with flow imaging capability. Due to the high density of particles in a fluidized bed, traditional PIV laser passage is not viable. Instead a PIV CCD camera can be used with a triggering circuit to capture particle positions within specified time delays. PIV varies from Particle Tracking Velocimetry (PTV), as it does not track individual particles but rather computes a statistically averaged displacement per an Interrogation Area, IA . The technique behind this approach is to determine the volume averaged displacement, $s_p(x, t)$, of the particles in an IA . The particle velocities are then found by dividing the displacement by the time between sequential images, Δt , and the magnification factor, M .

$$\vec{v}_p = \frac{s_p(x, t)}{M\Delta t} \quad (3.1.1)$$

An adaptive correlation algorithm supplied through Dantec Dynamic Studio 3.20 software was used for the PIV analysis. This correlation is based on the cross-correlation technique and is equipped with spatio-temporal gradient sub-pixel analysis, discrete window offset, and peak validation. A Flowsense MKII (4 Megapixels) CCD camera was used to record double frame 12 bit images at a resolution of 2048 x 2048 pixels. The camera was located at a distance of 0.75 m from the front wall of the bed and provided a magnification factor of 5-7 pixels per particle. The frequency at which double frame images were captured was 7.4 Hz, while the time delay between the double frame images was 1 ms. A total of 148 images were captured per test condition providing 10 seconds of PIV data. The adaptive correlation analysis was then applied using a multiple-pass mode with an IA iteratively reducing from 128 x 128 pixels to 32 x 32 pixels. A peak validation of 1.2 was used along with a 50% relative IA overlap.

PIV analysis can be problematic when it is applied to studies where there are regions of significant velocity differences (Scarano, 2002). To deal with these issues Liu et al. (2008a) applied different PIV sampling techniques per experimental spouting bed regions (i.e. dead zones, annulus, spout, and fountain) to account for the errors in signal noise reduction and peak locking effects. In this study, multiple flow regimes are examined which contain substantial changes in the average velocity gradient. To deal with this issue, the time delay of the CCD camera was set to better capture velocity profiles within the annulus regions. The resulting velocity vectors in the jet regions were then masked.

3.2 Digital Image Analysis (DIA)

The principle behind using Digital Image Analysis is to use the captured PIV pixels intensities to correlate to the bulk solid, $\varepsilon_{s,b}$, and gas void, ε_f , fractions. The pixel values of the 12 bit images captured ranged from 0 (dark regions) to 4095 (bright regions). Each image was exported to MATLAB 2010b to obtain particle distribution profiles and time averaged solid volume fractions.

The DIA started by first loading the captured images into an intensity matrix. To remove the affects from inhomogeneous lighting a base image of the freeboard containing no solid particles was subtracted from the matrix. The resulting data was then filtered and passed through an edge detection algorithm in order to remove noise and crop the boundaries of the flow regime. The intensity values between instantaneous images were then normalized between 0 (gas phase) and 1 (solid phase), to produce a corrected intensity, I_{cor} , matrix.

3.3 Bulk Solid Fractions

The hydrodynamics of an experimental fluidized bed can be classified though the solid volume fractions. The advantages of using PIV analysis is the volume fraction can be characterized without disrupting the gas-solid flow. However, this technique is limited to capturing particle behavior at the front wall of the bed.

To account for the intensity of the particles blocked behind the particles at the front wall, a relationship between the two is needed. The mean intensity values obtained from DIA analysis can be used to account for the solid volume fraction through the depth of bed (Goldschmidt et al., 2003). The I_{cor} matrices were first time averaged per each bed velocity and then averaged per bed width. The expanded bed height, h_{exp} , was defined at 5% of the maximum bed height

intensity (Agarwal et al., 2011a), show in Figure 3. The bulk solid volume fraction can be expressed as a function of h_{exp} using:

$$\varepsilon_{s,b} = \frac{m_{bed}}{\rho_p V_{exp}} \quad (3.3.1)$$

where V_{exp} is the expanded volume and m_{bed} is the mass of the bed. This correlation was used for internal spouting and jet fluidized bed dynamics. The bulk solid fraction from the expanded bed height cannot be properly represented at 5% of the maximum bed height intensity in a jet spouting regime due to the height of the spouting fountain. Instead a correlation between $\varepsilon_{s,b}$ and I_{cor} from the jet fluidized regimes are used to define the solid volume fractions for spouting regimes. This is further discussed in Section 4.3.

3.4 Solid Volume Fraction

Each intensity matrix consists of front particles (highest intensity values), back particles (low intensity values), and the gas phase (lowest intensity values). In order to convert I_{cor} into the solid volume fraction, ε_s , a correlation function is needed. The notation that particles area fractions could be defined from the intensity values was studied by Heffels et al. (1996) and Boerefijn and Ghadiri (1998). Later Link et al. (2005) further their studies to develop the porous cube model to correlate image intensity values with solid volume fraction using:

$$\varepsilon_s = (I_{cor})^{1.5} \quad (3.4.1)$$

Agarwal et al. (2011a) redefined this function to take into account the area fraction, A , along the front wall occupied by illuminated particles. This factor is necessary to justify the lower intensity values of the solid particles in the depth of the bed over the particles located at the front wall containing higher intensity values. The area fraction is then converted into the solid volume fraction through parameter B .

$$\varepsilon_s = (A \cdot I_{cor})^B \quad (3.4.2)$$

Link et al. (2005) used a similar approach by rising I_{cor} by a power of 1.5 to obtain a ε_s correlation when using a bed depth of $6D_p$. The parameters A and B in this study were empirically determining through calculating the least square fitting power law between the bulk solid fractions and the mean I_{cor} values. A threshold value was set to condition ε_s to the maximum particle packing fraction, ε_s^{max} . This value was determined by the maximum particle bulk solid fraction found from the stagnant fixed bed, given in Table 1.

3.5 Pressure Drop Spectral Analysis

The combination of PIV and DIA are effective non-intrusive measurement techniques when visual observation is available. However, the convenience of having full field observation is not typically viable in larger scaled-up beds. To address this issue there has been substantial research using non-invasive pressure analysis to classify the state of both fluidized (Croxford and Gilbertson, 2011; Zhang et al., 2010) and spouting (Leu and Lo, 2005) beds. The advantage of this study is both PIV and DIA can be used over the full field of the bed to validate pressure analysis.

There are three common types of pressure analysis established in literature which is the time domain, frequency domain, and chaos analysis. This study utilizes the non-intrusive pressure drop spectral analysis to classify the hydrodynamics into various flow regimes. The analysis allows for the time series signal to be converted into the frequency domain.

First, the low pass filtered time domain signal was processed through the Fast Fourier Transform (FFT) algorithm. The Fourier transformation allows for the identification of the amplitudes and the frequency phases within the pressure signal. The forward Fourier transform can be defined as:

$$p(u) = \int_{-\infty}^{\infty} p(t) \cdot e^{-2\pi i u t} dt \quad (3.5.1)$$

where $p(u)$ is the complex Fourier transform of a continuous function $p(t)$, u is the frequency, t is the time and i is the basis for complex numbers. Euler's Identity

$$e^{i\theta} = \cos \theta + i \sin \theta \quad (3.5.2)$$

can be used with Equation 3.5.1 to convert it into its sinusoidal form:

$$p(u) = \int_{-\infty}^{\infty} p(t)(\cos(2\pi u t) - i \sin(2\pi u t)) dt \quad (3.5.3)$$

Since the pressure signal $p(t)$ is not a continuous function but rather a sequence of N discrete data points, j , the finite domain discrete time signals are analyzed through the Discrete Fourier Transform (DFT):

$$\hat{p}(k) = \sum_{j=1}^N p(j) e^{(-2\pi i/N)(j-1)(k-1)} \quad (3.5.4)$$

where k is the frequency index. The k^{th} output corresponds to the k^{th}/N frequency, meaning the second half of $\hat{p}(k)$ is the same as the first half and was therefore discarded (Figliola and Beasley, 2006). Likewise no periodicity of the signal is given when k is equal to one as it represents the sum of all the inputs and was consequently thrown out. The resulting transformation was then rendered into the frequency power spectrum by multiplying $\hat{p}(k)$ by its own conjugate $\hat{p}^*(k)$:

$$P(K) = \hat{p}\hat{p}^* \quad (3.5.5)$$

The peak frequency, also known as the dominant frequency, found in the power spectrum was used with visual observation to classify the state of the bed into three main flow regimes: Fixed Bed and Internal Spout (Case I), Jet Fluidized (Case II), and Jet Spouting (Case III). However, the pressure signal is a complex function of the particle properties (Fan et al., 1981), probe position (Hong et al., 1990; Wilkinson, 1995), bed height (Bi and Grace, 1996), geometry (Wormsbecker et al., 2009), and materials (Fan et al., 2008). Therefore, the pressure analysis in this study is not exclusively a function of the flow regime state.

4. Results and Discussion

The 2-D hydrodynamic characteristics were investigated through varying the number of slit jets, gas velocities, and particle diameters. This section discusses the mapped flow regimes, minimum fluidization, jet system behaviors, local void fraction profiles, and the solid particulate circulation rates.

4.1 Flow Regimes and Minimum Fluidization

Four main operating flow regimes resulted from the combination of the one, two, and three jet experimental tests. Using visual observation accompanied with spectral analysis the dynamic behavior was distinguished into:

- Fixed Bed: Figure 4.a
The particles are un-fluidized and remain stationary forming a fixed bed.
- Internal Spouting: Figure 4.b
The jet(s) penetrates into part of the bed forming an internal cavity while the surrounding particles remain un-fluidized. Individual jets remain isolated and do not mix with each other.

- Jet Fluidized: Figure 4.c
Bubbles detach from the internal cavity. The particles surrounding the jet(s) are fluidized, while the jet(s) profiles remain below spouting conditions.
- Jet Spouting: Figure 4.d
The internal cavity reaches the top of the bed causing the jet(s) to produce a spout channel.

Similar categories of jet systems have been characterized for fluidized (Link et al., 2005) and spouting (Freitas et al., 2004a; Sutanto et al., 1985) beds. Mean Prewitt high pass filtered image are shown in Figure 4 to illustrate each of the various flow regimes.

The point of minimum fluidization was found when the magnitude of the pressure drop offsets the weight of the particles and the frictional forces within the bed. Figures 5 and 6 shows the pressure drop for two different size glass particles using one, two, and three jet distributor plate systems. In the region of A-B, the pressure drop increases almost linearly for increasing gas flowrate. This region marks the points of fixed beds and internal spouting regimes. At point B, u_{mf} is reached when the bubbles from the internal spout begin to reach the surface of the bed causing the pressure drop to decrease. Just beyond this point marks the onset of fluidization, turbulent fluidization, and spouting.

For single jet experiments, the pressure drop decreases from B-C when the spout broke through the bed. Then from C-D the pressure continued to drop until reaching a stable operating range. This sequence of progressive pressure drop for a single jet spouting bed has been previously been reported by Kunii and Levenspiel (1991) and Markowski and Kaminski (1983). The characteristic differences in B-C from Figures 5 and 6 may show the dependence on the pressure probe position relative to the bed height. These differences were examined by Wang et al. (2000) in a spouted bed.

For two and three jet configurations the pressure drop remained nearly constant in B-D. This region exhibits a mix of both spouting and turbulent fluidized bed characteristics. This is attributed to the sequence of particle buildup blocking the spout, followed by the particles being propelled into the freeboard. The pressure drop remains stable as the overall bed dynamics acts in a turbulent fluidized regime.

As this experimental study was design for CFD validation, the particle-wall effects on u_{mf} must be noted. Typical minimum fluidization velocities found in literature for similar sized glass Geldart B and D classified particles are given in Table 2 along with those measured from this study. All minimum fluidization velocities compared in this table are from either 2-D or 3-D bed configurations with larger cross-sectional areas, A_t , than examined in this study. The pronounced particle-wall effects between a 2-D and 3-D bed has been noted in an experimental study by van Buijtenen et al. (2011b). Another recent study by Grace and Li (2010) emphasizes the importance of CFD boundary conditions, ie. no-slip, partial slip, or full slip, when modeling 2-D bed hydrodynamics.

The maximum pressure drop across the bed can be simply defined by $m_{bed}gA_t^{-1}$ when no wall or particle friction effects exist. Alternatively the magnitude of the pressure drop across a column of packed solids is commonly evaluated through the empirical equation of Ergun and Orning (1949) with sole respect to the void fraction and fluid flux:

$$\frac{\Delta P_{Ergun}}{h_{exp}} = au + bu^2 \quad (4.1.1)$$

where a is defined as the viscous coefficient,

$$a = \frac{150\mu_g(1 - \varepsilon_f)^2}{\varepsilon_f^3(\phi_s D_p)^2} \quad (4.1.2)$$

μ_g is the viscosity of the inlet gas, ϕ_s is the particle sphericity, and b represents the inertial coefficient:

$$b = \frac{1.75\rho_g(1 - \varepsilon_f)}{\varepsilon_f^3\phi_s D_p} \quad (4.1.3)$$

However, this does not account for wall friction effects and makes the implicit assumption of a homogenous void fraction and gas velocity distribution. To account for the wall effects, Liu et al. (2008b) defined a new parameter to Equation 4.1.1. The maximum extra pressure drop, ΔP_{max} , was estimated from

$$\frac{\Delta P_{max}}{V_{bed}} = \frac{(\Delta P/h_{exp} - \Delta P_{Ergun}/h_{exp})_{u=u_c}}{A_t} \quad (4.1.4)$$

when the superficial gas velocity reaches the critical, u_c , velocity. The resulting average maximum extra pressure drop, $\Delta P_{max,avg}$, per a particulate type equated in this study is given in Table 1 to represent the added particle-wall and frictional effects.

4.2 Pressure Drop Spectral Analysis

The frequencies in the time domain of the differential pressure signal were analyzed through the power spectrum. The resulting dominant frequencies were used to define each of the four flow regimes. The power spectral densities for a single jet are shown in Figure 7. Fixed bed and internal spouts, given in Figure 7.a, show significant peaks in the power spectrum only at low frequencies $\ll 1$ Hz. There was a minimal increase in the dominant frequency with increasing gas velocity in the two regimes. The slight power at these low frequencies could possibly be due to external disturbances or turbulence generated by the gas flowing through the packed bed. Without visual observation, it would be hard to distinguish between the two cases. Due to their close similarities the two cases are combined and defined as Case I.

As the gas velocity surpassed u_{mf} the dynamics of the bed transitioned into jet fluidization. Two dominant frequencies are seen in the power spectrum in Figure 7.b. The higher frequency is in the range of 4 - 5 Hz while the lower frequency remains close to that of an internal spout. This suggests the flow regime is showing both characteristics of an internal spout and jet fluidization.

Further increase of the superficial gas velocity leads to jet fluidization (Case II). Figure 7.c shows only one dominant frequency ranging from 4 - 5 Hz. However, the wider range of frequencies displaced can be attributed to the passing of bubbles in the fluidized bed. This characteristic has been substantially studied (Bi, 2007; van Ommen et al., 2011) due to the complexity of the pressure signal.

A transitional period between the fluidized and spouting dynamics can also be captured with spectral analysis. Two frequencies, which appear to be near harmonics, are shown in Figure 7.d. Here the internal spouting cavity has reached the top of the bed. The larger frequency defines the onset of spouting while the lower frequency shows the progressive bubble formation and sudden eruptions.

Once the spout channel has been well defined only one dominant frequency remained. This frequency ranged from 8 - 10 Hz for the single jet, shown in Figure 7.e. As the inlet gas velocity increased so did the frequency of the pressure signal. This would suggest the transition

to the spouting regime is not sudden, but rather a continuous process. Figure 8 contains a plot of the dominant frequency levels at all tested G550 velocities.

As seen in Figure 8, the same spectral density analysis was applied to two and three jet distributor plates. Similarly, frequencies well below 1 Hz were seen for the fixed and internal spouts (Case I). However, both fluidized beds and the transitional period also, resulted in lower dominant frequencies from 1 - 4 Hz. This use of multiple jets promoted jet interactions and decreased dead zones creating a wider range of frequencies in the power spectrum.

Two and three jet systems reached the spouting regime at a slightly higher flowrate than the single jet. The use of more than one jet created a dynamic sequence between spouting, particulate build-ups, and the eruption of the solid particle clusters. This formed a mixture between spouting and a turbulent fluidized bed regime. The resulting dominant frequencies remained below the single jet spouting frequencies, ranging from 4 - 7 Hz.

4.3 Void Fraction Correlation

The glass 550 μm particle expanded bed heights and bulk solid fractions classified by Case I and II are shown in Figure 9. The onset of the minimum fluidization velocity can be observed when h_{exp} exceeds the initial bed height. Likewise, the decline in $\varepsilon_{s,b}$ can also be used to define u_{mf} .

Figure 9.a shows a sharp drop in the overall bed bulk solid fraction at the onset of fluidization. This is due to the higher jet penetration depth of a single jet. The rate of expansion in h_{exp} was found to decline when multiple jets were used. At gas velocities near u_{mf} the two jet system remained isolated with only bubbles merging near the surface of the bed. Implementing a third jet prompted jet interactions. The three jets merged into a single jet producing lower $\varepsilon_{s,b}$ values than the two jet system, as seen in Figure 9.b and 9.c

It could appear in Figure 9 that a significantly lower u_{mf} value exists for the one jet system over the multiple jet studied. However, a higher frequency of bubbles was produced through the surface of the bed during the PIV sampling time which resulted in higher intensity values in the mean I_{cor} matrices at the surface level of the bed. This produced slightly higher bed heights shown in Figure 9.a. Due to this observation the commonly used pressure drop analysis, discussed in Figures 5 and 6, was consequently chosen to determine the onset of fluidization.

The mean intensity and bulk solid fraction values are plotted in Figure 10 for all particles in the fluidized bed regime (Case II). The data was fitted with Equation 3.4.2 by applying a least square fit power law. Parameters A and B were found near to Link et al. (2004) and Agarwal et al. (2011a) with B equal to 1.66 and A equal to 0.98 and 1.16 for the 550 μm and 750 μm particles respectfully.

Factor A represents the spectral parameter of the particles while parameter B accounts for the mean solid volume fraction across the depth of the bed (Agarwal et al., 2011a). Parameter B was found equal to 1.5 by Link et al. (2004) for a single slot jet distributor plate with a depth of $6D_p$. This same parameter was found to be slightly higher in this study for a bed depth of 6 to $9D_p$. This suggests that thicker beds tend to have a higher B value, while thinner beds would have a B value closer to one, as observed in the results of Boerefijn and Ghadiri (1998).

The bulk solid fractions of the spouting beds could not be properly defined from the maximum expanded bed heights from Equation 3.3.1, due to the development of spout fountains. To overcome this issue it was assumed that the identical G550 and G750 particles of Case III followed the same particle intensity correlations as in Case II. The resulting solid volume fraction correlation from Equation 3.4.2 was then applied to the spouting regimes.

The bulk solid volume fractions were then used to compute the localized gas void fractions ($\varepsilon_f = 1 - \varepsilon_s$). Full field view maps under both fluidized (Case II) and spouting (Case III) regimes are given in Figures 11 and 12 respectfully.

4.4 Fluidized Bed Void Fraction

The fluidized bed regime (Case II) showed characteristics of internal jets with bubble formations for all size glass particles. The jets diameters expanded from the inlets until reaching a maximum width. Here the diameter of the jet remained constant until bubbles were formed. Figure 11 shows the full field void fraction comparison between the two sized particles for one, two, and three jet systems at $1.6 u_{mf}$.

Jet penetration heights were found to be higher at larger superficial gas velocities. The smaller glass particles also produced larger jet penetration heights over the 750 μm particles in all three jetting systems. This fluidized bed characteristic is in agreement with the experimental single jet findings of Ruoyo et al. (1996). Figure 11 also shows smaller dead zones sizes for the

larger diameter solid particles. This is due to the increased internal spouting diameters of the 750 μm particulates.

Double jet systems did not always show signs of interacting at low gas velocities. Instead there was a transitional period prior to the production of a jet interacting system. At lower fluidization velocities the shape of the bubbles produced by each jet was influence by the other. A further increased velocity caused the bubbles to merge into a larger bubble at middle of the bed. This bubble would continue to rise through the particles before causing the surface of the bed to collapse while new bubbles were being formed. Implementing a third jet into the double jet system created jet interactions for all gas velocities surpassing u_{mf} .

Shorter distances between the slit jets were achieved with the triple jet system. This caused the jets to merge close to the distributor plate as the inlet gas velocity increased. For Case II, dead zones always remained between the jets. It was not until the spouting regime (Case III) did the dead zones between the three jets begin to completely disappear due to the jets merging near the distributor plate.

4.5 Spouting Bed Void Fraction

Increasing the inlet gas velocities from Case II caused the dynamics of the bed to transition into the spouting regime. The spouting bed provided higher particle mobility with a smaller pressure drop across the bed. Case III can be characterized through investigating three zones: the spout, fountain, and annulus. Figure 13 gives an image of an instantaneous I_{cor} matrix defining the location of the various zones. Mean void profiles for Case III are given for all jet systems in Figure 12 at 3 u_{mf} .

4.5.1 Spout Zone

The transitional region into Case III showed unstable spouting channels for the single jet studies. This affect is attributed to the lack of in-bed stabilizers commonly used in spouting beds (He et al., 1994a) to prevent the spout from deviating from the vertical axis of the bed. As the spouting velocity was further increased, stable jet formations were produced for the single jet studies. The effect of a swaying spout can be seen in the decrease of ε_f in the fountain of the 1G550 system in comparison to the 1G750 test in Figure 12.a and 12.d. A stable spout showed a narrower void fraction profile between the upper surface of the bed and the base of the fountain. Additionally, higher particle concentrations were observed through the mean PIV images in the fountain region when swaying was not exhibited.

The voidage in the spout zone increased with increasing gas flowrate. Similar to Case II, the width of the inlet jet also increased almost linearly through the use of larger diameter particles and along the vertical axis of the spout. However, the width of the spout then decreased towards the top of the annulus. This denser ε_s zone is associated with the solid entrainment of annulus. This finding has also been noted in a flat based cylindrical half column (Day et al., 1987) and a conical spouted configuration (Olazar et al., 2001).

The radial voidage within the spouting zone increased with increasing gas velocity. The axial voidage distribution for a spouting bed at $2 u_{mf}$ is shown in Figure 14 at a height of 19.2 mm above the distributor. The shape of a single jet spouting regions has been described as elliptical by Guo et al. (1996). This shape is displayed in Figure 14 with the highest void fraction nearest to the centerline of the jet with decreasing values along the boundaries of the spout. A similar trend can be seen in the void profiles along the edges of spout in the two and three jet systems.

The dead zone between the jets in a double jet system can be clearly identified at the peak in ε_s at the centerline of the bed. At a further radial distance from this peak two elliptical ε_f curves detect the location of each spouting zones. The three jet system shows only one enlarge spouting zone in Figure 14. The reason for this is credited to jet merging. At a height of 19.2 mm the three jets have combined to form an enlarged single spout zone.

4.5.2 Annulus Region

The area of downward particle entrainment surrounding the spout zone is known as the annulus. Smith (1975) described this region for a single jet as the downward parabolic trajectory of particle movements towards the spout. The dynamics of the annulus have also been characterized as being nearly symmetric (Krzywanski et al., 1992) through a multi-dimensional model. Near local void fraction symmetry can also be observed in Figure 14 in the moving zones for all jet systems.

The void fraction in the annulus has frequently been defined as being equal to a loosely packed bed, around 0.4, and constant throughout the region (Mathur and Gishler, 1955; Smith, 1975). However contradicting results can be found throughout literature that dispute these findings. Thorley et al. (1959) and Grbavcic et al. (1976) concluded the void fraction varies in different parts of the annulus. Lim and Mathur (1974) determined the amount of gas in the annulus to decrease as the spouting velocity increased. Similar finding were found by Day et al.

(1987) and Epstein (1978) which also defined the void fraction of the annulus to be equivalent to a loosely packed bed.

Conflicting results were again found by Van Velzen et al. (1974) and Roy et al. (1994) for a conical based bed. These studies examined the annulus velocity and found the velocity to decrease in the lower sections of the annulus region. This led to the conclusion that a decrease in the velocity may lead to an increase in ε_f with respect to height in the annular zone. More recent studies by He et al. (1994a) examined a cylindrical column and half column bed voidage with a fibre optic probe. These experimental tests results were found conflicting to the finding of Lim and Mathur (1974). He et al. (2000) performed additional tests in an axisymmetric column to confirm the void fraction in the annulus increased with increasing gas velocity. It was concluded that the ε_f in the annulus increased from 2.5% to 11.6% of a loosely packed bed depending on the inlet gas velocity and bed geometry. This brings into question two common assumptions that the voidage in the annulus is constant and equal to a loose-packed bed.

The single jet findings in this study show the void fraction in the annulus to be slightly higher than a loosely packed bed as show in Figure 14. A recent study by van Buijtenen et al. (2011a) also examined a pseudo 2-D single jet spouting bed with PIV and DIA. However, a different correlation between the pixel intensity values and the solid fraction was derived. It was concluded from their study that any small difference in the void fraction of the annulus would be difficult to observe due to the uncertainty in their ε_f calibration curve.

Contrarily, the settings of the CCD used in the PIV analysis of this study were better set to capture particle motion in the annulus. As a result, higher gas fractions were observed than a loosely packed bed due to the high downward entrainment of particulates. This suggests the spout channel is not the only main factor in the vigorous gas-solid mixing, but that the annulus is also a large contributor in the multiphase mixing. In addition to the voidage effects caused from downward entrainment, the gas was also observed to flare outward from the spout channel into the annulus. This was often a contributing factor in the observed unstable spout swaying.

The downward moving zones in double and triple jet systems showed different hydrodynamics than that of the single jet case. This was caused by the higher order of particle entrainment which reduces the size of the dead zones separating the jets. With fewer particles between the jet systems, a combined single jet was formed which merged closer to the distributor plate at larger gas velocities. Unlike the single jet case which exhibits stable spouting due to a

well-defined annulus (Krzywanski et al., 1992) , the multiple jet systems remained highly unstable at all spouting velocities resulting in unstable moving zones. A subsequent sequence of particle accumulations and eruption of the particles toward the wall and freeboard was formed. This also produced higher void fraction than a loosely packed bed in the moving zones similar to the single jet case.

The axial ε_f distributions can be categorized into three main sections: i.e. the spout, annulus, and dead zones. The elliptical peaks in ε_f define the spouts in Figure 14. At further radial distances from the center axis of the bed, an increase in ε_s depicts the moving zones. This trend suggests that there are higher particle concentrations closer to the spout and a higher gas voidage close to the walls of the bed. A second elliptic peak is seen in the single jet case near the wall when dead-zones are not present. This was followed by a decline in gas void fraction defining the dead zones.

4.5.3 Fountain Region

A fountain region was produced from the deceleration of solid particles above the single jet spouting zone. This region takes the form of a parabolic shape (Grace and Mathur, 1978) which can be further divided into two main sections. The first being the core which consists of the solid up-flow and the second region is defined as the periphery which entails of the regions of solid particle down-flow returning to the annulus. In a small scale laboratory bed it is important consider these regions as they can contain a significant fraction of the total solid particles.

The highest particle concentrations in the fountain were found along the central axis of the fountain core and gradually decreased radially toward the periphery, shown in Figure 15. This is contrary to the notion of Hook et al. (1992) who predicted the fountain core to spread radially outward along the entire height of the fountain. The effects of increasing spout velocity are shown in Figure 16 by taking the cross sectional average gas void fraction along the height of the fountain. It was found that increasing spout velocities produced higher solid concentration in the core and a growth in the radial ε_s profile. This is contrary to the findings of He et al. (1994a) who concluded that particle solid fraction in the core decreases with increasing gas velocity. The reasoning for this was attributed to the increased radial spreading of particles. However, it must be noted that different bed geometries and physical particle properties were examined between their study and the experiments used in this investigation.

Solid concentrations were found to increase from the base to the core of the fountain and are consistent with the theoretical model produced by Grace and Mathur (1978). In their model, ε_f in the core was equivalent to a loosely packed bed. At over $3 u_{mf}$, Figure 15 shows the lowest void fraction as 0.54. This value is not consistent to a loosely packed bed but is in closer agreement with the value of 0.57 found by He et al. (1994a). The particle concentrations then decreased from the core to the top of the spout. Again this contradicts the model of Grace and Mathur (1978), who assumed a loosely packed voidage at the top of the fountain. Instead this trend was found to be in general agreement with Waldie et al. (1986).

4.6 Dead Zones

The regions of stagnant particles between the jet inlets and near the wall close to the distributor plate are categorized as the dead zones. It is important to analyze the size of these unfluidized sections as dead zones can lead to serious problems if exothermic reactions are to occur (Muller et al., 2010). The height and angle of the jets along the dead zones have been previously characterized with correlations for fluidized beds (Agarwal et al., 2011b; Rees et al., 2006; Thorpe et al., 2002). The aim of this study is to examine the influence of a multiple jet system. Therefore, bed dead zone mass fractions are computed from the volume, V_{dz} , and the average void fraction, $\varepsilon_{f,dz}$, of the dead zones as:

$$\eta_{dz} = \frac{(1 - \varepsilon_{f,dz})V_{dz}\rho_p}{m_{bed}} \quad (4.6.1)$$

The dead zone areas were defined as near zero velocity regions as indicated on the overlaid PIV vectors and mean Prewitt high passed filtered image illustrated in Figure 17. A reduction in the total dead zone fraction was found as the gas velocity increased for all jet combinations. Similar findings have been made for a single jet flat bottom spout bed (San José et al., 1996).

Figure 18 shows lower dead zone fractions for larger particle diameters. This was due to the effect that larger particles created an increased spouting zone. The total dead zones decreased as additional jets were implemented into the system. However, the use of two jets initially displayed lower dead zones over the triple jet system for the 550 μm glass particles. This was accredited to the jets merging towards the center of the bed for the three jet case. Differently the two jet test exhibited isolated jets which promoted dead zones reductions near the walls. This shows the importance of jet pitch in overall dead zone reduction.

4.7 Solid Circulation Rates

Calculations of solid entrainment require either knowledge of the particle and gas flow rates, or the rate of jet expansion angles (Stein et al., 1998). Therefore, the PIV particle velocity vectors, \vec{v}_x and \vec{v}_y , were coupled with their corresponding void fractions in each interrogation area to compute the local particle mass flux:

$$\dot{m}'' = \rho_p(1 - \varepsilon_f)\|\vec{v}\| \quad (4.7.1)$$

Based on the conservation of mass, the total solid up-flow must equal the total solid down-flow at any level within the bed. Since the annulus consists of the downward granular flow and the spout contains the upward gas-solid mixture, the solid mass flow should be comparable between the two regions. This concept has been previously investigated by He et al. (1994a) in a cylindrical spout bed and resulted in maximum deviation of 19% in the conical base region. Similar studies in a conical bed have also concluded the solid descending flow in the annular region to be nearly equivalent to the solid ascending flow in the spout region (San José et al., 1998; San José et al., 2006). The minor error found between the two solid rates has been attributed to the higher order of turbulent solid movement and flow fluctuation through the annular region found in a cylindrical column (Uemaki and Tsuji, 1992). To address this issue in this study, the rate of solid circulation was computed along the border of the spout, where San José et al. (2006) computed the maximum horizontal particle velocity from a mass balance equation. First, the horizontal component of each velocity vector was processed through Equation 4.7.1 to compute local horizontal particle mass fluxes, $\dot{m}_{x,n}''$. The fluxes were then multiplied by the cross-sectional area of an IA, $A_{IA,t}$. The resulting particle entrainment rates were summed along the spout border to compute the total solid circulation rate,

$$\dot{m}_{x,tot} = \sum_{n=1}^{N_{tot}} \dot{m}_{x,n}'' A_{IA,t} \quad (4.7.2)$$

The solid circulation rates can also be represented by a volumetric circulation flowrate ($\dot{V}_{x,tot} = \dot{m}_{x,tot}/\rho_p$), shown in Figure 19. The rate of particle entrainment was found to increase linearly with increasing gas velocity. This was also observed in cylindrical (Uemaki and Tsuji, 1992), semi-circular (Kececioglu and Keairns, 1989; Yang and Keairns, 1982), and rectangular (Agarwal et al., 2011a) columns. Due to the highly turbulent nature of the multiple jet systems in the spouting regimes, a stable and well-defined spout-annulus border was not exhibited. Therefore, the solid circulation analysis was only applied to the single jet studies.

However a recent multiple jet study, in a purely fluidized regime, was found to produce a decrease in the linearly increasing solid rate at the onset of jet interactions (Agarwal et al., 2011a).

Higher circulation rates were observed for the larger diameter particles. This can be attributed to the increased spouting diameter, decreased dead zones, increased particle velocity along the jet border, and a higher stagnant bed height. A larger bed height allowed for an increased spout surface area resulting in a higher solid cross-flowrate. This finding can be further attributed to the higher particle velocities found along the vertical spout axis for the 750 μm particles. This finding is in good agreement with Olazar et al. (1998) and Filla et al. (1983) who also found the rate of momentum exchange between the gas and solid particles to increase with particle size.

The accuracy of Equation 4.7.2 was assessed by comparing it with the counter current two-phase flow model of van Deemter (1967) for a fluidized bed. The basis of this model is to relate the total solid circulation rate to the total downward mass flowrate of the bed. This model takes the average vertical downward velocity, $\vec{v}_{y, neg}$, over the entire bed with respect to the total cross-sectional area of the distributor plate:

$$\dot{m}_{x, tot} = \rho_p A_t f r_{neg} (1 - \varepsilon_f) |\vec{v}_{y, neg}| \quad (4.7.3)$$

A factor, $f r_{neg}$, is implemented into the solid circulation calculation to account for the volume fraction of downward moving particles and gases. The volume fraction of downward gases is significantly smaller than the fraction of downward particles due to the density differences and the dynamics of the spouting regime over that of a bubbling fluidized bed. The gas fraction in $f r_{neg}$ was neglected due to this reason and that it was not possible to account for the downward gases through the experimental procedures of this study.

A comparison between the two analyses is plotted in Figure 19. An average deviation below 10% was found between the two models for both the 550 μm and 750 μm particles. Both trends show a linear increase in the volumetric circulation rate with respect to increased inlet jet velocity.

The circulation rate can be further investigated through computing the frequency residence time of the particulates through the bed. This was calculated through measuring the average cycle time by:

$$\bar{t} = \frac{m_{bed}}{\dot{m}_{x,tot}} \quad (4.7.4)$$

This type of analysis has been previously applied to conical (San José et al., 1996) and cylindrical (Roy et al., 1994; Thorley et al., 1959) spouted beds. It must be pointed out that these beds are designed with angled contactor bases to reduce the effects of static dead zones. Figure 18 shows the dead zone fraction in the single jet cases to range from 7 to 36% of the total bed mass for the given gas flow rates. To account for the stationary particulates, Equation 4.7.4 was redefined as:

$$\bar{t} = \frac{m_{bed}(1 - \eta_{dz})}{\dot{m}_{x,tot}} \quad (4.7.5)$$

to take into consideration the dead zones. The resulting average cycle times between Equation 4.7.4 and 4.7.5 are shown in Figure 20. The average error found from neglecting the dead zones was 13% and 36% for the 750 μm and 550 μm particles respectfully. As expected both particles showed a nearly linear decrease in cycle time with increasing gas velocity. The average cycle time was also found to decrease with increased particle size, due to enlarged solid circulations rates. This trend is comparable with Filla et al. (1983) who concluded that there is a large resistance in the particulate phase to the transverse flow towards the dilute jet region for smaller particles.

4.8 Fountain Heights

In order to further understand the effects increasing gas velocity on the spout geometry, the height of the fountain, H_f , was calculated from the top of the surface of the bed to the top of the fountain. To account for the initial bed height differences from the total number of particles used between the 550 μm and 750 μm cases, the fountain heights are represented as bed height fractions:

$$\eta_{H_f} = \frac{H_f}{H} \quad (4.8.1)$$

for the single jet studies in Figure 21. The fountain height expansion ratios increased with spouting velocity and were found to be higher for the larger glass particles. To compare these results with the correlations found in literature, the particle velocity in the spout at the surface level, $\vec{v}_s(h_0)$, of the bed is needed. Since the CCD camera in the PIV analysis was adjusted for better signal noise ratios, the velocity vectors in the spout were masked. Therefore, a correlation between the spout velocity and solid circulation rate was derived.

An explicit model, similar to Equation 4.7.1, was developed by Day et al. (1987) to compute the total solid mass flux of a bed from the area, $A_s(h_0)$, void fraction, $\varepsilon_{f,s}(h_0)$, and velocity of the spout at the surface level of the bed.

$$\dot{m}_{tot} = \rho_p A_s(h_0) \bar{v}_s(h_0) [1 - \varepsilon_{f,s}(h_0)] \quad (4.8.2)$$

The velocity in this study was computed from combining the cross-sectional area of the spout and the void fraction at the surface level with the total solid circulation rates. A similar approach by Uemaki and Tsuji (1992) used this correlation to compute the void fraction in the spout from the solid circulation rate and velocity. The importance for detailed void fractions and spouting diameters needed in this type computation has been noted (Kim and Cho, 1991). The use of PIV with DIA provided both detailed and localized void fractions along the structure of the spout.

A semi-theoretical spouting model was derived by Grace and Mathur (1978) from a force balance analysis. This was based on equations of motion with dependence on the spout voidage and particle velocity along the spout axis at the bed surface. Their findings produced an average deviation of 16.2% between their model and data. A best fit coefficient of 1.46 was applied to $\varepsilon_{f,s}(h_0)$:

$$H_f = \varepsilon_{f,s}(h_0)^{1.46} \frac{\bar{v}^2(h_0)}{2g} \frac{\rho_p}{\rho_p - \rho_g} \quad (4.8.3)$$

and resulted in a reduction in the average standard deviation to 15.4%. It is important to note from Figure 13 that the small scale bed in this study produced higher annular zones along the radial walls of the bed in comparison to the axial center of the spout. This effect has not been previously reported as the width of most laboratory scale beds found in literature are of a larger magnitude. Therefore, the fountain height has been defined from both the highest surface level of the bed along the annulus, $H_{f,A}$, and from the lowest part located at the top of the spout channel, $H_{f,S}$, when comparing to existing correlations. The difference between these two measurements is illustrated in Figure 13.

The model in Equation 4.8.3 under predicted to height of the fountain in all cases, shown in Figure 22. An average deviation of 57% and 68% was found from using $H_{f,A}$ and $H_{f,S}$ for the 550 μm particles respectfully. Closer agreement was found for the 750 μm particles with an average deviation of 21% for $H_{f,A}$ and 43% for $H_{f,S}$. This is different than the results of He et al.

(1994b) who found good agreement with this model for glass spheres in a cylindrical column. However the under prediction of fountain heights was also found by Olazar et al. (2004) with a relative error ranging from 50 to 60%. In addition Liu and Litster (1991) has also pointed out that this model needs to account for particle sphericity.

Other fountain height correlations have also been proposed (Chatterjee, 1970; Day, 1990; Hook et al., 1992; Morgan et al., 1985) and were compared with further experimental data by Day (1990) and Olazar et al. (2004). A regression analysis with a searching techniques was applied by Day (1990) to the data of Grace and Mathur (1978) to produce an empirical fountain height correlation. The derived equation had no dependency on void fractions or particle velocities. However, a higher average deviation between the resulting correlation and Equation 4.8.3 was found from the data of Grace and Mathur (1978).

Various combinations of correlation coefficients have also been fitted to Equation 4.8.3 by Olazar et al. (2004). The optimization in their study resulted in using the suggested fountain height correlation derived by Thorley et al. (1959):

$$H_f = \frac{\bar{v}^2(h_0)}{2g} \frac{\rho_p}{\rho_p - \rho_g} \quad (4.8.4)$$

This analysis is based off the assumption that the drag forces are small in comparison to the gravity. A good fit of Equation 4.8.4 was found in the data of Olazar et al. (2004). However, it should be noted that the study only investigated velocities up to 1.3 times the minimum spouting velocity. Figure 22 shows good agreement between the correlation and the experimental data at low gas velocities. However, at higher gas velocities Equation 4.8.4 significantly over predicted the fountain heights. An overall average standard deviation of 31% and 73% was found for $H_{f,S}$ and $H_{f,A}$ respectfully for the 550 μm particles. All though significant error was found between the two previous correlations, they were successful in bounding the experimental results in this study.

Figures 21 and 22 show the fountain height to be directly proportional to the spouting velocity and is in agreement with Olazar et al. (2004) . Higher fountain heights were also seen for increased particle diameter. This contradicts Olazar et al. (2004) who found H_f to decrease by 33% as the particle diameters were increased from 3 to 5 mm. Two main reasons were noticeable in this study for explaining the differences. First, the larger particles produced an increased

spouting diameter, reduced dead zones, increased solid circulation, and a decreased average particulate cycle time as all were previously noted. Secondly, the particle drag force can decrease with increased particle diameter. This was mathematically represented through an equation of motion for a single solid sphere in a gas stream (Grace and Mathur, 1978; Kmiec, 1980; Thorley et al., 1959). Lastly it should be noted that the bed geometry of this study is different than the typical conical based and axisymmetric bed found from the prior compared studies. Therefore the data in this investigation should be applied with caution when comparing it with previous correlations.

5. Conclusion

The coupling of PIV and DIA were successfully used to analysis the two-phase dynamics of a flat bottom bed under fluidized and spouting conditions. Hydrodynamics of a multiple jet system was compared to that of a single jet for the validation of Discrete Particle Models. Time series pressure analysis for a single jet resulted in a lower pressure drop across the bed than that of multiple interacting jets. The rendering of the time series signal into the power spectrum made it possible to characterize the flow dynamics into three distinct regimes: Fixed Bed and Internal Spout (Case I), Jet Fluidized (Case II), and Jet Spouting (Case III).

A void fraction relationship was derived from the DIA and was found to be in close comparison with Link et al. (2004) and Agarwal et al. (2011a). The highest gas fractions were found in the spout and showed an elliptical profile. Applying radial void fraction analysis exposed jet interactions while also showing that multiple jets can act independently. The annulus and fountain regions both displayed higher void fractions than a loosely packed bed contradicting Smith (1975) and Grace and Mathur (1978). Additionally, particulate concentrations were found to radially decrease in the fountain from the core to the periphery.

An existing summary and comparison between various studies and correlations on solid circulation rates and fountain heights was given. The PIV adaptive correlation algorithm was employed to compute the solid circulation rate. A linearly increasing rate was found to be directly proportional to the gas velocity and increased particle diameter due to the enlarged momentum exchange. Good agreement was found between the methods of the solid circulation rate produced in this study with the counter current two-phase flow model of van Deemter (1967). Dead zone fraction analysis emphasized the importance of jet pitch as implementing

more jets did not always directly resulted in decreased total dead zones due to jet merging. This finding was carried over to define an enhanced method in computing average cycle times.

The expanded fountain heights for the rectangular flat bottom bed were compared with semi-theoretical models found in literature. At low spouting velocities the fountain heights were comparable to the neglected drag force model of Thorley et al. (1959). However, at higher flowrates the data was in closer agreement with the model produced by Grace and Mathur (1978) which added a correlation coefficient to compensate for the slight particulate drag effects. The overall fountain geometry was found near to the parabolic shape observed by Smith (1975). Higher fountain heights were computed at greater superficial spouting velocities and for larger particle diameters contrary to Olazar et al. (2004). The analysis found in this study was based on a rectangular multiple slit jet distributor and therefore should be applied with caution when comparing it to cylindrical and conical based beds.

Acknowledgements

The authors are grateful for the support from the Virginia Tech Institute for Critical Technology and Applied Science (ICTAS).

References

- Agarwal, G., Lattimer, B., Ekkad, S., Vandsburger, U., 2011a. Experimental study on solid circulation in a multiple jet fluidized bed. *AIChE Journal*, n/a-n/a.
- Agarwal, G., Lattimer, B., Ekkad, S., Vandsburger, U., 2011b. Influence of multiple gas inlet jets on fluidized bed hydrodynamics using Particle Image Velocimetry and Digital Image Analysis. *Powder Technol.* 214, 122-134.
- Bi, H.T., Grace, J.R., 1996. Modeling of solids global fluctuations in bubbling fluidized beds by standing surface waves - Comment. *Int. J. Multiph. Flow* 22, 203-205.
- Bi, H.T.T., 2007. A critical review of the complex pressure fluctuation phenomenon in gas-solids fluidized beds. *Chem Eng Sci* 62, 3473-3493.
- Bilbao, J., Olazar, M., Arandes, J.M., Romero, A., 1989. Optimization of the Operation in a Reactor with Continuous Catalyst Circulation in the Gaseous Benzyl Alcohol Polymerization. *Chemical engineering communications* 75, 121-134.
- Boerefijn, R., Ghadiri, M., 1998. High speed video image analysis of flow of fine particles in fluidized bed jets. *Adv. Powder Technol.* 9, 229-243.

- Bokkers, G.A., Annaland, M.V.S., Kuipers, J.A.M., 2004. Mixing and segregation in a bidisperse gas-solid fluidised bed: a numerical and experimental study. *Powder Technol.* 140, 176-186.
- Burgess, J.M., Calderbank, P.H., 1975. The measurement of bubble properties in two-phase dispersions—III. *Chem Eng Sci* 30, 1511-1518.
- Çeçen, A.e., 1994. The maximum spoutable bed heights of fine particles spouted with air. *The Canadian Journal of Chemical Engineering* 72, 792-797.
- Chatterjee, A., 1970. Spout-Fluid Bed Technique. *Industrial & Engineering Chemistry Process Design and Development* 9, 340-341.
- Croxford, A.J., Gilbertson, M.A., 2011. Pressure fluctuations in bubbling gas-fluidized beds. *Chem Eng Sci* 66, 3569-3578.
- Day, J.Y., 1990. The Fountain Height and Particle Circulation Rate in a Spouted Bed. *Chem Eng Sci* 45, 2987-2990.
- Day, J.Y., Morgan, M.H., Littman, H., 1987. Measurements of spout voidage distributions, particle velocities and particle circulation rates in spouted beds of coarse particles—II. Experimental verification. *Chem Eng Sci* 42, 1461-1470.
- Epstein, N., 1978. Non-Darcy Flow and Pressure Distribution in a Spouted Bed, pp. 98-103.
- Ergun, S., Orning, A.A., 1949. Fluid Flow through Randomly Packed Columns and Fluidized Beds. *Industrial & Engineering Chemistry* 41, 1179-1184.
- Fan, L.T., Ho, T.C., Hiraoka, S., Walawender, W.P., 1981. Pressure-Fluctuations in a Fluidized-Bed. *AIChE Journal* 27, 388-396.
- Fan, X.F., Parker, D.J., Yang, Z.F., Seville, J.P.K., Baeyens, J., 2008. The effect of bed materials on the solid/bubble motion in a fluidised bed. *Chem Eng Sci* 63, 943-950.
- Fayed, M.E., Otten, L., 1997. *Handbook of Powder Science and Technology* (2nd Edition). Springer - Verlag, pp. 532-567.
- Figliola, R.S., Beasley, D.E., 2006. *Theory and design for mechanical measurements*. John Wiley, Hoboken, N.J.
- Filla, M., Massimilla, L., Vaccaro, S., 1983. Gas Jets in Fluidized-Beds - the Influence of Particle-Size, Shape and Density on Gas and Solids Entrainment. *Int. J. Multiph. Flow* 9, 259-267.

- Franka, N.P., Heindel, T.J., Battaglia, F., 2007. Visualizing Cold-Flow Fluidized Beds With X-Rays. ASME Conference Proceedings 2007, 99-105.
- Freitas, L.A.P., Dogan, O.M., Lim, C.J., Grace, J.R., Bai, D.R., 2004a. Identification of flow regimes in slot-rectangular spouted beds using pressure fluctuations. *Can J Chem Eng* 82, 60-73.
- Freitas, L.A.P., Mitsutani, K., Lim, C.J., Grace, J.R., Wei, W.S., 2004b. Voidage profiles in a slot-rectangular spouted bed. *Can J Chem Eng* 82, 74-82.
- Goldschmidt, M.J.V., Link, J.M., Mellema, S., Kuipers, J.A.M., 2003. Digital image analysis measurements of bed expansion and segregation dynamics in dense gas-fluidised beds. *Powder Technol.* 138, 135-159.
- Grace, J.R., Li, T.W., 2010. Complementarity of CFD, experimentation and reactor models for solving challenging fluidization problems. *Particuology* 8, 498-500.
- Grace, J.R., Mathur, K.B., 1978. Height and structure of the fountain region above spouted beds. *The Canadian Journal of Chemical Engineering* 56, 533-537.
- Grbavcic, Z.B., Vukovic, D.V., Zdanski, F.K., Littman, H., 1976. Fluid-Flow Pattern, Minimum Spouting Velocity and Pressure-Drop in Spouted Beds. *Can J Chem Eng* 54, 33-42.
- Guo, Q., Zhang, J., Luo, G., 1996. Porosity Distribution in Two-dimensional Fluidized Bed with a Jet. *Chemical Industry and Engineering* 13, 14-19.
- He, Y.L., Lim, C.J., Grace, J.R., 2000. Pressure gradients, voidage and gas flow in the annulus of spouted beds. *Can J Chem Eng* 78, 161-167.
- He, Y.L., Lim, C.J., Grace, J.R., Zhu, J.X., Qin, S.Z., 1994a. Measurements of Voidage Profiles in Spouted Beds. *Can J Chem Eng* 72, 229-234.
- He, Y.L., Qin, S.Z., Lim, C.J., Grace, J.R., 1994b. Particle-Velocity Profiles and Solid Flow Patterns in Spouted Beds. *Can J Chem Eng* 72, 561-568.
- Heffels, C., Willemse, A., Scarlett, B., 1996. Possibilities of near backward light scattering for characterizing dense particle systems. *Powder Technol.* 86, 127-135.
- Hong, R., Li, H., Li, H., Wang, Y., 1997. Studies on the inclined jet penetration length in a gas—solid fluidized bed. *Powder Technol.* 92, 205-212.
- Hong, S.C., Jo, B.R., Doh, D.S., Choi, C.S., 1990. Determination of Minimum Fluidization Velocity by the Statistical-Analysis of Pressure-Fluctuations in a Gas Solid Fluidized-Bed. *Powder Technol.* 60, 215-221.

- Hook, B.D., Littman, H., Morgan, M.H., Arkun, Y., 1992. A-Priori Modeling of an Adiabatic Spouted Bed Catalytic Reactor. *Can J Chem Eng* 70, 966-982.
- Kececioglu, I., Keairns, D.L., 1989. Computation of Solid Circulation Rates in a Fluidized-Bed from Tracer Particle Concentration Distributions. *Can J Chem Eng* 67, 290-300.
- Kim, S.J., Cho, S.Y., 1991. Particle-Velocity and Circulation Rate in Liquid Spouted Beds. *Korean Journal of Chemical Engineering* 8, 131-136.
- Kmieć, A., 1980. Hydrodynamics of Flows and Heat Transfer in Spouted Beds. *The Chemical Engineering Journal* 19, 189-200.
- Krzywanski, R.S., Epstein, N., Bowen, B.D., 1992. Multi-dimensional model of a spouted bed. *The Canadian Journal of Chemical Engineering* 70, 858-872.
- Kunii, D., Levenspiel, O., 1991. *Fluidization engineering*. Butterworth-Heinemann, Boston.
- Laverman, J.A., Roghair, I., Annaland, M.V., Kuipers, H., 2008. Investigation into the hydrodynamics of gas-solid fluidized beds using particle image velocimetry coupled with digital image analysis. *Can J Chem Eng* 86, 523-535.
- Lefroy, B.E., 1969. The Mechanics of Spouted Beds. *Trans. Inst. Chem. Eng.* 17, 120.
- Leu, L.P., Lo, M.C., 2005. Pressure fluctuations in spouted beds. *Journal of the Chinese Institute of Chemical Engineers* 36, 391-398.
- Lim, C.J., Mathur, K.B., 1974. Residence time distribution of gas in spouted beds. *The Canadian Journal of Chemical Engineering* 52, 150-155.
- Lim, K.S., Agarwal, P.K., O'Neill, B.K., 1990. Measurement and modelling of bubble parameters in a two-dimensional gas-fluidized bed using image analysis. *Powder Technol.* 60, 159-171.
- Link, J., Zeilstra, C., Deen, N., Kuipers, H., 2004. Validation of a discrete particle model in a 2D spout-fluid bed using non-intrusive optical measuring techniques. *Can J Chem Eng* 82, 30-36.
- Link, J.M., Cuypers, L.A., Deen, N.G., Kuipers, J.A.M., 2005. Flow regimes in a spout-fluid bed: A combined experimental and simulation study. *Chem Eng Sci* 60, 3425-3442.
- Littman, H., Morgan, M.H., Narayanan, P.V., Kim, S.J., Day, J.Y., Lazarek, G.M., 1985. An Axisymmetric Model of Flow in the Annulus of a Spouted Bed of Coarse Particles - Model, Experimental-Verification and Residence Time Distribution. *Can J Chem Eng* 63, 188-194.
- Liu, G.Q., Li, S.Q., Zhao, X.L., Yao, Q., 2008a. Experimental studies of particle flow dynamics in a two-dimensional spouted bed. *Chem Eng Sci* 63, 1131-1141.

- Liu, L.X., Litster, J.D., 1991. The effect of particle shape on the spouting properties of non-spherical particles. *Powder Technol.* 66, 59-67.
- Liu, X.H., Xu, G.W., Gao, S.Q., 2008b. Micro fluidized beds: Wall effect and operability. *Chem. Eng. J.* 137, 302-307.
- Markowski, A., Kaminski, W., 1983. Hydrodynamic Characteristics of Jet-Spouted Beds. *Can J Chem Eng* 61, 377-381.
- Mathur, K.B., Gishler, P.E., 1955. A technique for contacting gases with coarse solid particles. *AIChE Journal* 1, 157-164.
- Morgan, M.H., Day, J.Y., Littman, H., 1985. Spout voidage distribution, stability and particle circulation rates in spouted beds of coarse particles—I. Theory. *Chem Eng Sci* 40, 1367-1377.
- Morooka, S., Kawazuishi, K., Kato, Y., 1980. Holdup and flow pattern of solid particles in freeboard of gas—solid fluidized bed with fine particles. *Powder Technol.* 26, 75-82.
- Muller, C.R., Holland, D.J., Sederman, A.J., Dennis, J.S., Gladden, L.F., 2010. Magnetic resonance measurements of high-velocity particle motion in a three-dimensional gas-solid spouted bed. *Physical review. E, Statistical, nonlinear, and soft matter physics* 82, 050302.
- Olazar, M., San Jose, M.J., Alvarez, S., Morales, A., Bilbao, J., 1998. Measurement of particle velocities in conical spouted beds using an optical fiber probe. *Industrial & Engineering Chemistry Research* 37, 4520-4527.
- Olazar, M., San Jose, M.J., Izquierdo, M.A., Alvarez, S., Bilbao, J., 2004. Fountain geometry in shallow spouted beds. *Industrial & Engineering Chemistry Research* 43, 1163-1168.
- Olazar, M., San José, M.J., Izquierdo, M.A., Alvarez, S., Bilbao, J., 2001. Local Bed Voidage in Spouted Beds. *Industrial & Engineering Chemistry Research* 40, 427-433.
- Palis, S., Kienle, A., 2012. Stabilization of continuous fluidized bed spray granulation with external product classification. *Chem Eng Sci* 70, 200-209.
- Rao, A., Curtis, J.S., Hancock, B.C., Wassgren, C., 2010. The Effect of Column Diameter and Bed Height on Minimum Fluidization Velocity. *AIChE Journal* 56, 2304-2311.
- Rees, A.C., Davidson, J.F., Dennis, J.S., Fennell, P.S., Gladden, L.F., Hayhurst, A.N., Mantle, M.D., Muller, C.R., Sederman, A.J., 2006. The nature of the flow just above the perforated plate distributor of a gas-fluidised bed, as imaged using magnetic resonance. *Chem Eng Sci* 61, 6002-6015.

- Roy, D., Larachi, F., Legros, R., Chaouki, J., 1994. A Study of Solid Behavior in Spouted Beds Using 3-D Particle Tracking. *Can J Chem Eng* 72, 945-952.
- Ruoyo, H., Hongzhong, L., Maoyu, C., Jiyu, Z., 1996. Numerical simulation and verification of a gas-solid jet fluidized bed. *Powder Technol.* 87, 73-81.
- San José, M.a.J., Olazar, M., Alvarez, S., Izquierdo, M.A., Bilbao, J., 1998. Solid cross-flow into the spout and particle trajectories in conical spouted beds. *Chem Eng Sci* 53, 3561-3570.
- San José, M.J., Alvarez, S., Morales, A., Olazar, M., Bilbao, J., 2006. Solid Cross-Flow into the Spout and Particle Trajectories in Conical Spouted Beds Consisting of Solids of Different Density and Shape. *Chemical Engineering Research and Design* 84, 487-494.
- San José, M.J., Olazar, M., Llamosas, R., Izquierdo, M.A., Bilbao, J., 1996. Study of dead zone and spout diameter in shallow spouted beds of cylindrical geometry. *The Chemical Engineering Journal and the Biochemical Engineering Journal* 64, 353-359.
- Sánchez-Delgado, S., Marugán-Cruz, C., Acosta-Iborra, A., Santana, D., 2010. Dense-phase velocity fluctuation in a 2-D fluidized bed. *Powder Technol.* 200, 37-45.
- Sasic, S., Leckner, B., Johnsson, F., 2006. Time-frequency investigation of different modes of bubble flow in a gas-solid fluidized bed. *Chem. Eng. J.* 121, 27-35.
- Scarano, F., 2002. Iterative image deformation methods in PIV. *Meas. Sci. Technol.* 13, R1-R19.
- Smith, J.W., 1975. Spouted beds, Kishan B. Mathur and Norman Epstein, Academic Press, Inc., New York(1974). 304 pages. *AIChE Journal* 21, 623-623.
- Stein, M., Seville, J.P.K., Parker, D.J., 1998. Attrition of porous glass particles in a fluidised bed. *Powder Technol.* 100, 242-250.
- Sung, J.S., Burgess, J.M., 1987. A Laser-Based Method for Bubble Parameter Measurement in Two-Dimensional Fluidized-Beds. *Powder Technol.* 49, 165-175.
- Sutanto, W., Epstein, N., Grace, J.R., 1985. Hydrodynamics of Spout-Fluid Beds. *Powder Technol.* 44, 205-212.
- Thorley, B., Saunby, J.B., Mathur, K.B., Osberg, G.L., 1959. An analysis of air and solid flow in a spouted wheat bed. *The Canadian Journal of Chemical Engineering* 37, 184-192.
- Thorpe, R.B., Davidson, J.F., Pollitt, M., Smith, J., 2002. Maldistribution in fluidized beds. *Industrial & Engineering Chemistry Research* 41, 5878-5889.
- Tsuji, T., Uemaki, O., 1994. Coal-Gasification in a Jet-Spouted Bed. *Can J Chem Eng* 72, 504-510.

- Uemaki, O., Tsuji, T., 1992. Particle-Velocity and Solids Circulation Rate in a Jet-Spouted Bed. *Can J Chem Eng* 70, 925-929.
- van Buijtenen, M.S., Börner, M., Deen, N.G., Heinrich, S., Antonyuk, S., Kuipers, J.A.M., 2011a. An experimental study of the effect of collision properties on spout fluidized bed dynamics. *Powder Technol.* 206, 139-148.
- van Buijtenen, M.S., Buist, K., Deen, N.G., Kuipers, J.A.M., Leadbeater, T., Parker, D.J., 2011b. Numerical and experimental study on spout elevation in spout-fluidized beds. *AIChE Journal*, n/a-n/a.
- van Deemter, J., 1967. The counter-current flow model of a gas-solids fluidized bed. *Proceedings of the international symposium on fluidization*, 334-347.
- van Ommen, J.R., Sasic, S., van der Schaaf, J., Gheorghiu, S., Johnsson, F., Coppens, M.-O., 2011. Time-series analysis of pressure fluctuations in gas–solid fluidized beds – A review. *Int. J. Multiph. Flow* 37, 403-428.
- Van Velzen, D., Flamm, H.J., Langenkamp, H., Casile, A., 1974. Motion of solids in spouted beds. *The Canadian Journal of Chemical Engineering* 52, 156-161.
- Waldie, B., Wilkinson, D., Mchugh, T.G.P., 1986. Measurement of Voidage in the Fountain of a Spouted Bed. *Can J Chem Eng* 64, 950-953.
- Wang, F., Yu, Z., Marashdeh, Q., Fan, L.-S., 2010. Horizontal gas and gas/solid jet penetration in a gas–solid fluidized bed. *Chem Eng Sci* 65, 3394-3408.
- Wang, S.N., Xu, J., Wei, W.S., Shi, G., Bao, X.J., Bi, H.T., Lim, C.J., 2000. Gas spouting hydrodynamics of fine particles. *Can J Chem Eng* 78, 156-160.
- Wilkinson, D., 1995. Determination of Minimum Fluidization Velocity by Pressure Fluctuation Measurement. *Can J Chem Eng* 73, 562-565.
- Wormsbecker, M., van Ommen, R., Nijenhuis, J., Tanfara, H., Pugsley, T., 2009. The influence of vessel geometry on fluidized bed dryer hydrodynamics. *Powder Technol.* 194, 115-125.
- Yang, W.-C., Keairns, D.L., 1982. Solid entrainment rate into gas and gas—solid, two-phase jets in a fluidized bed. *Powder Technol.* 33, 89-94.
- Yin, X.L., Wu, C.Z., Zheng, S.P., Chen, Y., 2002. Design and operation of a CFB gasification and power generation system for rice husk. *Biomass Bioenerg* 23, 181-187.
- Zhang, Y.M., Bi, H.T., Grace, J.R., Lu, C.X., 2010. Comparison of Decoupling Methods for Analyzing Pressure Fluctuations in Gas-Fluidized Beds. *AIChE Journal* 56, 869-877.

Zhao, X.L., Li, S.Q., Liu, G.Q., Song, Q., Yao, Q., 2008. Flow patterns of solids in a two-dimensional spouted bed with draft plates: PIV measurement and DEM simulations. *Powder Technol.* 183, 79-87.

Zhou, J., Grace, J.R., Lim, C.J., Brereton, C.M.H., Qin, S., Lim, K.S., 1995. Particle Cross-Flow, Lateral Momentum Flux and Lateral Velocity in a Circulating Fluidized-Bed. *Can J Chem Eng* 73, 612-619.

Figures and Tables

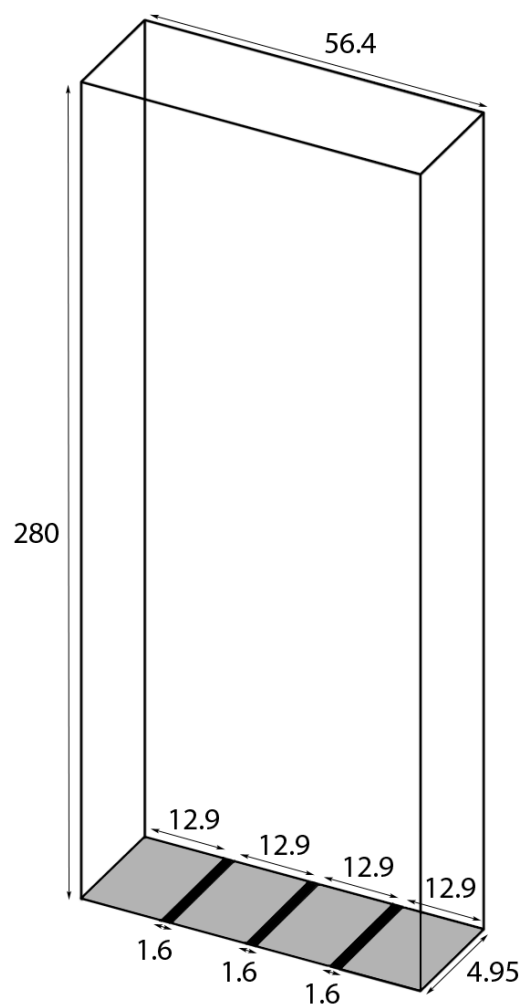


Figure 1: Schematic of the 2-D flat bottom rectangular column setup with dimensions in mm.

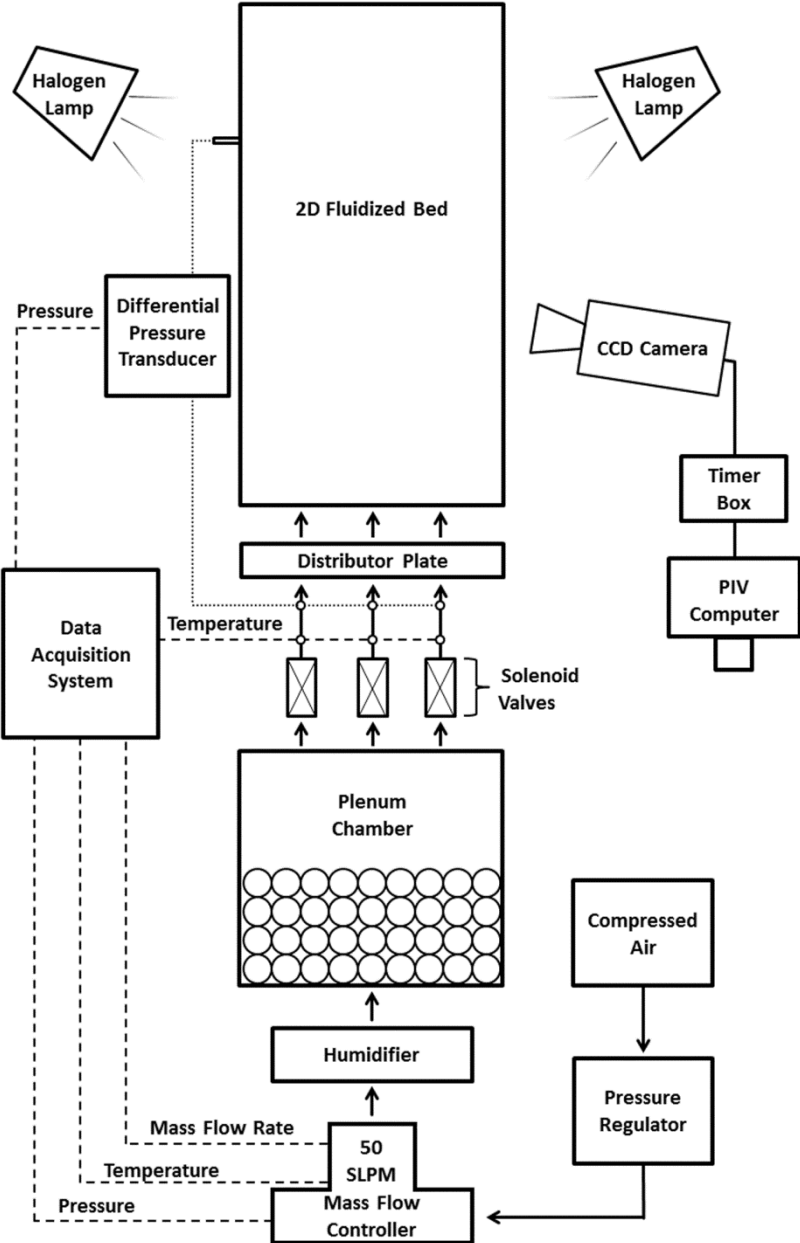


Figure 2: Diagram of the experimental setup.

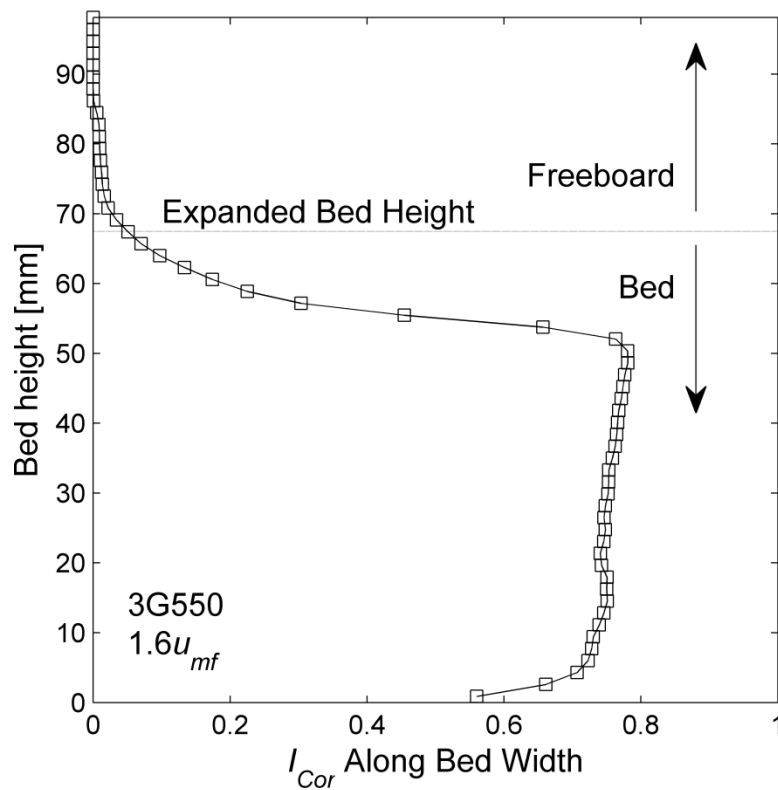


Figure 3: Corrected intensity, I_{cor} , averaged along the vertical height of the bed for 3G550 at $1.6 u_{mf}$ to define the expanded bed height.

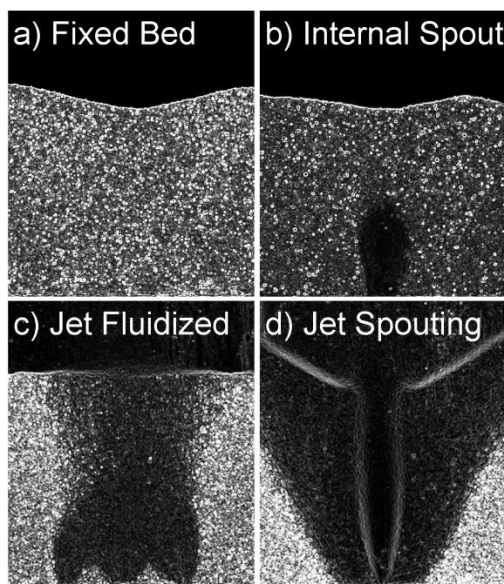


Figure 4: Mean Prewitt high pass filtered PIV images of the various flow regimes: a) Fixed Bed, b) Internal Spout, c) Jet Fluidized, and d) Jet Spouting.

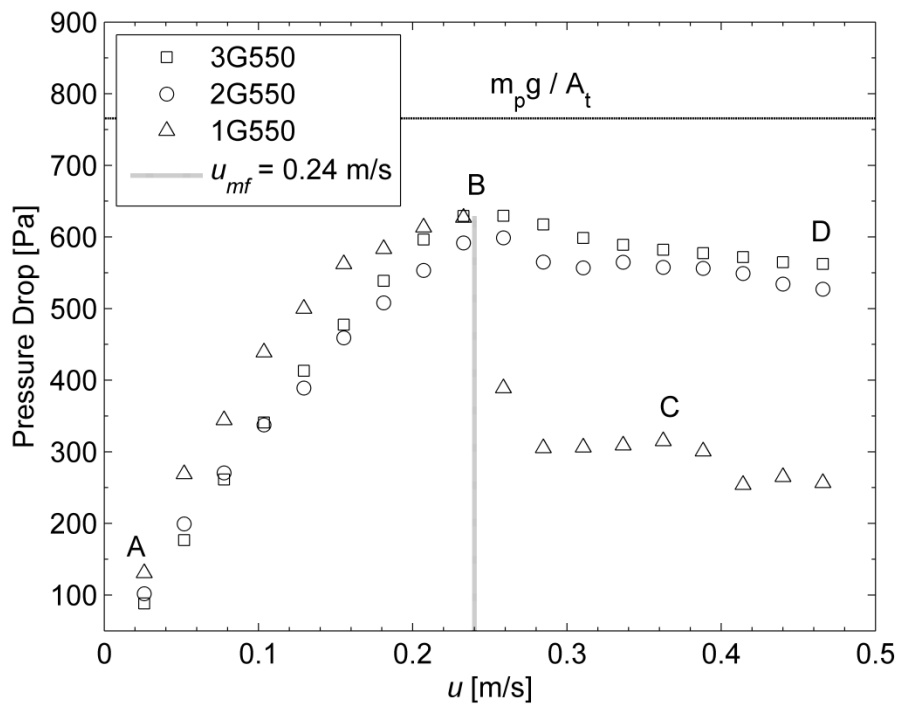


Figure 5: Differential pressure measurements for G550 using the pressure drop method to define the onset of the minimum fluidization velocity, u_{mf} .

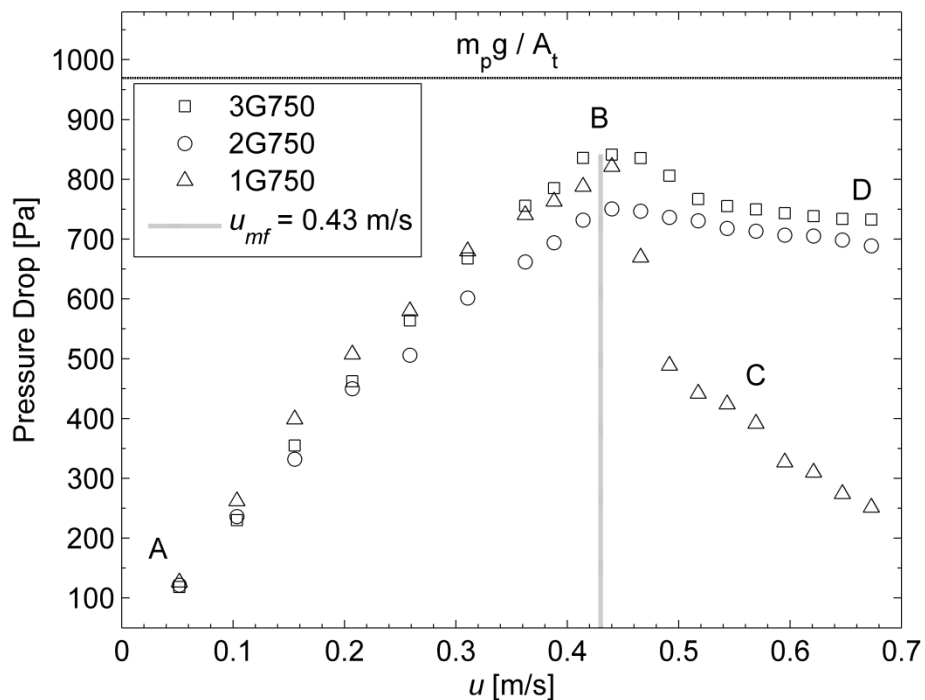


Figure 6: Differential pressure measurements for G750 using the pressure drop method to define the onset of the minimum fluidization velocity, u_{mf} .

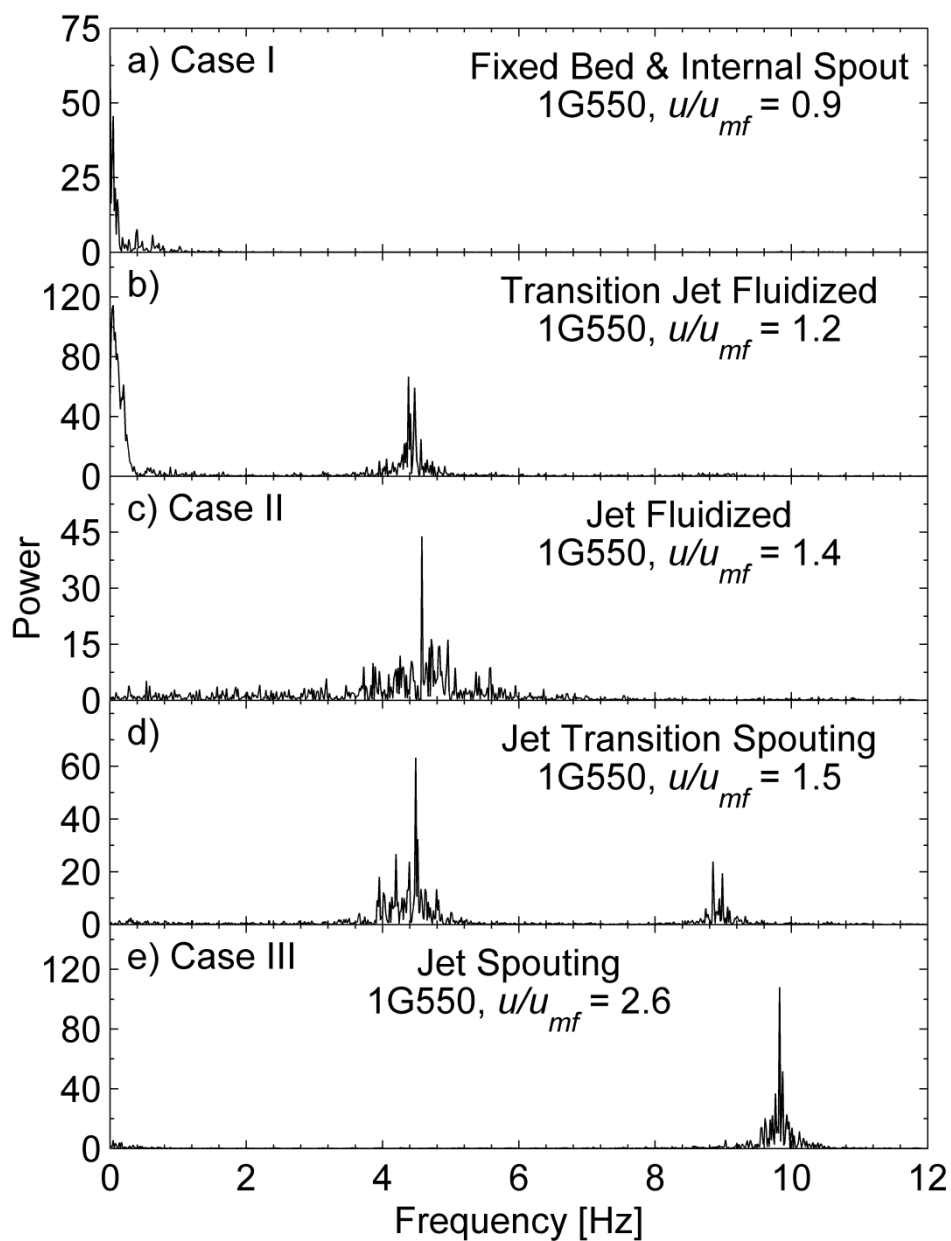


Figure 7: Dominant frequencies in the power spectrum from the differential pressure measurements used to classify the flow regimes: a) Fixed Bed and Internal Spout, b) Transition Jet Fluidized, c) Jet Fluidized, d) Jet Transition Spouting, and e) Jet Spouting.

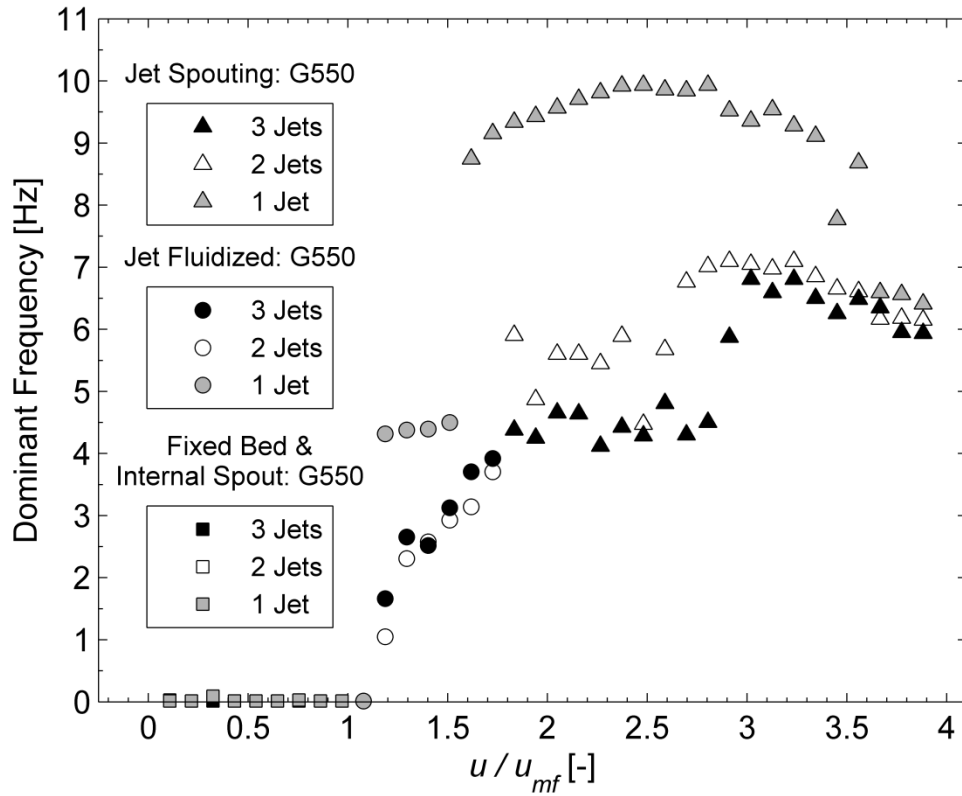


Figure 8: Effect of superficial gas velocity on the dominant frequencies for the G550 multiple jet systems.

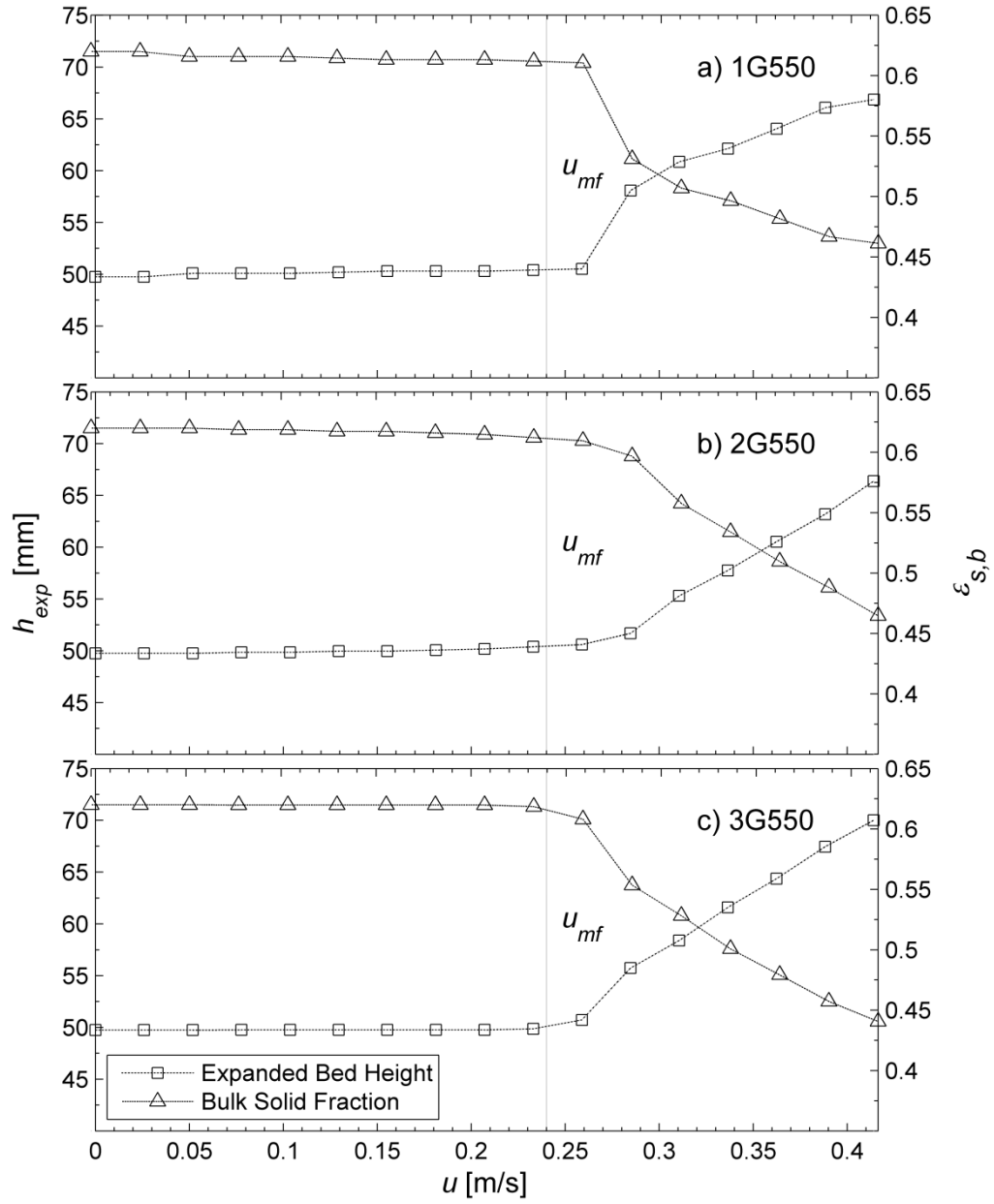


Figure 9: Expanded bed heights, h_{exp} , and bulk solid fractions, $\epsilon_{s,b}$, for Case I and II as a function of G550 inlet gas velocities for: a) a single jet, b) double jet, and c) triple jet system.

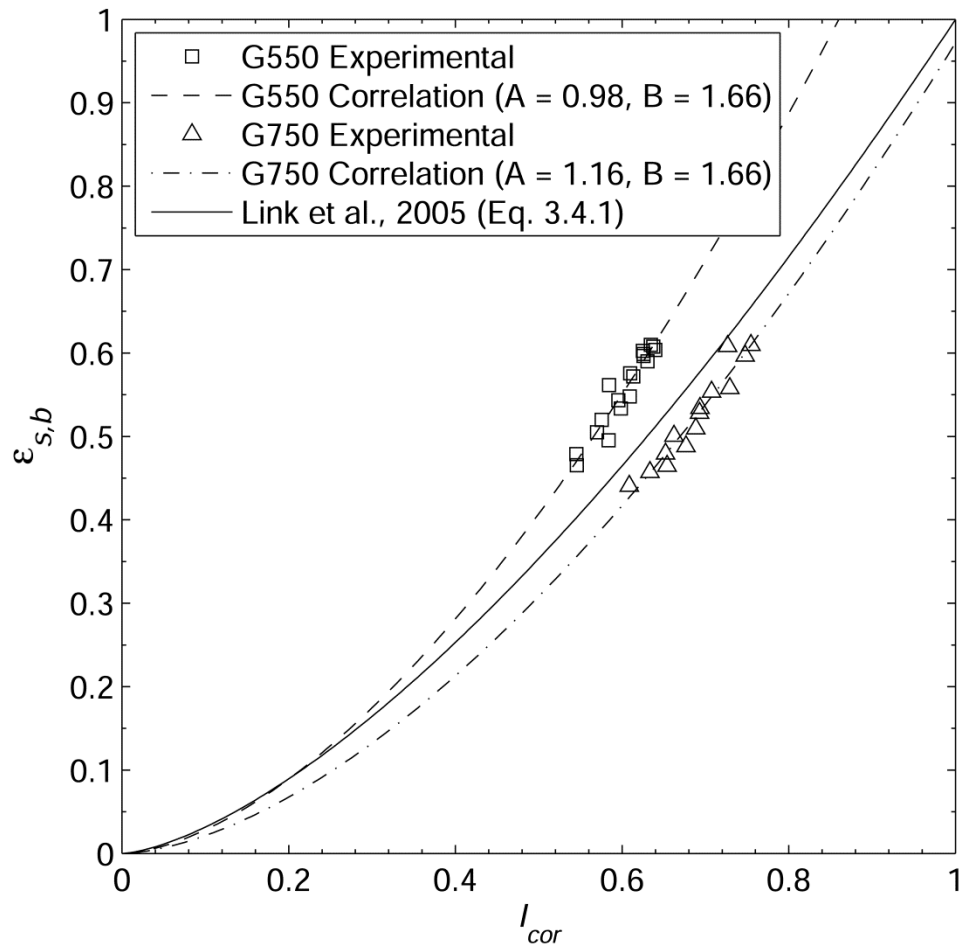


Figure 10: Solid volume fraction, ε_s , correlation for G550 and G750 particulates classified in the jet fluidized regime in comparison to Equation 3.4.1.

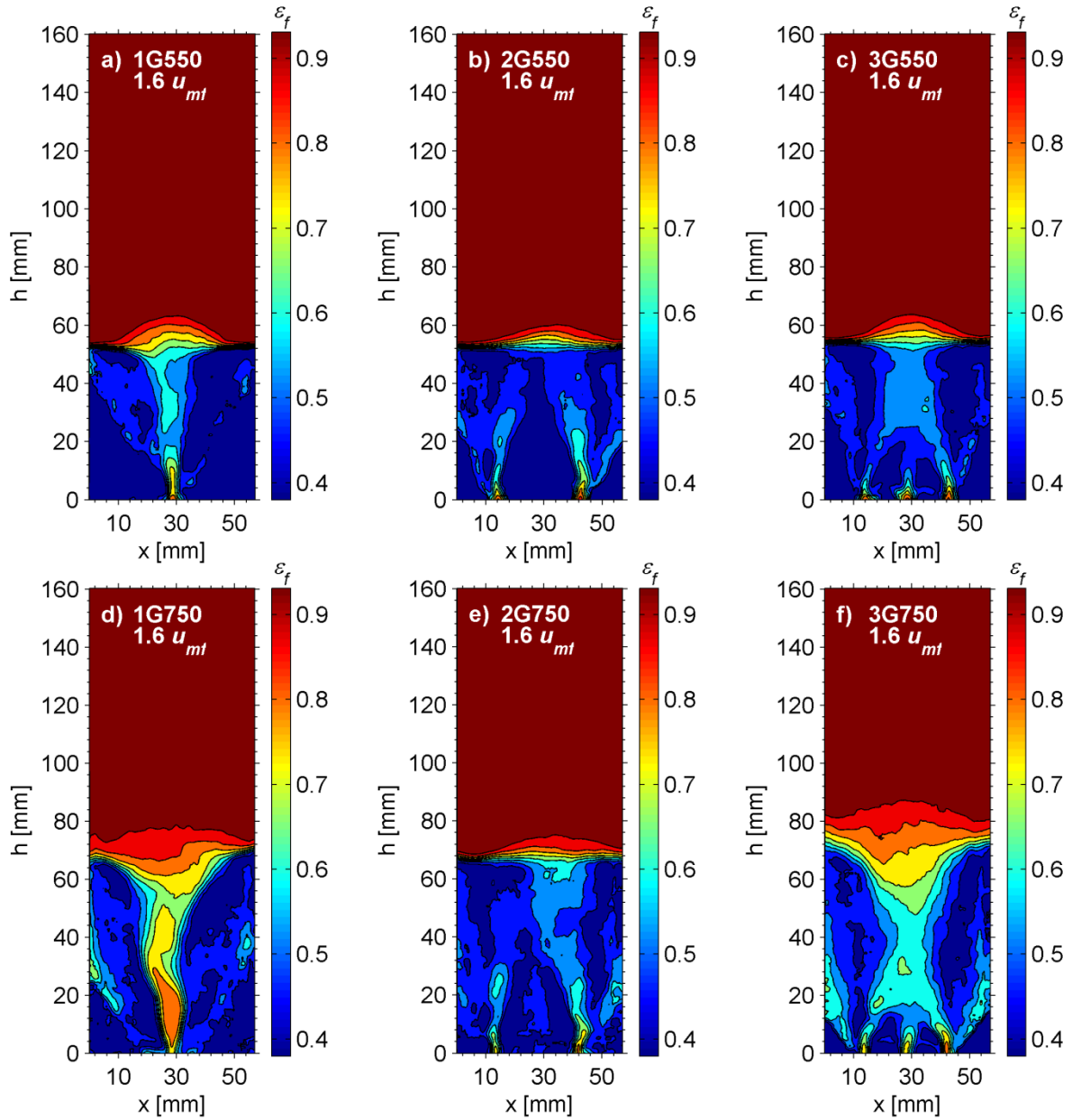


Figure 11: Localized mean gas void fraction, ε_f , distributions at $1.6 u_{mf}$, for: a) 1G550, b) 2G550, c) 3G550, d) 1G750, e) 2G750, and f) 3G750.

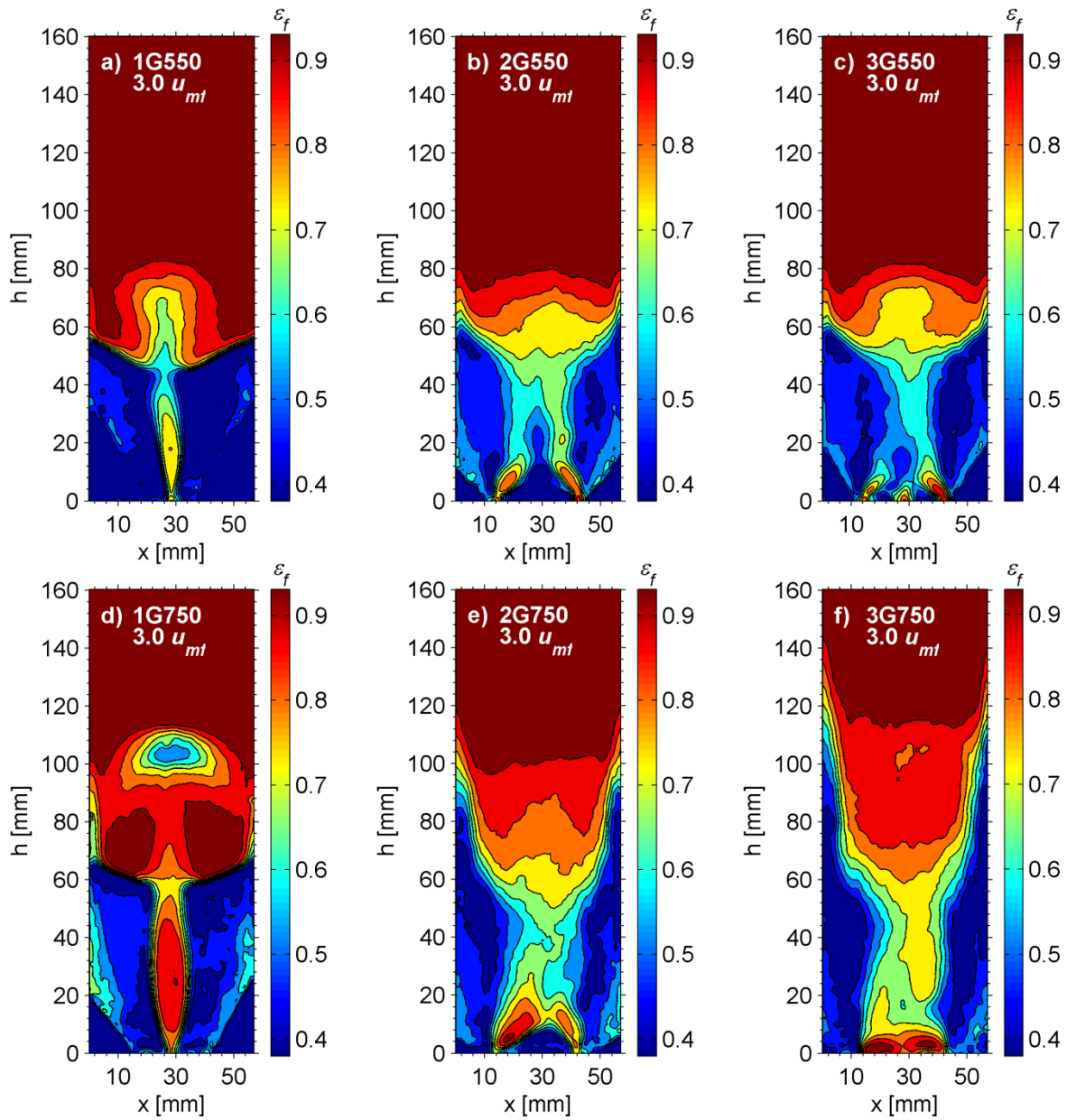


Figure 12: Localized mean gas void fraction, ε_f , distributions at $3.0 u_{mf}$, for: a) 1G550, b) 2G550, c) 3G550, d) 1G750, e) 2G750, and f) 3G750.

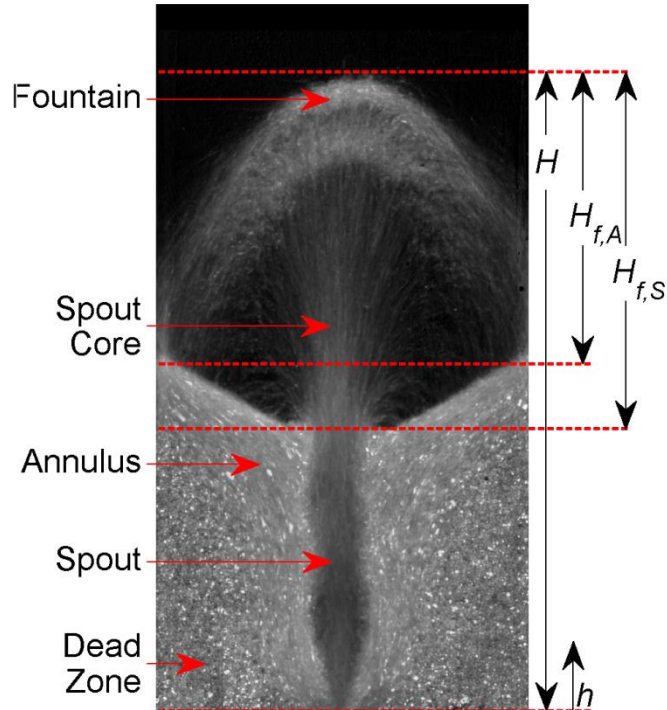


Figure 13: Instantaneous single jet I_{cor} image showing the annulus, spout, and fountain regions.

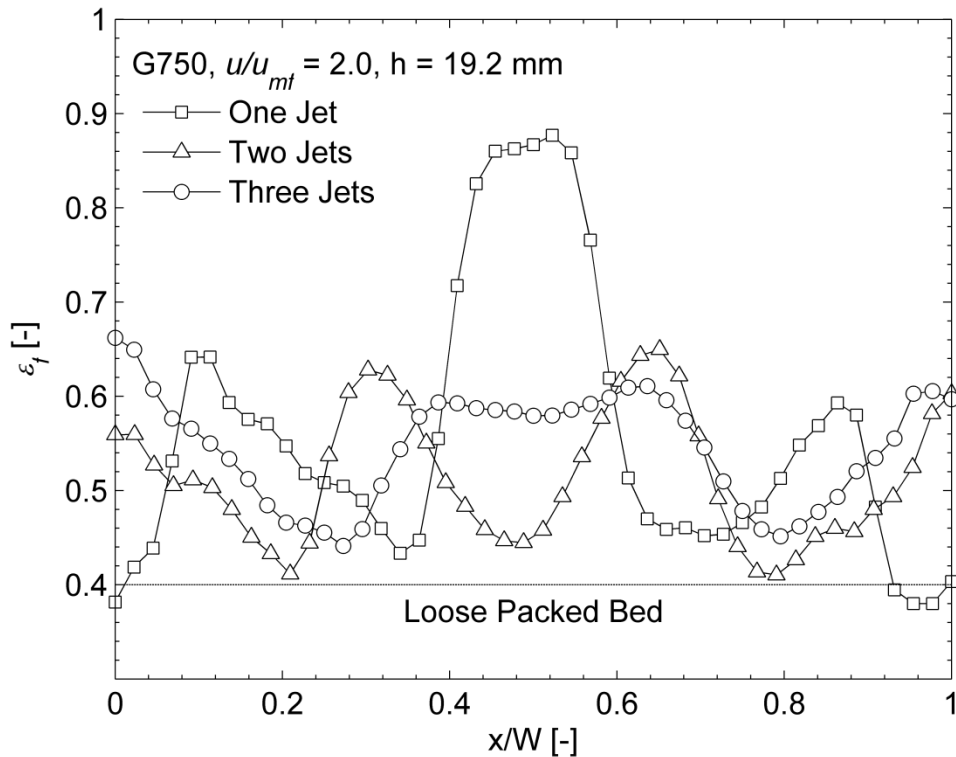


Figure 14: Axial gas void fraction, ϵ_f , distributions at $2.0 u_{mf}$ and a bed height of 19.2 mm above the distributor plate for one, two, and three jet G750 systems.

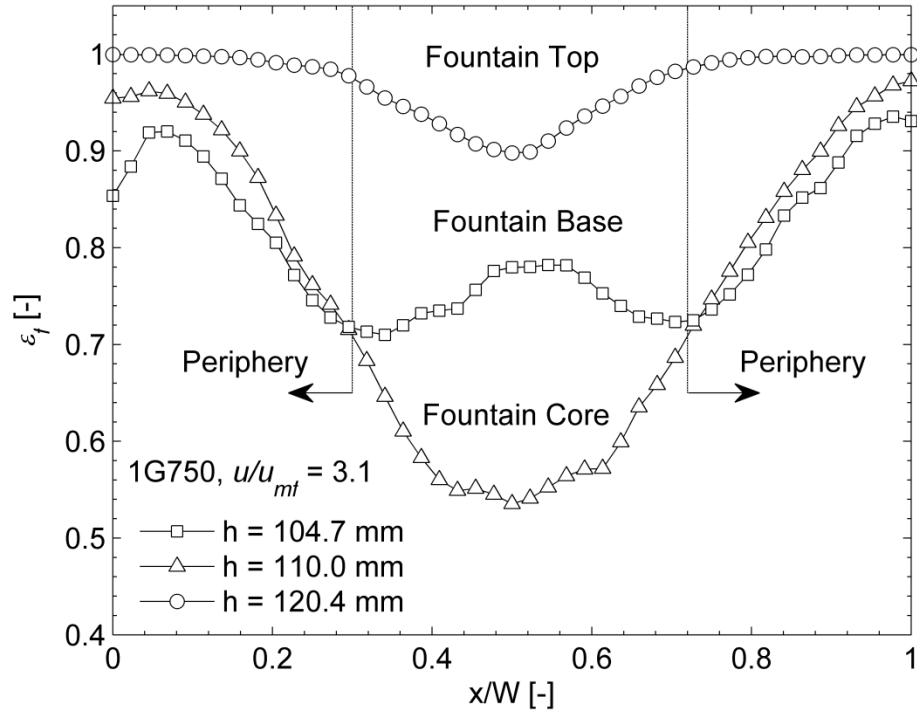


Figure 15: Axial gas void fraction, ε_f , distributions in the fountain region at $3.1 u_{mf}$ and bed heights of 104.7 mm, 110.0 mm, and 120.4 mm for 1G750.

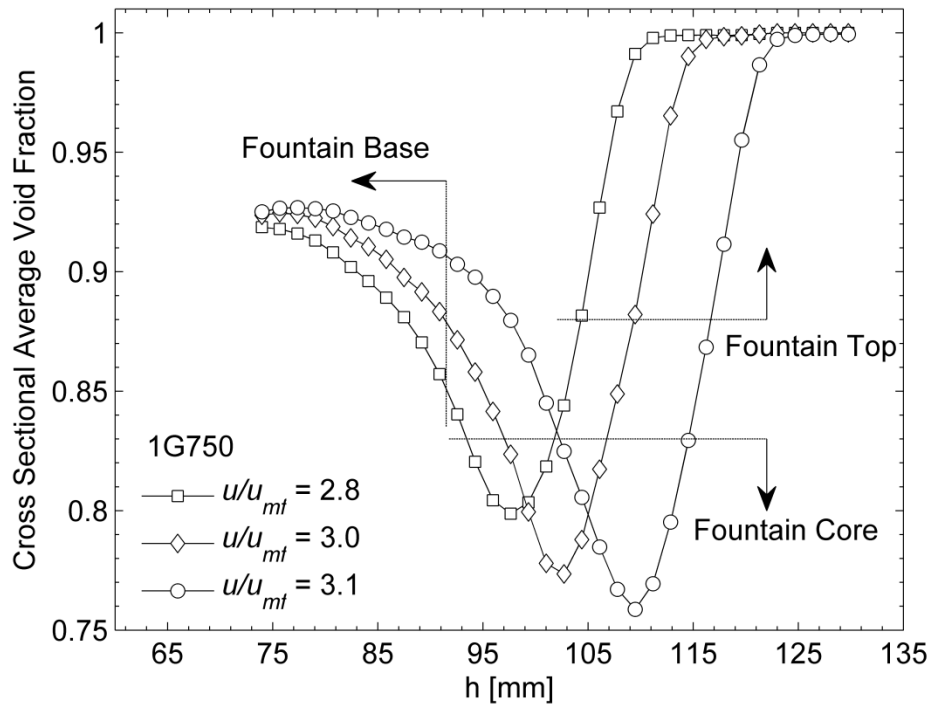


Figure 16: Cross sectional averaged gas void fractions, ε_f , in the fountain region at $2.8 u_{mf}$, $3.0 u_{mf}$, and $3.1 u_{mf}$.

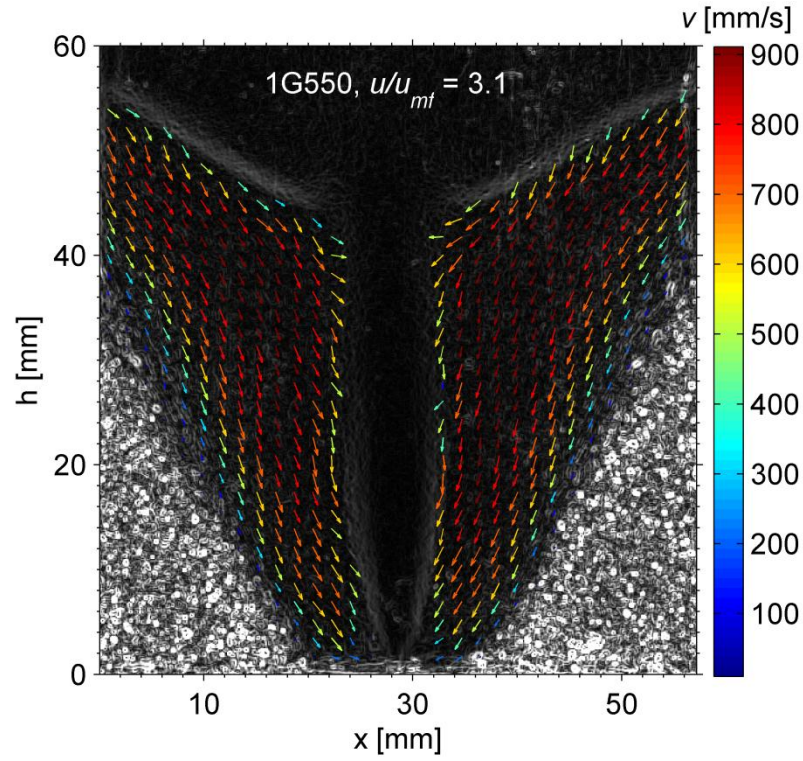


Figure 17: Mean Prewitt high passed filtered image overlaid with corresponding annulus velocity vectors at $3.1 u_{mf}$.

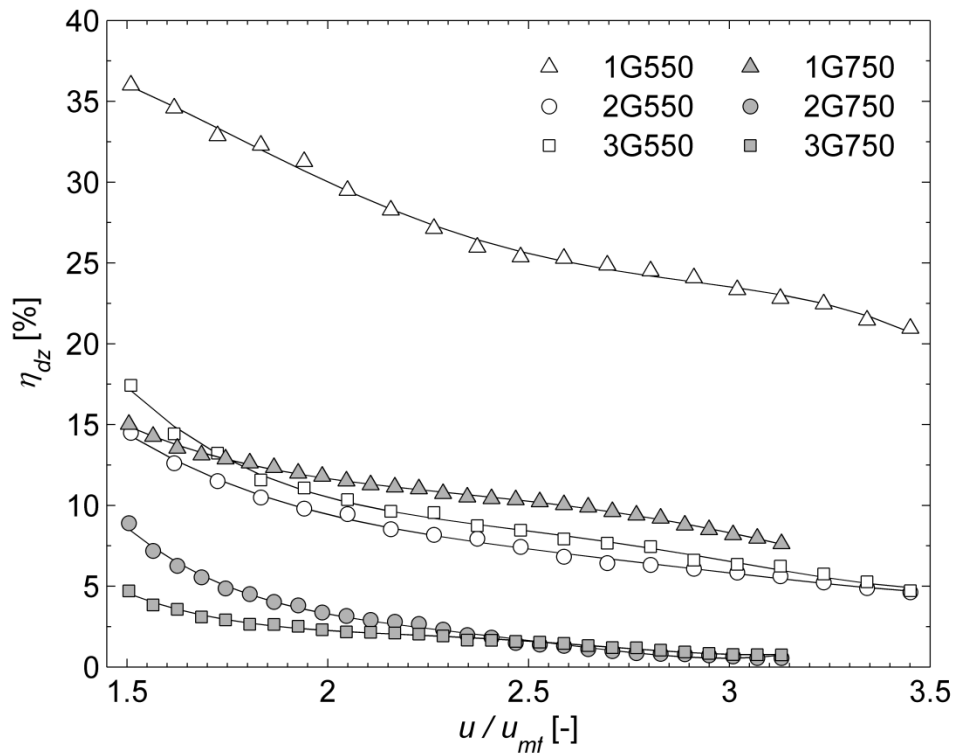


Figure 18: Dead zone mass fractions, η_{dz} , for G550 and G750 in one, two, and three jet systems.

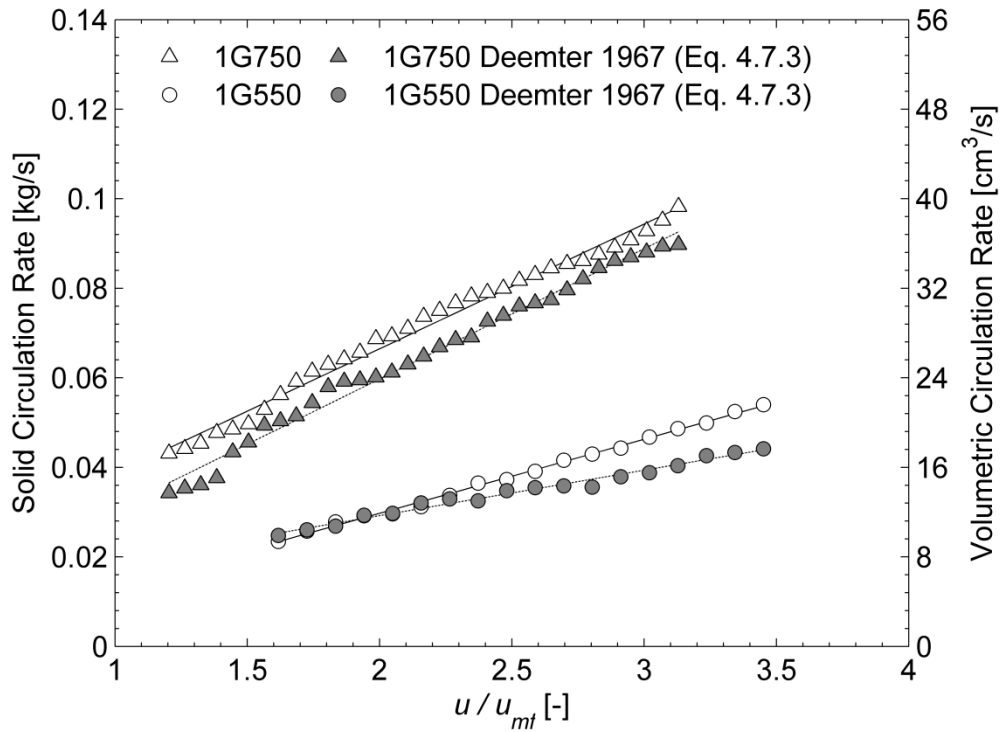


Figure 19: Solid, \dot{m}_{tot} , and volumetric, \dot{V}_{tot} , circulation rates for 1G550 and 1G750 in comparison with counter-current model of Equation 4.7.3

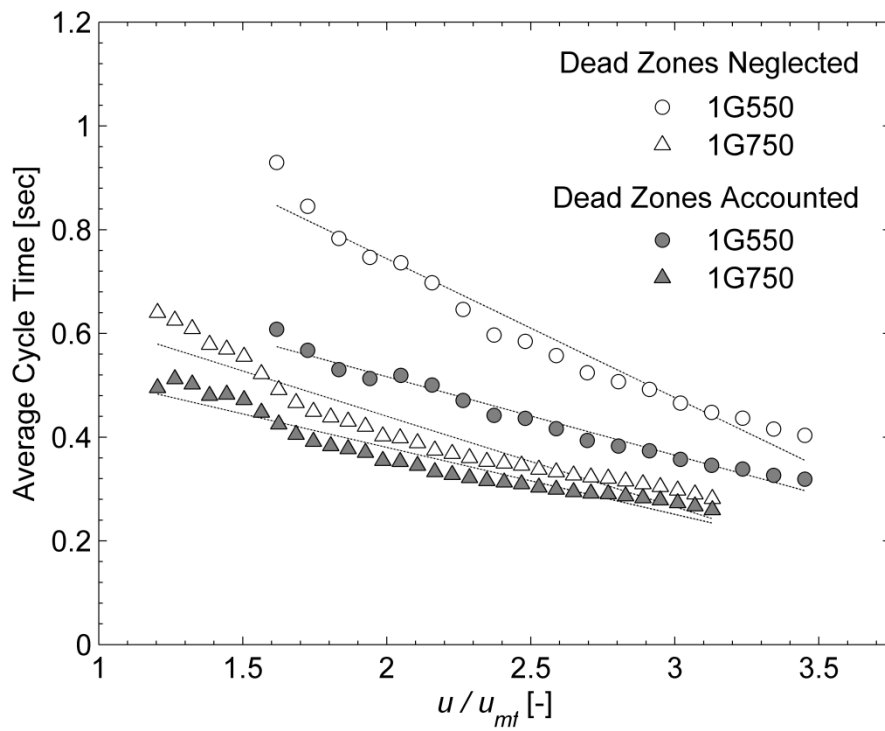


Figure 20: Average particle cycle times compared between neglecting and accounting for total dead zone mass.

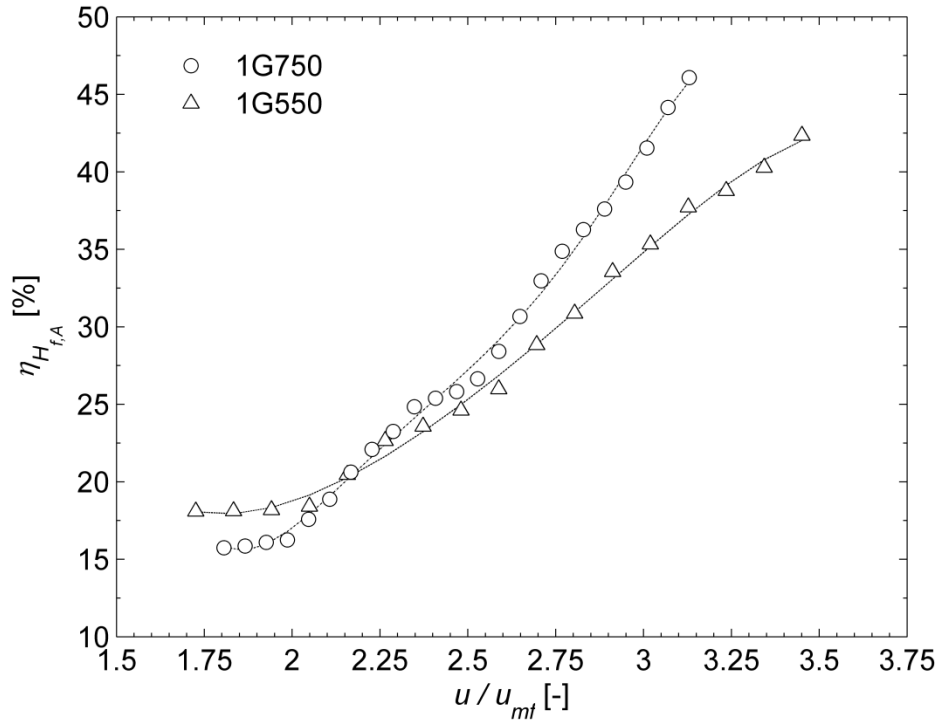


Figure 21: Effect of superficial gas velocity on fountain height expansion ratios, $\eta_{H_{f,A}}$, defined from the top of the annulus, for G550 and G750 systems.

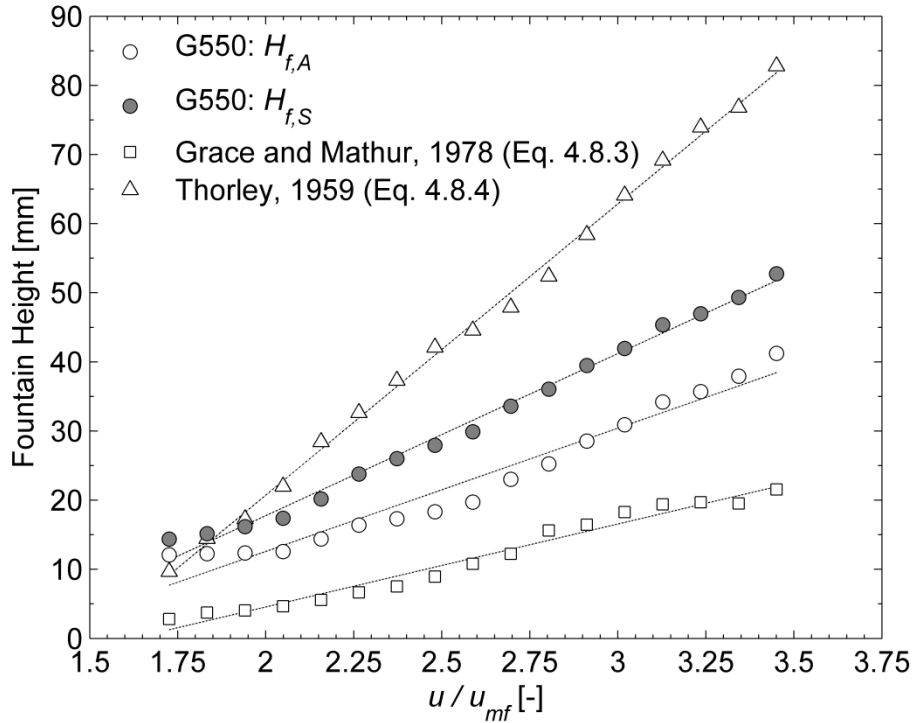


Figure 22: Experimental fountain height compared with the force balance analyses of Equations 4.8.3 and 4.8.4.

Table 1. Properties of experimental fluidized bed media.

Property	Small Particles	Large Particles
Notation	G550	G750
Geldart Group	B	D
Number of Particles	100,000	50,000
D_p [μm]	550	750
ρ_p [kg m^{-3}]	2500	2500
ϕ_s [-]	1	1
u_{mf} [m s^{-1}]	0.24	0.43
ε_s^{max} [-]	0.38	0.38
$P_{max,avg}$ [Pa]	490	472

Table 2. Minimum fluidization velocities found in literature for glass Geldart B and D particle classifications.

Reference	Bed Design	Material	Geldart Group	ρ_p [kg m^{-3}]	d_p [μm] ^a	u_{mf} [m s^{-1}]
(Franka et al., 2007)	Column Fluidized	Glass	B	2600	550	0.20
(Rao et al., 2010)	Column Fluidized	Glass	B	2500	550	0.25
(Çeçen, 1994)	Semi-Cylindrical Spouted	Glass	B	2491	450	0.15
		Glass	D	2464	651	0.28
(Agarwal et al., 2011a)	2-D Fluidized	Glass	B	2500	550	0.22
		Glass	D	2500	750	0.35
(Laverman et al., 2008)	2-D Fluidized	Glass	B	2500	500	0.18
Found in this study	2-D Fluidized & Spouted	Glass	B	2500	550	0.24
		Glass	C	2500	750	0.43

^a Mean particle diameter

Chapter 3

Transient Bed-to-Wall Heat Flux Measurements in Fluidized and Spouted Beds

Abstract

An experimental procedure is described to quantify the bed-to-wall heat transfer maps in spouted, fluidized, and fixed beds. The technique is based off an inverse heat conduction problem designed to overcome the spatial, time varying, and instrumental intrusive limitations often found in multiphase flow heat transfer measurements. Attention is paid to the data processing methods, the effects of added high emissivity wall paint, and the signal to noise ratio found in infrared thermography. The method is validated through a pseudo 2-D fluidized experimental bed, by varying the number of inlet jets, particle size, and flow regimes. The analysis exposed jet interaction, spout fountain heat flux profiles, and enlarged gas inlet thermal gradients for increased particulate size. The dominant source of heat transfer to the wall was found from the convection of the inlet gas and the downward transport of the solid particles.

Submitted for review to the International Journal of Heat and Mass Transfer, June 2012

Corresponding Author: Steven L. Brown

Co-Author: Brian Y. Lattimer

1. Introduction

Fluidized and spouted beds are well acknowledged for their vigorous mixing in multiphase processing. The large interfacial area of solid particulates allows for intensive heat and mass transfer, promoting near isothermal conditions. These beds have wide spread application from catalytic pyrolysis (Bilbao et al., 1989) to gasification (Tsuji and Uemaki, 1994), and chemical processing (Fayed and Otten, 1997). The current advancements in Computational Fluid Dynamic (CFD) models demand validation with quantifiable, accurate, and detailed experiments.

Several heat transfer studies in both fluidized and spouted bed regimes can be found throughout literature. Yet, the vast majority of these studies use single point probes to quantify the heat transfer characteristics. Due to the ease of heat transfer measurements, thermocouples are commonly used in spouted (Klassen and Gishler, 1958), fluidized (Petrovic and Thodos, 1968), and fixed beds (Pons et al., 1993). These measurements provide beneficial data but lack spatial variation, and are most often limited to providing an averaged heat transfer rate.

The conditions inside a steady-state and perforated-plate bed can be considered nearly isothermal (Kunii and Levenspiel, 1991). In this instance it is sufficient to use a single point measurement, such as thermocouples, to sample temperature. However, this method is not adequate for measuring localized conditions under a transient state. Instead large fluidized beds typically use arrays of thermocouples which are distributed over the whole reactor (Werther, 1999). A significant deviation in the local hydrodynamics would occur if this same measurement procedure was applied to small laboratory sized beds.

Furthermore, varying hydrodynamic characteristics are found in the different regions within each flow regime. This makes the multiphase heat transfer a complex problem. To simplify this issue Kunii and Levenspiel (1991) broke-down the heat transfer analysis into two parts: gas-to-particle and bed-to-surface. In order to compute local convective bed-to-wall heat transfer coefficients

$$h_{bw}(t) = q''_{bw}(t) / (T_w(t) - T_b(t)) \quad (1.1)$$

it is essential to know the instantaneous heat flux, q''_{bw} , distribution and time varying surface temperature, T_w , along the outer wall. Additionally, the knowledge of q''_{bw} is desirable when computing the near wall conductivity of the bulk region adjacent to the wall for CFD simulations

(Yusuf et al., 2012), as it can significantly differ from the true thermal conductivity of the fluidized material.

Early studies by Malek and Lu (1964) have discretized the walls of two cylindrical spouted beds into five sections. Each section was fitted with thermocouples and a water cooled tight jacket to measure the rate of energy change at the wall. The technique was successfully implied in measuring q''_{bw} but was limited to steady-state bed conditions and a five region analysis. It was also noted that the size of the intrusive thermocouples considerably decreased the height of the spout and promoted spout swaying.

More commonly, experimental heat transfer models in literature study the effects of the wall-to-bed heat flux through the use of a heated wall (Chatterjee et al., 1983; Yusuf et al., 2012). These studies are often limited to a constant surface heat flux or temperature distribution. A transient measurement of the emulsion heat transfer was studied in Gloski et al. (1984) by applying an instantaneous electrical power dissipation to a thin foil heater. While these studies provide valuable information, they are restricted to bed temperatures operating below the wall temperature.

Very few studies examine the time-wise variations of local heat flux measurements at elevated bed temperatures. Instantaneous readings have been made with heat flux gauges in fluidized beds. Saxena et al. (1989) gave a review of thermopile type gauges used to capture the temperature differences across a thin surface with known thermal properties to compute heat transfer coefficients. However, these gauges require protective sheaths as they are not abrasion resistant and give only a single localized heat flux rate. Another probe based off of the Gardon gauge (Gardon, 1960) was designed to measure heat flux in high temperature beds (Gosmeyer, 1979). However, it was concluded that the gas-solids do not provide a uniform heat flux distribution over the surface of the gauge rendering inconsistent results.

The aim of this study is to apply an innovative, but yet simple approach to measuring transient localized bed-to-wall heat flux distributions in fluidized, spouted, and fixed bed regimes. An energy balance is applied to a wall of a small scaled laboratory bed and is resolved as an inverse heat conduction problem (IHCP). Typically this type of analysis is found in convective heat transfer measurements. An extensive review of these thermo-fluid-dynamic studies can be found in Carlomagno and Cardone (2010).

The advantages of this approach are the measurement techniques are non-intrusive to the flow and are capable of capturing transient bed conditions. Moreover, the detailed localized data needed for the validation of CFD models, such as Discrete Particle Models (DPM), can be captured with respect to time. This study extends on the multiple jet hydrodynamic system previously characterized by Brown and Lattimer (2012).

A description of the non-reacting bed setup and detailed explanation of the energy balance applied in the study is first given. This is followed by an experimental investigation to demonstrate the use of the proposed analysis. The same bed containing of a multiple slit jet system of Brown and Lattimer (2012) is used under hydrodynamic steady-state conditions of the multiphase flow. The heat transfer is then induced by the subjecting the inlet gas to a thermo-transient response which then flows into the ambient temperature bed of particles.

2. Experimental Setup

Experiments were conducted in a pseudo-2D fluidized bed, shown in Figure 1, with cross-sectional dimensions of $X = 56.4$ mm, $D_b = 4.95$ mm and overall bed height, H , of 280 mm. The base entailed of a stainless steel distributor plate with three evenly spaced selectable slit jets of 1.6 mm wide by the full depth of the bed. The outside of the plate was coated with a low thermal conductivity silicone rubber insulation to reduce thermal energy loss. The back and side walls consisted of Polymethyl-Methacrylate coated in paint to ensure surface flatness. The front wall was comprised of a thin, 152 μm , Stainless Steel 304 (SS 304) polished plate with material properties given in Table 1. The plate was secured in tension across to the front of the bed to provide a rigid surface and reduce any bowing effect produced by the mass of the fluidized particulates. A thin uniform coating of matt black paint was applied to the outer wall of the plate to provide a high surface emissivity.

A schematic of the setup is given in Figure 2. Compressed air was used as the fluidization gas and was controlled by a pressure regulator and a 50 SLPM ALICAT (Model # MC-50SLPM-D) mass flow controller with an accuracy of ($\pm 0.4\%$ reading, $+ 0.25\%$ FS). The gas was first channeled through a plenum chamber and controlled by three rapidly responding solenoid valves providing the ability for various jet selections. The gas was then directed through inline mesh heaters each controlled by a variable autotransformer with a maximum capacity of 2.0 kVA.

Chromel-Alumel (Type K) bare bead thermocouples were located near the top of the distributor plate just below the gas inlet of each slot jet to measure inlet gas temperature, T_{in} (K). Two thermocouples were positioned at a height of 174 mm upstream of the distributor plate in the freeboard region, while two additional thermocouples were also placed just above the maximum expanded bed height of each experimental test case. An additional thermocouple was positioned outside the bed near the front wall to measure the ambient temperature, T_{amb} (K). A 32 bit National Instrument cDAQ-9174 chassis was used with a NI-9123 card to record the thermocouple data at 10 Hz under a high-resolution mode providing a measurement sensitivity less than 0.02 °C.

A FLIR SC655 Infrared (IR) camera, operating in the 7.5 - 13.0 μm range, was directly placed perpendicular to the painted stainless steel foil at front wall of the bed to capture local temperature distributions. The area surrounding the fluidized bed was enclosed in a black body box with an opening for the IR camera lens to prevent external radiation reflections. The sampling frequency of the IR camera was set at 200 Hz while the 24.5 mm lens provided a resolution of 640 x 120 pixels or about 510 μm per pixel. A calibration between the camera and the high emissivity paint was conducted prior to the experimental tests to ensure accurate measurements. Thermocouples were applied to the front wall of the bed and a thin filmed strip heater to the back. The surrounding sides of the plate were insulated with a ceramic fiber while the front side remained open to the atmosphere. Once the plate was heated to near steady-state and isothermal conditions, the difference between the thermocouples and IR camera measurements were used with the FLIR ExaminIR Max 1.30.0 software to compute the emissivity of the matt black paint. The temperature uncertainty was estimated at ± 0.2 °C in the range from 20 to 100 °C. The resulting surface emissivity of the painted plate was found as 0.95 ± 0.02 .

The top of the distributor plate was covered by a fine mesh screen and the bed was filled with glass particles. Two types of particles were used to explore the effects of particle size, fluidization regimes, and the number of slit jets used at the distributor plate. The particles were in the Geldart B and C classification with mean diameters, D_p , of 550 μm and 750 μm respectively. The minimum fluidization velocity, u_{mf} (m s^{-1}), for each particle type was previously found by Brown and Lattimer (2012) through applying a differential pressure drop analysis and are given in Table 2 along with their physical properties.

The experimental procedure started by first fluidizing the particles with ambient temperature air at over $3 u_{mf}$ and then incrementally dropping the superficial gas velocity. Once the desired inlet gas flowrate was reached, a period of five minutes was allowed for the gas-solid hydrodynamics to reach steady state conditions. Power was then supplied to the inline mesh heaters producing a transient inlet air temperature curve. Figure 3 shows a single jet inlet air temperature distribution with respect to time. It should be noted that the rate of change in the inlet gas temperature varies with the magnitude of the inlet gas velocity. The transient heating of the thin plate is then recorded with the IR camera for a duration of 60 seconds.

3. Data Analysis

An inverse heat conduction analysis was applied to the captured wall temperature profiles to compute localized bed-to-wall heat flux distributions produced by the multiphase flow. A two-dimensional heat transfer model was developed based off of a control volume approach represented in Figure 4. Using conservation of energy, the rate of energy transferred from the fluidized bed to the wall, \dot{E}_{bw} (W), can be defined as:

$$\dot{E}_{bw} = \dot{E}_{st} + \dot{E}_{conv} + \dot{E}_{rad} + \dot{E}_{cond} \quad (3.1)$$

where \dot{E}_{st} , \dot{E}_{conv} , \dot{E}_{rad} , and \dot{E}_{cond} , is the rate of energy stored in the wall, lost through natural convection, lost through radiation, and distributed in the wall through conduction respectfully. The small thickness and high thermal conductivity of the thin plate provided a low Biot number, $Bi < 0.1$. Furthermore, the contact resistance between the plate and a single paint layer has been found negligible also due to a low Biot number (Mehryar, 2006). The temperature distribution was therefore presumed constant across the thickness of the plate, δ_{ss} (m), and paint. Additionally, the normal conduction through the z-direction of the plate and paint was neglected and only the lateral conduction in the x and y-directions was considered.

The thermo-physical effects of the added paint can also be accounted for to reduce uncertainty in the heat transfer analysis. A single coat of acrylic (Nogueira et al., 2003) and matt black (Stafford et al., 2009) paint on stainless steel has been measured as $20 \mu\text{m}$ using Thermal Wave Interferometry (TWI) and as $21.81 \mu\text{m}$ utilizing a microscope respectfully. A paint thickness, δ_p (m), of $20 \mu\text{m}$ was consequently chosen for this study, and the thermal-physical properties were taken from the findings of Raghu and Philip (2006) and are given in Table 1.

With the previous assumptions, Equation 3.1 can be redefined in terms of the heat flux produced at the wall:

$$q''_{bw} = q''_{st} + q''_{rad} + q''_{cond} + q''_{conv} \quad (3.2)$$

where subscripts *bw*, *st*, *rad*, *cond*, and *conv* denote to the bed-to-wall, stored energy, radiation, conduction, and natural convection respectfully. The rate of change of thermal energy stored within the wall was determined as:

$$q''_{st} = (\rho_{ss}c_{p,ss}\delta_{ss} + \rho_p c_{p,p}\delta_p) \frac{\partial T_{x,y}}{\partial t} \quad (3.3)$$

where $T_{x,y}$ (K) is the localized captured wall temperature distribution, ρ (kg m^{-3}) is the density, c_p ($\text{J kg}^{-1}\text{K}^{-1}$) is the specific heat, and subscripts *ss* and *p* respectfully denote to the SS 304 plate and paint. Due to the relatively low temperature profiles examined in this study the material properties were assumed constant. The derivative of the temperature with respect to time was expressed as the temperature difference per unit time, Δt (sec),

$$\frac{\partial T_{x,y}}{\partial t} \cong \frac{\Delta T_{x,y}}{\Delta t} = \frac{T_{x,y}^n - T_{x,y}^{n-1}}{\Delta t} \quad (3.4)$$

The rate of radiation energy lost from the plate to the environment was defined by

$$q''_{rad} = \varepsilon\sigma(T_{x,y}^4 - T_{amb}^4) \quad (3.5)$$

where ε is the emissivity of the paint and σ ($\text{W m}^{-2}\text{K}^{-4}$) is the Stefan-Boltzmann constant. Heat is also lost from the plate to the surrounding air by natural convection. Most empirical correlations on natural convection are based on either uniform temperature or heat flux distributions (Churchill and Chu, 1975). These classical correlations for natural convection along a vertical plate cannot be used in non-uniform temperature distributions without a lack of accuracy. Few works in literature exist on non-isothermal natural convection. An attempt to produce a general series solution based on solving the continuity, momentum, and energy equations was made by Kuiken (1969) in which the wall surface temperature distribution was defined by:

$$T = T_{amb} + r_0\bar{y}^k(1 + a_1\bar{y}^m + a_2\bar{y}^{2m} + \dots) \quad (3.6)$$

where r_0 (K) is a defined temperature, \bar{y} is the normalized length of the plate, and m , a_n are constants. The study resulted in asymptotic solutions for small and large values of \bar{y} . This left a region where neither solutions could be properly applied. To address this issue Na (1977) applied a numerical approach based off of a finite difference method. The non-linear differential

equations were linearized using a Quasilinearization approach (Bellman and Kalaba, 1965). A solution was developed by solving in terms of the Nusselt Number,

$$Nu_y = h_{conv}y / k \quad (3.7)$$

where h_{conv} ($W m^{-2}K$) is the heat transfer coefficient, and the Grashof number,

$$Gr_y = g\beta(T - T_{amb})y^3 / \nu^2 \quad (3.8)$$

where g ($m s^{-2}$) is the nominal acceleration of gravity, and ν ($m^2 s^{-1}$) is kinematic viscosity of the ambient air. The energy lost from natural convection in this study was solved by fitting the instantaneous wall temperature distributions with Equation 3.6 and applying the numerical method of Na (1977). The volumetric thermal expansion coefficient, β (K^{-1}), provides a measure of the degree of expansion based on the temperature change at a constant pressure, P .

For an ideal gas, $\rho = P/RT$, the density depends on the absolute temperature of the fluid:

$$\beta = -\frac{1}{\rho} \left(\frac{\partial \rho}{\partial T} \right)_P = \frac{1}{\rho} \frac{P}{RT^2} = \frac{1}{T} \quad (3.9)$$

where R ($J kg^{-1}K^{-1}$) is the specific gas constant. The absolute temperature can be defined from the mean temperature of the boundary layer over the surface of the plate, known as the film temperature:

$$T_f \equiv (T_{x,y} + T_{amb}) / 2 \quad (3.10)$$

The thermal dependent properties of the air can be expressed as a function of temperature and are given by Incropera and DeWitt (2002). The resulting rate of energy lost from natural convection is given as,

$$q''_{cond} = h_{conv}(T_{x,y} - T_{amb}) \quad (3.11)$$

The temperature gradient within the plate and paint will result in lateral conduction, q''_{cond} , and can be expressed in terms of Fourier's law:

$$q''_{cond} = -(k_{ss}\delta_{ss} + k_p\delta_p) \left(\frac{\partial^2 T_{x,y}}{\partial x^2} + \frac{\partial^2 T_{x,y}}{\partial y^2} \right) \quad (3.12)$$

where k ($W m^{-1}K^{-1}$) is the material thermal conductivity. The heat transfer between neighboring pixels can be approximated in Equation 3.12 using the first two terms of a Taylor series expansion and applying a finite-difference approach. The resulting lateral conduction term can then be further reduced knowing that the pixels represent a square mesh where $\Delta x = \Delta y = \ell$ (m),

$$q''_{cond} = -(k_{ss}\delta_{ss} + k_p\delta_p) \left(\frac{T_{x+\ell,y}^n + T_{x-\ell,y}^n + T_{x,y+\ell}^n + T_{x,y-\ell}^n - 4T_{x,y}^n}{\ell^2} \right) \quad (3.13)$$

This discrete analysis is commonly used in place of the continuous two-dimensional Laplace operator in inverse heat conduction problems. However with low temporal gradients and short pixel spacing, this approach does not allow to satisfy the requirements of stability, uniqueness, and existence (Ilyinsky et al., 1997). Any slight error or noise in the signal will be significantly amplified in the 5 point discrete Laplace operator. To reduce these uncertainties the noise in the temporal data must first be filtered.

Several numerical techniques can be found in literature for filtering a 2D signal. Among the IHCP infrared thermography experiments, Colombo et al. (2008) has applied both a median and a Gaussian filter for reducing spatial and temporal noise. However, a Gaussian filter must be applied with caution as fine detail can be lost in the data due to the ‘blurring’ nature of this filter. A Fourier Transform method has also been investigated (Ilyinsky et al., 1997) for removing high frequency noise components from the signal. A more recent study by Rainieri and Pagliarini (2002) has examined several numerical filters to try to overcome the uncertainties in the IHCP measurements. The use of two consecutive adaptive Wiener filters was highly suggested for recovering the first derivative and restoring the second derivative for the corrected Laplacian. This approach has been used in this study to reduce errors from the signal to noise ratio.

Signal noise is also a product of the fluctuating temperature gradient produced by the transient multiphase flow of the fluidized bed. The high sampling frequency can result in large temporal noise due to this reason. This has been confirmed (Rainieri et al., 2008) in an infrared thermo-graphic system by varying the frame rate. It was concluded that the temporal noise can either be reduced by lowering the frame rate or averaging consecutive frames. In an attempt to further reduce noise in this study, the equated bed-to-wall heat flux was time averaged every second or 200 frames. Figure 5a illustrates the magnitude of neglecting any preprocessing data filtering prior to computing Equation 3.2 in a single jet fluidized bed. The large noise amplification through the discrete Laplacian operator is clearly seen, as only one generalized peak region exists. Applying both the Wiener filter analysis and time averaging, a distinct heat flux profile is identified in Figure 5b.

In addition to increasing the signal to noise ratio, the thermal effects of the paint layer on the lateral conduction analysis must also be taken into consideration to reduce experimental

error. The importance of accounting for this added layer has been studied (Stafford et al., 2009) by impinging air onto a SS 304 plate. Their experiment was performed under steady-state conditions allowing for the time dependent energy stored term to be neglected. Thus, only the lateral conduction term was examined. Their study concluded that the effects of the added paint on the plate in high conductive heat flux profiles could be neglected. However, in low heat transfer regions up to 5.5% of the total heat flux applied to the thin plate was accounted for in lateral conduction term of the paint layer. These findings help show the importance of examining and accounting for the thermal effects in both the plate and added paint in IHCP.

4. Uncertainty Analysis

The uncertainty analysis was based off of measurement resolutions and various material properties. A list of each parameter, p_i , and the corresponding uncertainty value, dp_i , are given in Table 3. The SS 304 material property uncertainty values were given by the supplier and the thermo-physical properties of paint were taken from Raghu and Philip (2006). A worst case approach based off a jitter, or Root Mean Square, analysis was employed (Moffat, 1988),

$$\partial q_{bw}'' = \left[\sum_{i=1}^N \left(\frac{\partial q_{bw}''}{\partial p_i} dp_i \right)^2 \right]^{1/2} \quad (4.1)$$

to compute the overall uncertainty in the bed-to-wall heat flux. A resulting maximum uncertainty of 10.5 % was estimated across all test cases.

5. Variable Impact Discussion

Initial results and discussion focus on the influence of the variables used in the inverse heat conduction problem by analyzing them with experimental data in fluidized and spouted beds. Figure 6 gives mean Prewitt high pass filtered PIV images, taken from Brown and Lattimer (2012) to illustrate the dynamics of an internal spout, multiple jet fluidized bed, and a single jet spouted bed.

5.1 Heat Flux Terms

It is important to quantify the impact of the paint layer, lateral conduction, radiation, convection, and energy stored in the thin-foil during multiphase flow transient experiments. The low temperature, < 400 K, profiles examined in this study resulted in a relatively low energy loss from radiation. Over all experiments performed the maximum percent of the total energy exchange from radiation remained well below 1%. The energy lost through natural convection

was much higher ranging up to a maximum of 23% in the total energy exchange of Equation 3.1. The dominant heat fluxes found in the analysis were the energy stored, q''_{st} , and the lateral conduction, q''_{cond} . The major contributing factors found in each term are described in the following sections.

5.1.1 Energy Stored

The main source of heat flux found at the wall was in terms of the stored energy. The effects of applying a paint layer on q''_{st} in IHCP has not received considerable attention in literature as many studies neglect q''_{st} based on a steady state approach. The effects of neglecting any analysis involving the paint layer are shown in Figure 7, for a single jet in a fluidized regime. Here the highest bed-to-wall heat flux can be seen in Figure 7c at the axial center of the bed, located at the gas inlet. A mean percent error of 11% exists in this region when disregarding the paint layer. From this error less than half a percent is due to the paint in the conduction analysis. This leaves the energy stored as the major contributor to the deviation. This is largely due to the high volumetric capacity of the paint. From a computational point of Equation 3.3, the area heat capacity of the paint used accounts for 18.5% of the magnitude in q''_{st} .

For all jet combinations, particle sizes, and flow regimes tested the percent of the total energy exchanged from the paint layer through lateral conduction remained below 1%. However, the total energy stored in the paint layer ranged up to 17.5%. This finding clearly shows the importance of accounting for the paint layer in Equation 3.2. The maximum percent of the stored energy from the stainless steel plate to the total energy exchanged was up to 79%, making it the largest contributor in the energy analysis as expected.

5.1.2 Lateral Conduction

The effect of neglecting lateral conduction in both the plate and paint layer is also shown in Figure 7. The largest errors in neglecting conduction are found at lower bed heights near the gas inlet. This is attributed by two main reasons in the gas-solid hydrodynamics. The first being high gas void fractions, ε_f , are found at the jet inlet (Brown and Lattimer, 2012). This causes the inlet air to convectively flow directly along the front wall of the bed, producing high rates of energy stored in the wall and large temperature gradients. These gradients directly affect the magnitude of the lateral conduction. Within the jet boundary, located at the center of the bed, a mean error of 40% is seen in Figure 7c when neglecting the lateral conduction, q''_{cond} .

The second reason for high heat flux measurements at the gas inlet is due to particulate dead zones. Gas void fractions equivalent to a packed bed were found in the dead zones (Brown and Lattimer, 2012). This significantly reduces the gas-to-particle convective heat transfer within these regions. A resulting high temperature gradient was found at the wall between the dead zones and the inlet gas channel. Again these areas of large temperature peaks directly result in lateral energy dissipation within the thin plate. A mean absolute error of nearly 230% can be observed in this region when not accounting for q''_{cond} . It should be noted that higher rates of conductive dissipation were found in the plate at lower gas flow rates between the spouting, fluidized, and fixed bed regimes.

At a further height, $h = 32.1$ mm, into the fluidized bed the effects of ignoring q''_{cond} was generally found near the same order of magnitude of the neglected paint layer in the bulk, center region of the bed. This result can be attributed to the lower temperature gradient in the well mixed fluidized bed. At a bed height of $h = 50$ mm, an even smaller temperature gradient exists along the center of the bed. This is a direct result of the large surface area and high heat capacity of the particles causing the portion of the bed directly above the jet to act as a heat sink. With small temperature gradients in the center region of the bed, the dominant error in ignoring q''_{cond} is found near the outer side walls. Here the downward particle entrainment surrounding the jet produces a thermal convective scouring action along the wall. This again increases the temperature gradient. Overall all, the highest percent of q''_{cond} found in the total energy exchanged was near 42%, and less than 1% for the stainless steel plate and paint layer, respectfully.

These same lateral conduction effects can also be seen in a spouting bed. The various structures of a single jet spouting bed are shown in Figure 8 through an instantaneous PIV images given by Brown and Lattimer (2012). The mean error from neglecting conduction over a time span of 60 seconds is shown in Figure 9. This full field view highlights the areas of the largest error found from disregarding the lateral conduction provided by Equation 3.13. A maximum mean error near 450% was found between the gas inlet and the dead zone regions. This was followed by the spout channel, annulus, and fountain core, all with errors well under 100%. The lowest deviations were observed from mid-way up the spout channel to the fountain base in the bulk region.

A similar finding from neglecting conduction terms was found when air was impinged onto a heat plate (Stafford et al., 2009). Errors up to 215% were observed when using a SS 304 plate thickness of 41.3 μm . Another study investigated the thin-foil heat transfer technique in micro-scale air flows (Patil and Narayanan, 2005). Here the magnitude of q''_{cond} was based on an order of magnitude estimate for a 25.4 μm Inconel foil. The conduction heat flux rate was found to be on the same order of magnitude as the net heat flux entering the plate.

These findings emphasize the importance of accounting for the lateral conduction term. It should also be noted for future experiments that it is possible to reduce the magnitude of this term by examining the variables of Equation 3.13. One way of achieving lower conduction would be to position the IR camera at a further distance from the plate. This would increase the distance between neighboring pixels, and thus reduce the magnitude of q''_{cond} . The same effect could also be achieved by spatially averaging n by n pixels. However, both approaches result in a reduction in the spatial resolution. Secondly, designing experiments with small lateral temperature gradients, such as in the well mixed bulk region of a fluidized bed, will have lower wall conduction effects. Thirdly, using a plate with a lower thermal conductivity or thickness would also significantly reduce q''_{cond} . However, the thermal conductivity must remain high enough in comparison to the thickness to assume a lump capacitance model, while the thickness remains suitable to support the dynamics of the multiphase flow. Lastly, the type of paint used and the method of application must be taken into consideration. If the paint grains are distinguished by the IR camera then the signal noise will further be amplified in the conduction term (Mehryar, 2006).

6. Experimental Results and Discussion

Results and discussion on applying the inverse heat conduction analysis to experimental data is given to validate the use of this model in spouted, fluidized, and fixed beds. A transient study and a comparison between a single and double jet system is given in the following sections.

6.1 Transient Heat Transfer Distribution

The time series analysis of a single jet spouting regime at $3 u_{mf}$, in Figure 10, encompasses the transient heat transfer distribution between the spout channel, dead zones, annulus, and fountain regions. An instantaneous PIV image taken from Brown and Lattimer

(2012) is given Figure 8 to illustrate these various regions. At the start of the inlet gas temperature ramp the highest bed-to-wall heat flux is initially produced in the base of the spout channel at the onset of the thermal boundary layer. A significant portion of the gas is found to pass through the spout resulting in high gas void fractions (Brown and Lattimer, 2012). Combining the low gas residence time with the small total surface area of the particulates in the spout, a decrease in q''_{bw} is observed along the axial height of the spout.

With a bed solid circulation rate of 46.8 g/s (Brown and Lattimer, 2012) there is a high particle velocity distribution in the spout with lower particle velocities found in the annulus. The higher heat capacity of the solids and lower particle velocities allows for an increased particle-to-wall heat transfer distribution. The particles produce a convective scouring action which can decrease the film thickness along the wall of the bed. This is in agreement with the conclusion that the proportion of the total upward heat carried by the gas is insignificant in comparison to heat carried downwards by the solids (Epstein and Mathur, 1971).

The particles carried upwards through the spout culminate to form a fountain. The fountain can be divided into two main sections. The first being the core which consists of the solid up-flow and the second region is defined as the periphery which entails of solid particle down-flow returning to the annulus. Often heat transfer models have neglected the fountain and only focused on the annulus and spout (Kmieć, 1980). However it is important to consider this region as it can contain a significant fraction of the total solid particles.

The highest particle concentrations in the fountain can be found along the central axis of the fountain and gradually decrease radially toward the periphery (Brown and Lattimer, 2012). At a further time step, the fountain-to-wall heat transfer is observed.

A higher heat flux is seen in the fountain core, in Figure 10, as the particles temporarily become stagnant due to the change in the vertical velocity direction. The spout channel gas then directly impinges on the suspended particle clusters before moving to the periphery. Here low heat flux measurements were captured along the wall of the periphery due to the increases gas void fraction until reaching the annulus. The lower average particle residence time in the fountain (Börner et al., 2011) and the lower bulk solid fractions (Brown and Lattimer, 2012) can explain for the slower transient rate of q''_{bw} in the fountain as compared to the annulus. The overall transient wall heat flux analysis of Figure 10 suggests the main source of bed-to-wall heat

transfer outside of the inlet spout channel to be through the convective downward transport of the particles.

6.2 Flow Regimes

The rate energy into the bed, $\dot{E}_{in} = \dot{m}_g c_{p,g} T_{in}$, varies between the spouting, fluidized, and fixed bed regimes. In order to compare the heat flux distributions between these systems, each instantaneous heat flux data set was individually normalized with respect to itself. A generalized bed heat flux distribution was then made by averaging the normalized profiles over a 60 second time span. The resulting mean normalized bed-to-wall heat flux is defined as, $q''_{bw,nom}$. Three vertically distributed wall regions, provided in Figure 11, were then examined. Region I covers axial center, Region II covers the mid-section, and Region III is defined at the outer-walls of the bed.

6.2.1 Single Jet

The $q''_{bw,nom}$ distribution in each of the three regimes is shown in Figure 12 for a single jet. The highest heat flux for each exists in Region I at the jet inlet. For the larger glass particles a greater heat flux can be seen in Region II. This is attributed to the increased spouting diameter produced by the larger diameter particles (Brown and Lattimer, 2012). At a further vertical distance to the annulus, a peak in the heat flux is clearly seen in the spouted bed, in Figure 12a, from the downward convective scoring transport of the particles. A second peak is then observed in the center region for the 550 μm particles at the fountain. A comparable peak is also found at an added height for the 750 μm particles. However this peak is more uniformly distributed over the width of the bed and results from two characteristics of the spouting dynamics. The first is the lack of in-bed stabilizers which lead to spout swaying effects (He et al., 1994). The second reason is due to the increased width of the fountain core and periphery (Brown and Lattimer, 2012). Above the fountain a relatively small $q''_{bw,nom}$ value remains from the convective gas heating in the freeboard.

A similar trend is also seen in the fluidized bed $q''_{bw,nom}$ distribution in Figure 12b. However, the wall heat flux above the internal spouting cavity is more uniform across the three regions. A slight increase in $q''_{bw,nom}$ is again observed in the wall region, Region III, where downward flowing particles entrain into the jet. The fixed bed or internal cavity, represented in Figure 12c also has a similar inlet heat flux map. The only difference is a larger heat flux is

observed in Regions II and III due to the increased internal spouting cavity diameter of the 750 μm particulates (Brown and Lattimer, 2012).

6.2.2 Double Jets

Implementing a second jet into the system provides an altered bed-to-wall heat flux map, shown in Figure 13. The two outer jets produced a highest heat flux in the mid-region, Region II, near the distributor plate. At a further height in the spouting regime, Figure 13a, jet merging in the center region, Region I, is captured. The dynamic sequence between spouting, particulate build-ups, and the eruption of solid particle clusters formed a mixture between a spouting and fluidized bed due to the merging of the two jets (Brown and Lattimer, 2012). A resulting near uniform heat flux is observed at the front wall due the highly turbulent fluidized nature of the bed. A small area of downward entraining particles remained near the outer wall, Region III, shown the $q''_{bw,nom}$ map of Figure 13a.

Lowering the inlet gas velocities to $1.6 u_{mf}$ caused the double jet system to transition into the fluidized regime, seen in Figure 13b. The dead zone build-ups between the jets prevented the internal jet cavities from merging (Brown and Lattimer, 2012). Instead, the shedding bubbles of each jet merged into a larger bubble at the center of the bed, Region I. This bubble continued to rise through the particles before causing the surface of the bed to collapse while new bubbles were being formed. As a result, an increased $q''_{bw,nom}$ concentration was formed in Region I. A similar trend is seen in the fixed bed, shown in Figure 13c, but no sign of jet or bubble merging was present.

7. Conclusion

A non-intrusive bed-to-wall heat transfer technique was developed to capture localized heat flux and wall temperature distributions adjacent to a multiphase flow. The use of a lumped capacitance model and infrared camera allowed for transient experimental tests to be performed where the bed temperature was not limited by the outer wall temperature. Attention was paid to the data processing methods to improve the thermal image signal to noise ratio for evaluating the Laplacian. Experiments were performed to quantify the effects of lateral conduction and the added paint layer. It was concluded that neglecting the paint layer can lead to significant errors in inverse heat conduction problems, mainly through the stored energy term.

The capability of this method was applied to a pseudo 2-D bed to investigate bed-to-wall heat transfer characteristics under spouting, fluidized, and fixed bed regimes. Particle size and the number of jets implicated into the system were varied. The dominant source of heat transfer found at the wall was through the convective impinging action of the inlet gas and the downward transport of the solid particulates. Enlarged spout thermal-gradients were also captured at the inlet for increased particle diameter.

The analysis exposed the interaction of multiple jets and bubble formations through the wall heat flux measurements. Heat transfer data was also captured at the parabolic fountain, showing the core region to contain the highest heat temporal gradients. This experimental study has shown the potential for applying inverse heat transfer analysis to fluidized beds for the validation of computational models.

Acknowledgements

The authors are grateful for the support from the Virginia Tech Institute for Critical Technology and Applied Science (ICTAS).

References

- Bellman, R., Kalaba, R.E., 1965. Quasilinearization and nonlinear boundary-value problems. American Elsevier Pub. Co., New York.
- Bilbao, J., Olazar, M., Arandes, J.M., Romero, A., 1989. Optimization of the Operation in a Reactor with Continuous Catalyst Circulation in the Gaseous Benzyl Alcohol Polymerization. *Chemical engineering communications* 75, 121-134.
- Börner, M., Peglow, M., Tsotsas, E., 2011. Particle Residence Times in Fluidized Bed Granulation Equipments. *Chemical Engineering & Technology* 34, 1116-1122.
- Brown, S., Lattimer, B., 2012. Experimental hydrodynamics of multiple jet systems in a fluidized and spouted bed. (Manuscript submitted for publication). *Int. J. Multiph. Flow*.
- Carlomagno, G.M., Cardone, G., 2010. Infrared thermography for convective heat transfer measurements. *Experiments in Fluids* 49, 1187-1218.
- Chatterjee, A., Adusumilli, R.S.S., Deshmukh, A.V., 1983. Wall-to-Bed Heat-Transfer Characteristics of Spout-Fluid Beds. *Can J Chem Eng* 61, 390-397.

- Churchill, S.W., Chu, H.H.S., 1975. Correlating Equations for Laminar and Turbulent Free Convection from a Vertical Plate. *International Journal of Heat and Mass Transfer* 18, 1323-1329.
- Colombo, L.P.M., Briola, C.L., Niro, A., 2008. Infrared Thermographic Measurements of Heat Transfer Enhancement Over Ribbed Surfaces, *European Thermal-Sciences Conference*, The Netherlands.
- Epstein, N., Mathur, K.B., 1971. Heat and mass transfer in spouted beds - A review. *The Canadian Journal of Chemical Engineering* 49, 467-476.
- Fayed, M.E., Otten, L., 1997. *Handbook of Powder Science and Technology* (2nd Edition). Springer - Verlag, pp. 532-567.
- Gardon, R., 1960. A Transducer for the Measurement of Heat-Flow Rate. *Journal of Heat Transfer* 82, 396-398.
- Gloski, D., Glicksman, L., Decker, N., 1984. Thermal-Resistance at a Surface in Contact with Fluidized-Bed Particles. *International Journal of Heat and Mass Transfer* 27, 599-610.
- Gosmeyer, C.D., 1979. An experimental study on heat transfer in large particle heated fluidized bed. Oregon Univeristy, Corvallis, Oregon, U.S.A.
- He, Y.L., Lim, C.J., Grace, J.R., Zhu, J.X., Qin, S.Z., 1994. Measurements of Voidage Profiles in Spouted Beds. *Can J Chem Eng* 72, 229-234.
- Ilyinsky, A.L., Rainieri, S., Farina, A., Pagliarini, G., 1997. New Experimental Technique for Enhancement of Spatial Resolution in Heat Transfer Measurements, *Proc. 4th World Conference on Experimental Heat Transfer, Fluid Mechanics and Thermodynamics*, Brussels, pp. 93 - 100.
- Incropera, F.P., DeWitt, D.P., 2002. *Fundamentals of heat and mass transfer*. J. Wiley, New York.
- Klassen, J., Gishler, P.E., 1958. Heat transfer from column wall to bed in spouted fluidized and packed systems. *The Canadian Journal of Chemical Engineering* 36, 12-18.
- Kmieć, A., 1980. *Hydrodynamics of Flows and Heat Transfer in Spouted Beds*. The Chemical Engineering Journal 19, 189-200.
- Kuiken, H.K., 1969. General series solution for free convection past a non-isothermal vertical flat plate. *Applied Scientific Research* 20, 205-215.
- Kunii, D., Levenspiel, O., 1991. *Fluidization engineering*. Butterworth-Heinemann, Boston.

- Malek, M.A., Lu, B.C.Y., 1964. Heat transfer in spouted beds. *The Canadian Journal of Chemical Engineering* 42, 14-20.
- Mehryar, R.G.A.C.S., 2006. Paint effects on the advanced quantitative infrared thermography applied to jet impacts, 8th Conf. on QIRT, Padova, Italy.
- Moffat, R.J., 1988. Describing the uncertainties in experimental results. *Experimental Thermal and Fluid Science* 1, 3-17.
- Na, T., 1977. Numerical solution of natural convection flow past a non-isothermal vertical flat plate. *Applied Scientific Research* 33, 519-543.
- Nogueira, E.S., Pereira, J.R.D., Baesso, M.L., Bento, A.C., 2003. Study of layered and defective amorphous solids by means of thermal wave method. *Journal of Non-Crystalline Solids* 318, 314-321.
- Patil, V.A., Narayanan, V., 2005. Application of heated-thin-foil thermography technique to external convective microscale flows. *Meas. Sci. Technol.* 16, 472-476.
- Petrovic, L.J., Thodos, G., 1968. Effectiveness factors for heat transfer in fluidized beds. *The Canadian Journal of Chemical Engineering* 46, 114-118.
- Pons, M., Dantzer, P., Guillemot, J.J., 1993. A Measurement Technique and a New Model for the Wall Heat-Transfer Coefficient of a Packed-Bed of (Reactive) Powder without Gas-Flow. *International Journal of Heat and Mass Transfer* 36, 2635-2646.
- Raghu, O., Philip, J., 2006. Thermal properties of paint coatings on different backings using a scanning photo acoustic technique. *Meas. Sci. Technol.* 17, 2945-2949.
- Rainieri, S., Bozzoli, F., Pagliarini, G., 2008. Characterization of an uncooled infrared thermographic system suitable for the solution of the 2-D inverse heat conduction problem. *Experimental Thermal and Fluid Science* 32, 1492-1498.
- Rainieri, S., Pagliarini, G., 2002. Data filtering applied to infrared thermographic measurements intended for the estimation of local heat transfer coefficient. *Experimental Thermal and Fluid Science* 26, 109-114.
- Saxena, S.C., Srivastava, K.K., Vadivel, R., 1989. Experimental-Techniques for the Measurement of Radiative and Total Heat-Transfer in Gas-Fluidized Beds - a Review. *Experimental Thermal and Fluid Science* 2, 350-364.
- Stafford, J., Walsh, E., Egan, V., 2009. Characterizing convective heat transfer using infrared thermography and the heated-thin-foil technique. *Meas. Sci. Technol.* 20.

Tsuji, T., Uemaki, O., 1994. Coal-Gasification in a Jet-Spouted Bed. *Can J Chem Eng* 72, 504-510.

Werther, J., 1999. Measurement techniques in fluidized beds. *Powder Technol.* 102, 15-36.

Yusuf, R., Halvorsen, B., Melaen, M.C., 2012. An experimental and computational study of wall to bed heat transfer in a bubbling gas–solid fluidized bed. *Int. J. Multiph. Flow* 42, 9-23.

Figures and Tables

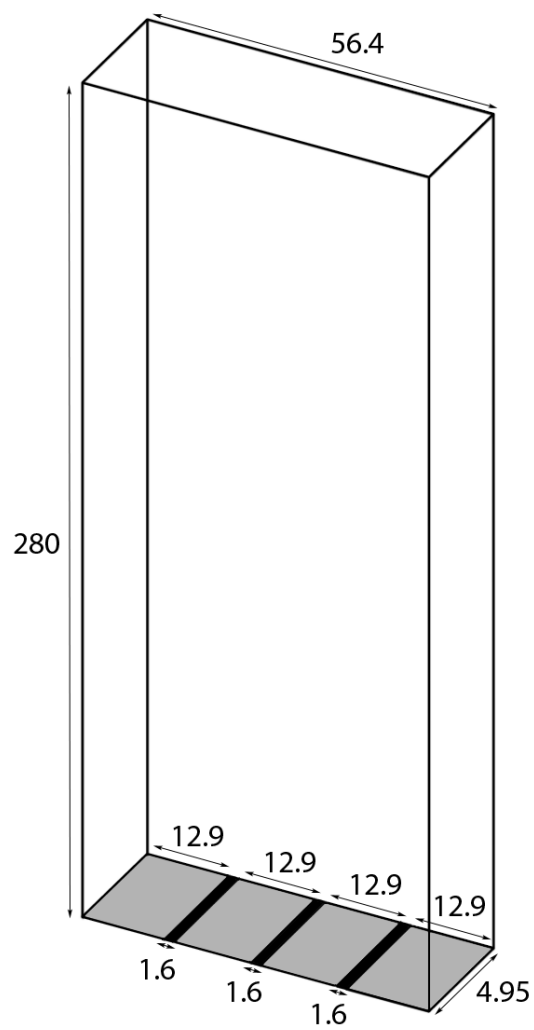


Figure 1: Schematic of the 2-D flat bottom rectangular column setup with dimensions in mm.

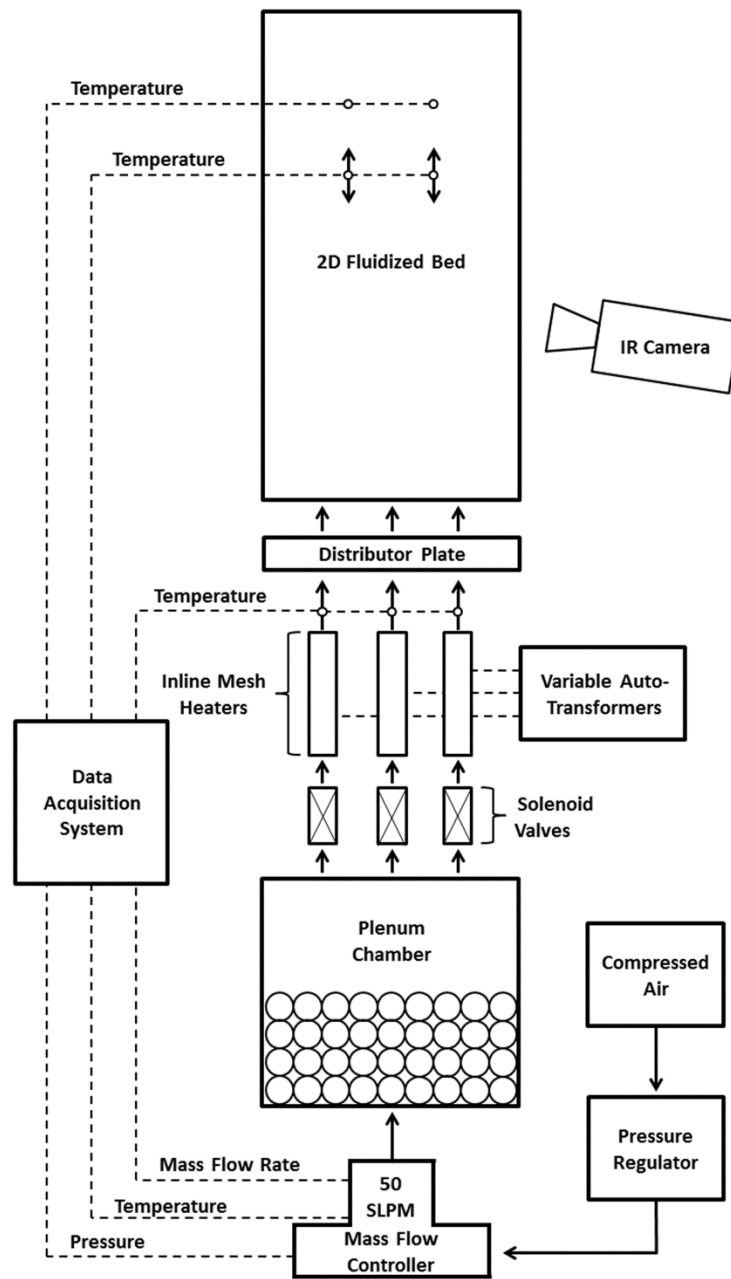


Figure 2: Diagram of the experimental setup.

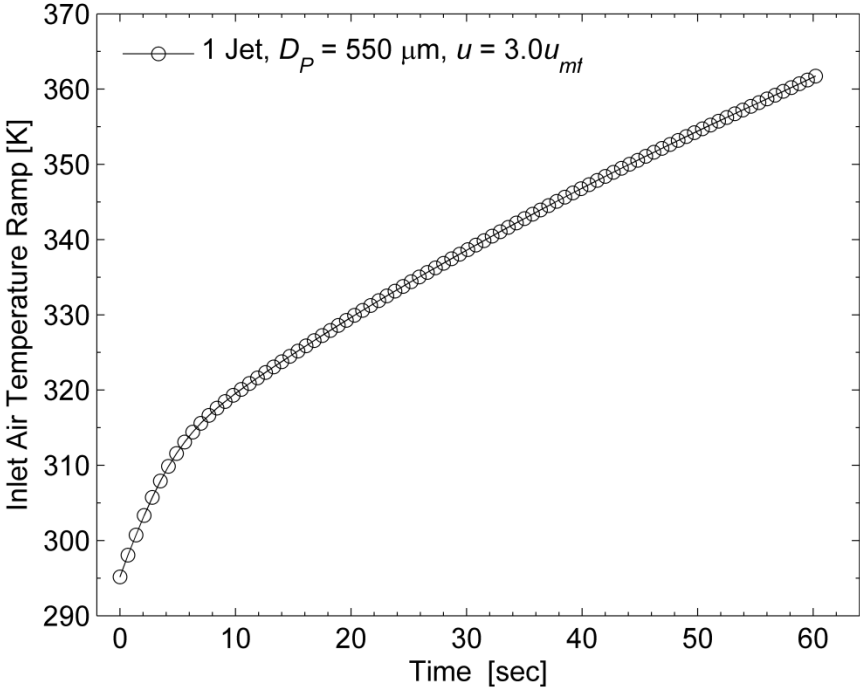


Figure 3: Transient inlet air temperature ramp at $3 u_{mf}$ for a single jet with glass particles of $D_p = 550 \mu\text{m}$

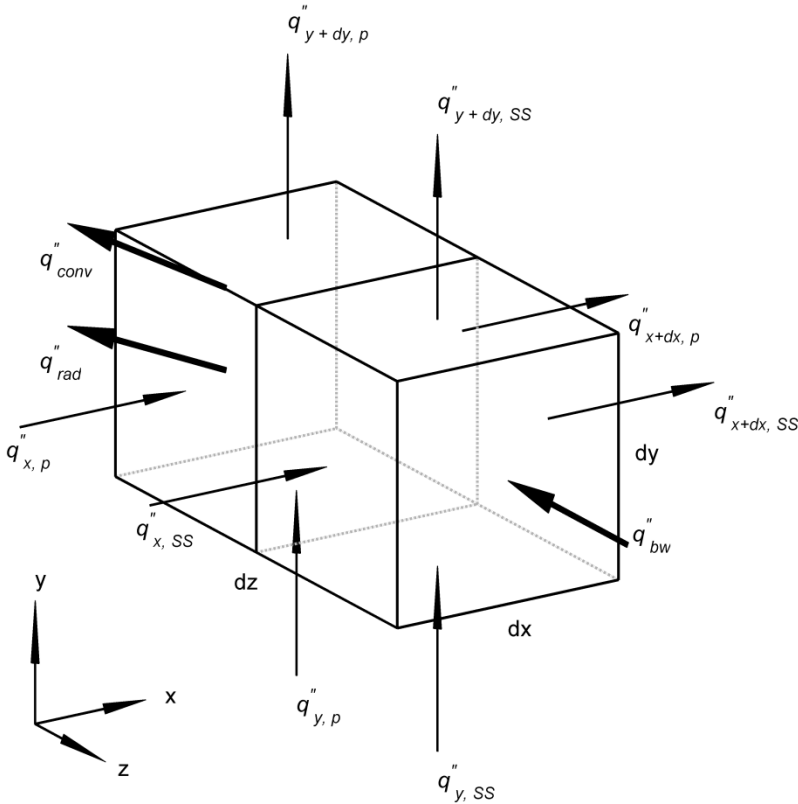
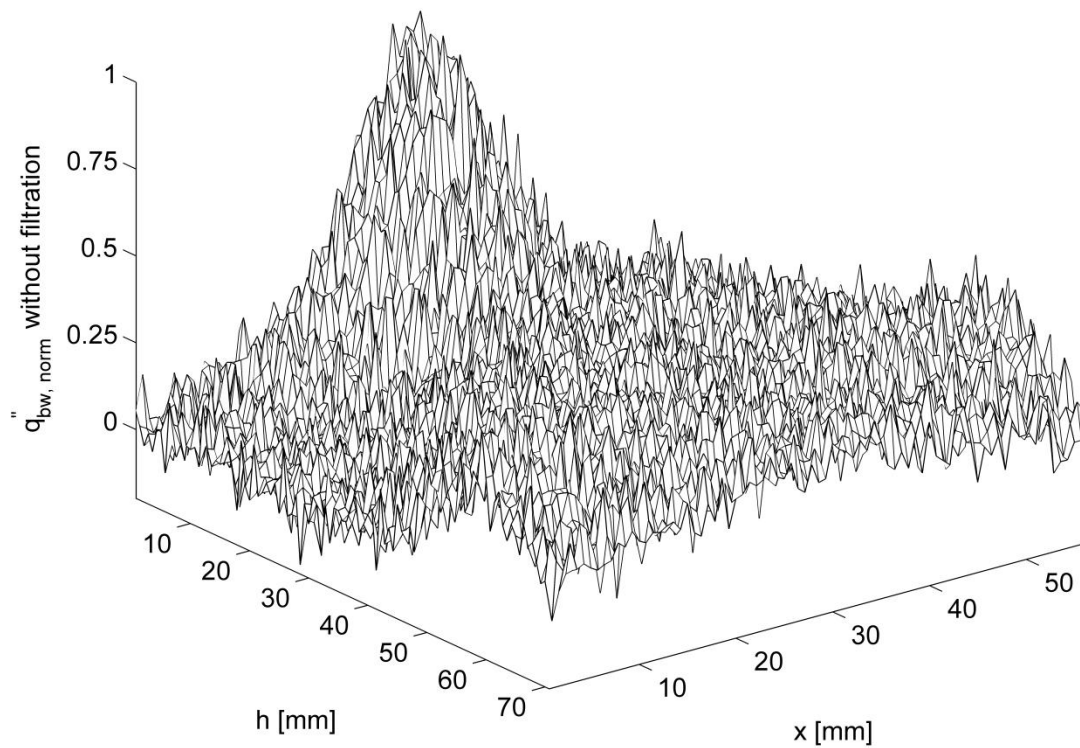


Figure 4: Differential control volume for the paint layer and stainless steel plate.

a)



b)

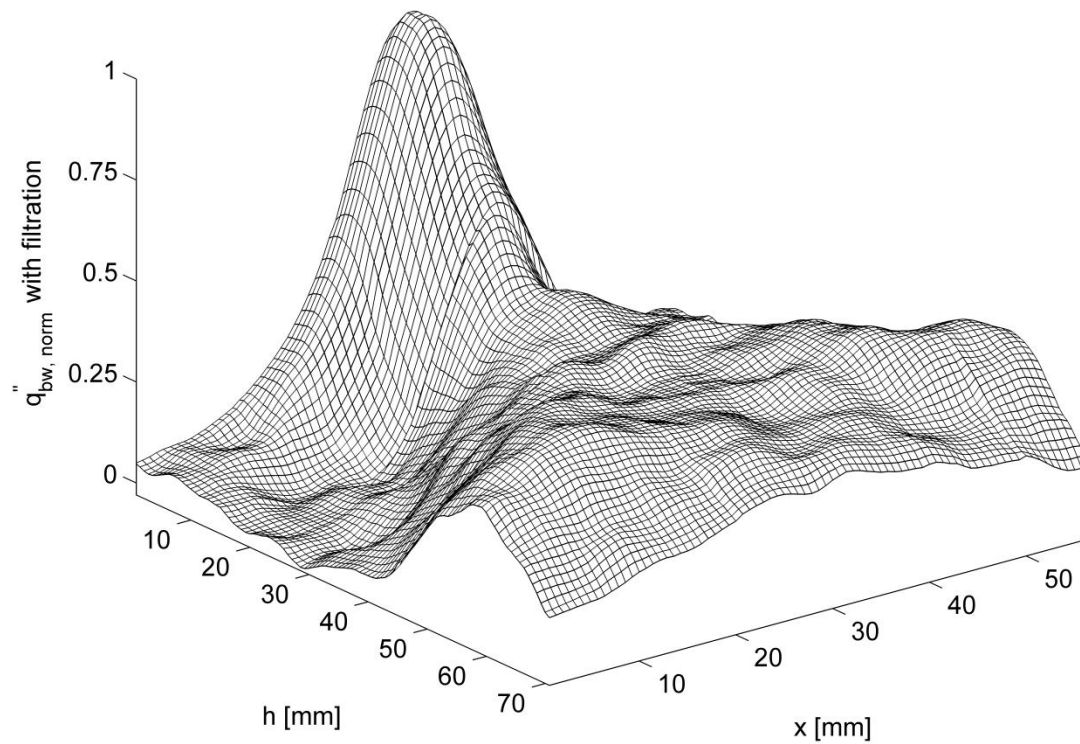


Figure 5: Normalized bed-to-wall heat flux data a) without filtration and b) with filtration for a single jet fluidized bed.

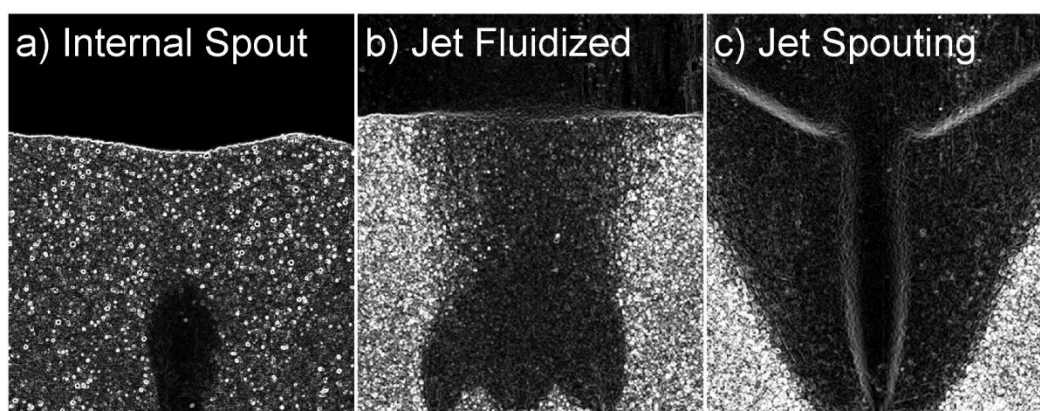


Figure 6: Mean Prewitt high pass filtered PIV images illustrating an a) internal spout, b) multiple jet fluidized bed, and c) a single jet spouting bed.

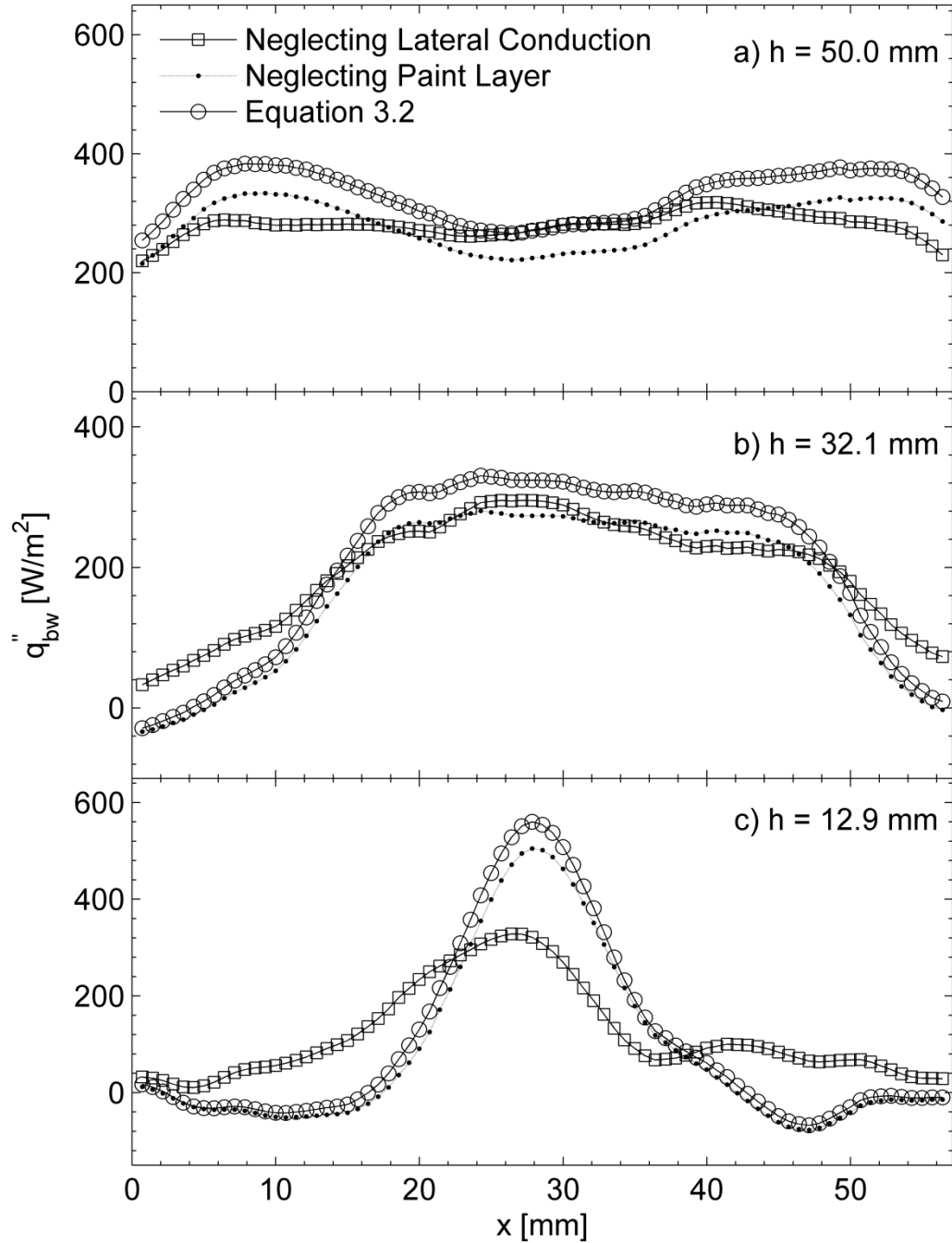


Figure 7: Effects of neglecting lateral conduction and the paint layer on Equation 3.2 in a single jet, G550, fluidized bed at $1.6 u_{mf}$ and $t = 19$ seconds.

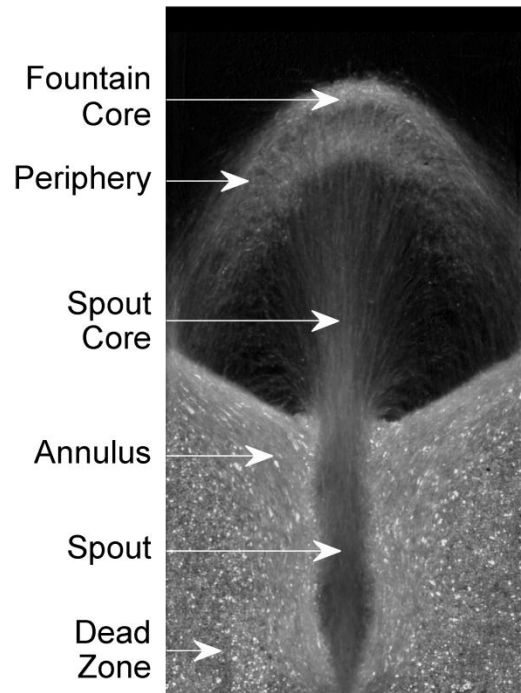


Figure 8: Instantaneous PIV image illustrating the various regions in a spouted bed.

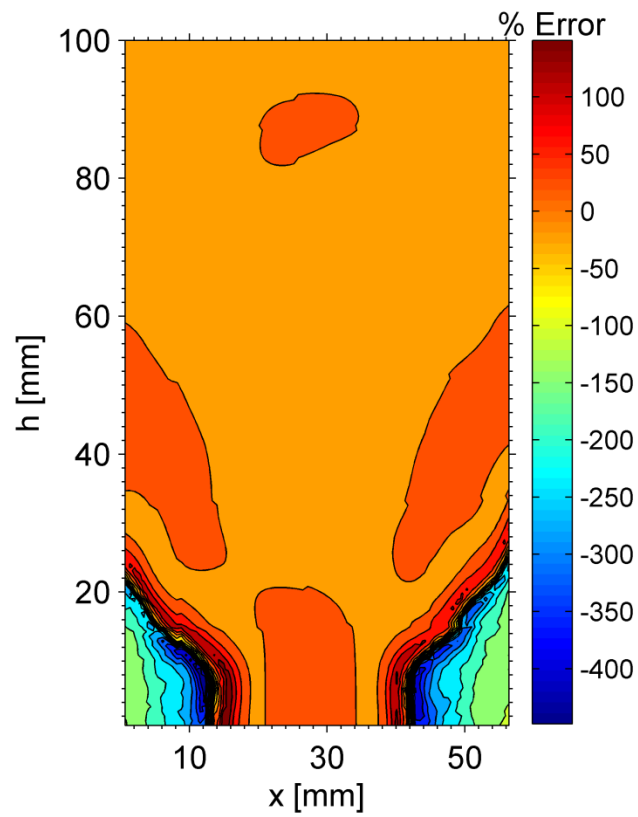


Figure 9: Mean error in neglecting lateral conduction over a 60 second time span in a single jet, G550, spouted bed at $3 u_{mf}$.

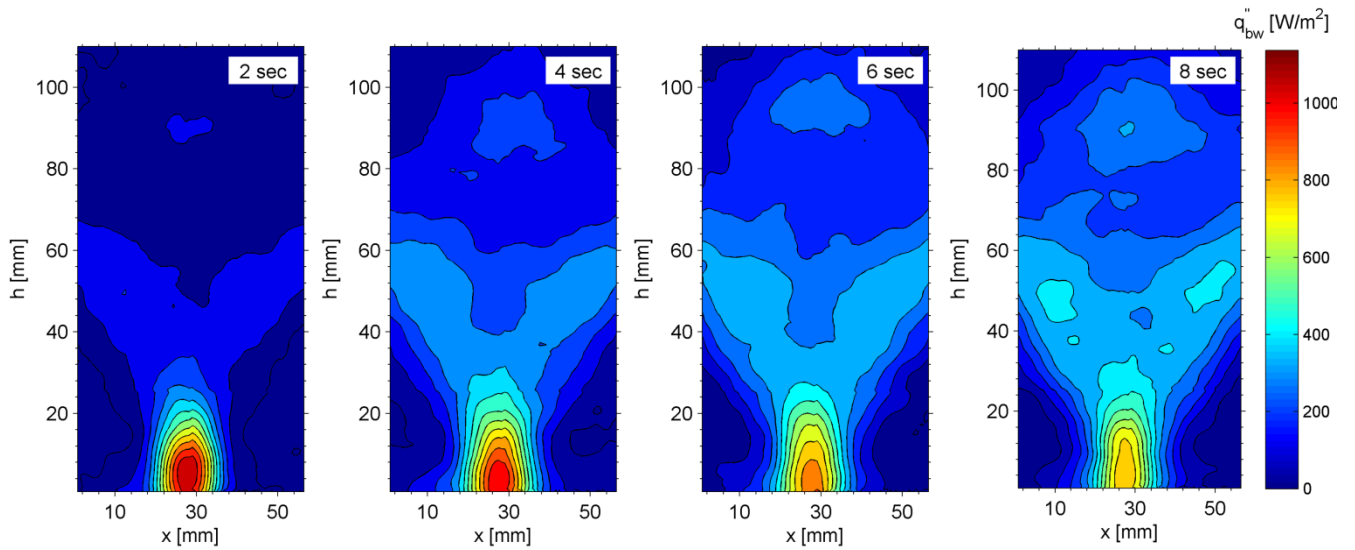


Figure 10: Transient time series bed-to-wall heat flux distributions of a single jet, G550, spouted bed at $3 u_{mf}$.

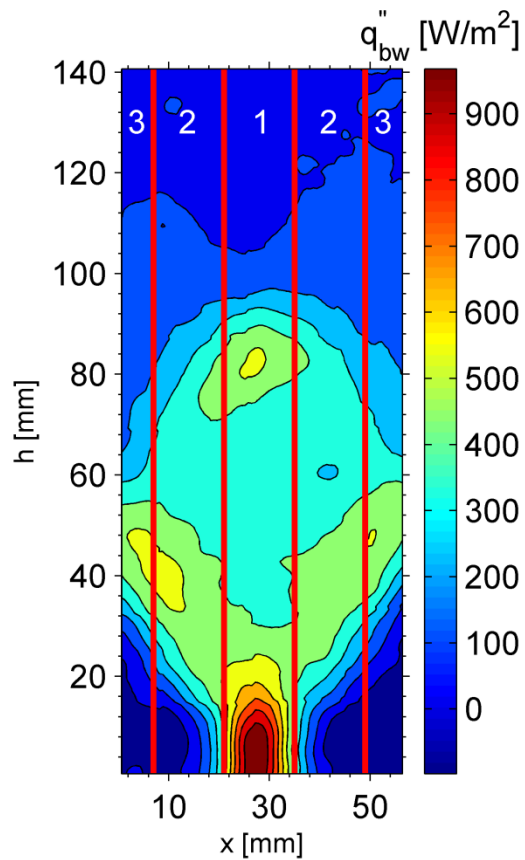


Figure 11: Heat Flux interrogation areas: center (1), mid (2), and outer-wall (3) regions.

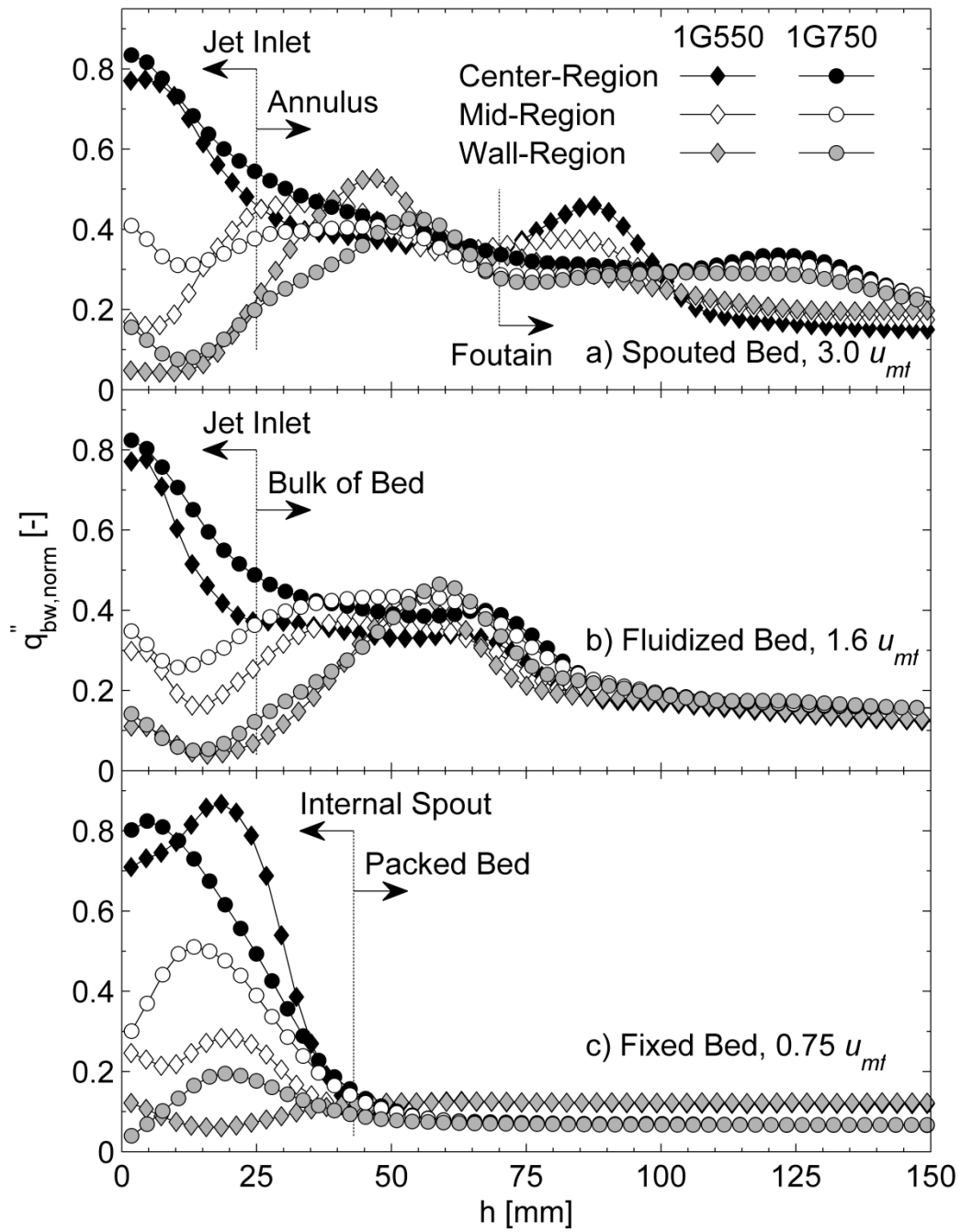


Figure 12: Normalized bed-to-wall heat flux distributions for a single jet system over 60 seconds.

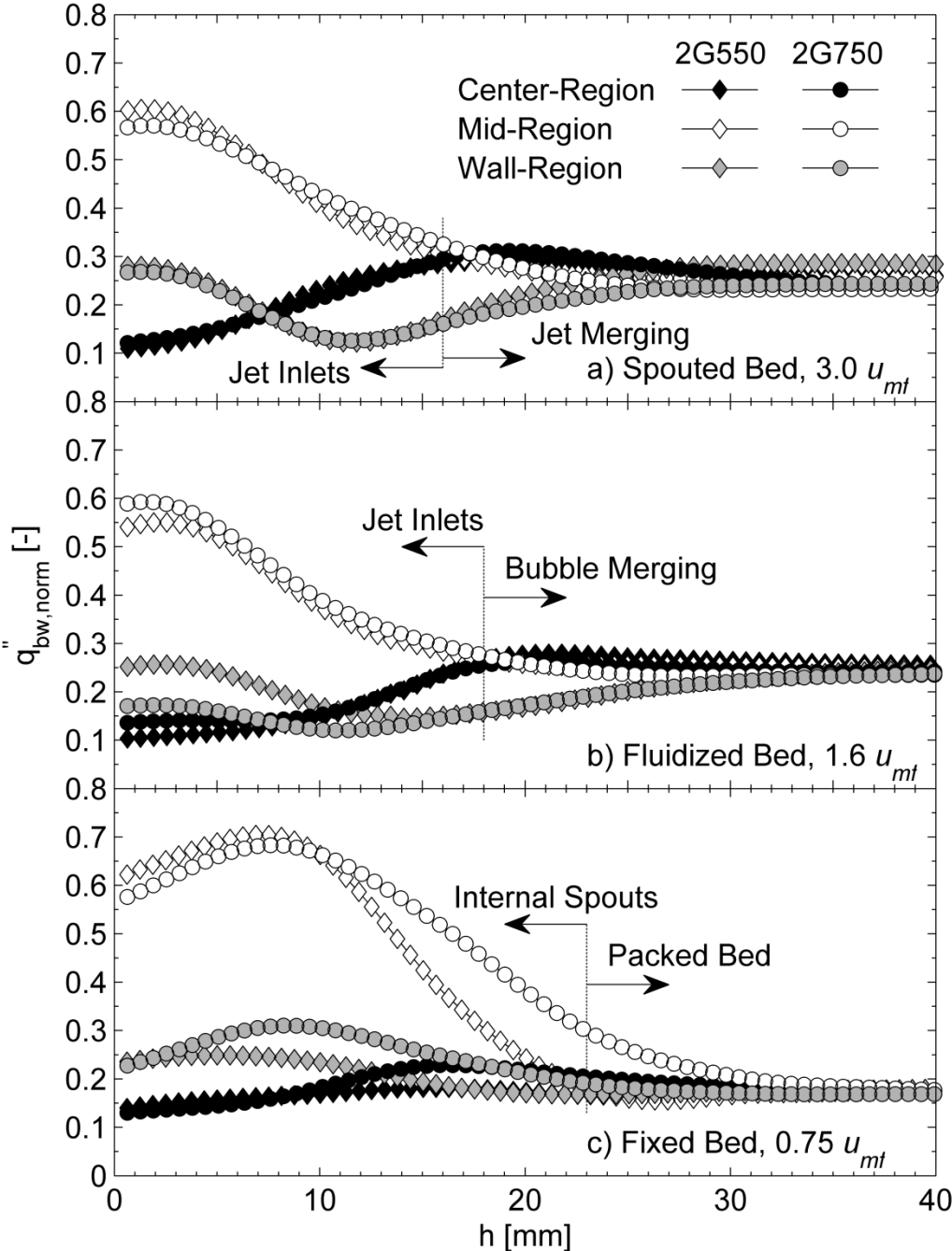


Figure 13: Normalized bed-to-wall heat flux distributions for a double jet system over 60 seconds.

Table 1: Material properties.

Property	SS 304	Paint	Units
Density	8000	1331	kg m^{-3}
Thermal Conductivity	16.2	1.38	$\text{W m}^{-1}\text{K}^{-1}$
Thickness	152	20	μm
Specific Heat	500	5184	$\text{J kg}^{-1}\text{K}^{-1}$

Table 2: Properties of experimental fluidized bed media.

Property	Small Particles	Large Particles
Notation	G550	G750
Geldart Group	B	D
Number of Particles	100,000	50,000
D_p [μm]	550	750
ρ_p [kg m^{-3}]	2500	2500
ϕ_s [-]	1	1
u_{mf} [m s^{-1}]	0.24	0.43

Table 3: Instrument resolution and material uncertainties.

p_i	dp_i	Units
$c_{p,p}$	± 518	$\text{J kg}^{-1}\text{K}^{-1}$
ε	± 0.02	-
k_p	± 0.11	$\text{W m}^{-1}\text{K}^{-1}$
δ_p	± 2.0	μm
δ_{ss}	± 7.6	μm
ρ_p	± 39	kg m^{-3}
T_{ref}	± 0.1	K
$T_{x,y}$	± 0.2	K

Chapter 4

Transient Gas-to-Particle Heat Transfer Measurements in Fluidized and Spouted Beds

Abstract

Heat transfer characteristics of fluidized particles were experimentally quantified through measuring emitted infrared radiation. The presented experimental technique was designed to overcome the spatial, time varying, and instrumental intrusive limitations often found in multiphase flow studies. A pseudo two-dimensional bed was investigated by supplying a thermo-transient inlet gas temperature to fluidized, spouted, and fixed bed regimes. The highest rates of energy stored in the particles were found along the downward particulate entrainment zones surrounding the inlet gas channel. Gas-to-particle heat transfer coefficients in the spouted regime were computed per bed axial position. The resulting values found in the lower portion of the spout were in close comparison to the averaged gas-to-particle heat transfer coefficient empirical correlations found in literature. New findings are given on the high convective heat transfer coefficients in the spout fountain region, resulting from the highly turbulent nature of gas-solid mixing.

Submitted for review to the Experimental Thermal and Fluid Science Journal, June 2012

Corresponding Author: Steven L. Brown

Co-Author: Brian Y. Lattimer

1. Introduction

Fluidization is commonly used in industrial applications for its intense mixing capabilities and high rates of heat exchange in multiphase flow. The large surface area of fluidized particulates allows for near isothermal operating conditions between gas and solids. Scaling-up laboratory sized beds to industry sized applications has remained a challenge. To address this issue, Computational Fluid Dynamic (CFD) models are being developed to predict the characteristics of fluidized systems. The current advancements in CFD models demand validation with quantifiable, accurate, and detailed experiments.

Fluidized, spouted, and fixed beds have different gas-solid dynamics and thus yield varied heat transfer characteristics. The successful designs of these fluidized systems rely on the characterization of the various flow regimes. Temperature distribution is an important parameter to classify. Heat transfer information exists in literature, but is scarce at the detailed particle level need for CFD validation, such as Discrete Particle Models (DPM).

Past experimental studies have typically neglected intra-particle temperature gradients by assuming equal gas and particle temperature through a steady state analysis. This type of approach most often leads to an overall averaged bed heat transfer coefficient. By measuring the bulk properties of the bed, the spatial resolution of gas and particle heat transfer characteristics is lost.

To remain non-intrusive to the gas-solid flow, Kmiec (1975) and Englart et al. (2009) have applied a water vapor analysis to cylindrical spouted beds containing conical bases. An overall heat transfer coefficient was quantified through the use of a log mean temperature difference across the steady-state spouted bed. As a result both studies resulted in empirical correlations to predict gas-to-particle heat transfer coefficients. These studies provide detailed information, but are limited to an average gas-to-particle heat transfer coefficient across the bed.

To increase spatial variation of heat transfer measurements, thermocouples are commonly placed inside the gas-solid flow. The difficulties associated with measuring relative solid and gas temperatures with thermocouples was reviewed by Baeyens and Goossens (1973). Intrusive thermocouples are anticipated to have convective and conductive heat transfer with the surrounding gas and solid flow. Yet, the use of in bed thermocouples is frequently found throughout literature. Malek and Lu (1964) applied bare bed thermocouples to measure air

temperature, and mesh covered thermocouples to measure the temperature difference somewhere between the gas and solids in a spouted bed. Petrovic and Thodos (1968) has also used a similar technique in a fluidized bed by imbedding a thermocouple within a sphere to compute particle surface temperature. The intrusive effects of thermocouples on the hydrodynamics were noted by Malek and Lu (1964) as it caused the spout to sway and decrease in height in their study. In addition, the resolution of the measurement technique was limited to the discrete number of thermocouples applied in the analysis.

Numerical models have also been developed to help quantify the heat transfer characteristics. Kmiec (1980) defined a two zone thermal-model based on a spouted bed. The analysis only focused on the spout and annulus zones, while neglecting the fountain region. In a small scale laboratory bed the fountain region can consist of a significant amount of particulates (Brown and Lattimer, 2012a). In addition, the high gas-solid turbulence mixing found in a fountain is substantial to consider in convective heat transfer analysis. The knowledge of the particle temperature is also desirable when computing near wall particle conductivity of the bulk regions for CFD simulations (Yusuf et al., 2012). A recent experimental study by Hamzehei and Rahimzadeh (2009) was designed to validate a CFD heat transfer model of a fluidized bed. In their study, the CFD thermal-model was validated through gas temperature variations as particle temperature measurements were not available from the experimental study.

The aim of this study is to apply an innovative, but yet simple approach to measuring particle temperature. An experimental pseudo two-dimensional bed was designed with a container wall made from an optical window having high transmission in the infrared radiation wavelength spectrum. As a result, the electromagnetic radiation of the fluidized particles can be directly measured to compute near wall particle temperatures. The advantage of this approach is the measurement is non-intrusive to the gas-solid flow. In addition, the method is not limited to steady-state conditions. Moreover, the detailed localized data needed for the validation of DPM can be captured with respect to time. This study extends upon the hydrodynamics of a multiple jet system previously characterized by Brown and Lattimer (2012a).

A description of the non-reacting bed setup and detailed explanation of the measurement technique is first given. This is followed by an experimental investigation of a thermo-transient single jet spouted, fluidized, and fixed bed study. The hydrodynamics of the gas-solid mixing system is examined under steady-state conditions, while the inlet gas temperature is subjected to

a thermo-transient response. The heated inlet gas then flows into the ambient temperature particle bed to provide the time dependent heat transfer analysis.

2. Experimental Setup

The experiments were performed in a pseudo two-dimensional fluidized bed, shown in Figure 1, with cross-section dimensions of $W = 56.4$ mm, $D_b = 4.95$ mm and overall bed height, H , of 280 mm. The base entailed of a stainless steel distributor plate with three evenly selectable slit jets of 1.6 mm wide by the full depth of the bed. The outside of the plate was coated with a low thermal conductivity silicon rubber insulation to reduce thermal energy loss. The back and side walls consisted of Polymethyl-Methacrylate coated in paint to ensure surface flatness. The front wall comprised of a 12.7 mm thick sodium chloride, NaCl, window. This window exhibits high transmission in the near infrared (0.75 – 3 μm), middle infrared (3 – 6 μm), and far infrared (6 – 15 μm) wavelength bands, with good transmission in the visible light spectrum.

A schematic of the setup is given in Figure 2. Compressed air was used as the fluidization gas and was controlled by a pressure regulator and a 50 SLPM ALICAT (Model # MC-50SLPM-D) mass flow controller with an accuracy of ($\pm 0.4\%$ reading, + 0.25% FS). The gas was first channeled through a plenum chamber and controlled by three rapidly responding solenoid valves providing the ability for various jet selections. The gas was then directed through inline mesh heaters each controlled by a variable autotransformer with a maximum capacity of 2.0 kVA.

Chromel-Alumel (Type K) bare bead thermocouples were located near the top of the distributor plate just below the gas inlet of each slot jet to measure in inlet gas temperature, $T_{g,in}$ (K). Two thermocouples were positioned at a height of 174 mm upstream of the distributor plate in the freeboard region, while two additional thermocouples, $T_{g,out}$ (K), were also placed just above the maximum expanded bed height of each experimental test case. A 32 bit National Instrument cDAQ-9174 chassis was used with a NI-9123 card to record the thermocouple data at 10 Hz under a high-resolution mode providing a measurement sensitivity less than 0.02 $^{\circ}\text{C}$.

A FLIR SC655 Infrared (IR) camera, operating in the 7.5 - 13.0 μm range, was directly placed perpendicular to the sodium chloride window of the bed to capture local particle temperature distributions. The area surrounding the fluidized bed was enclosed in a black body box with an opening for the IR camera lens to prevent external radiation reflections. The

sampling frequency of the IR camera was set at 200 Hz while the 24.5 mm lens provided a resolution, $M_{px} \times N_{px}$, of 640 x 120 pixels or about 1 pixel per particle.

The top of the distributor plate was covered by a fine mesh screen and the bed was filled with glass particles. The particles pertained to the Geldart B classification with mean diameter, D_p , of 550 μm . The minimum fluidization velocity, u_{mf} (m s^{-1}), was previously found by Brown and Lattimer (2012a) through applying a differential pressure drop analysis and is given in Table 1 along with the physical properties of the particles.

3. Data Acquisition

Knowledge of the basic principles of radiation is needed to understand infrared thermography, calibration techniques, and the experimental measurement procedure. Each is discussed in this section.

3.1 Infrared Measurements

Instantaneous particle temperatures were computed by measuring thermal radiation through infrared thermography. Radiation is emitted by any matter with at a nonzero temperature. The body with the greatest emissive power at a given temperature is known as an ideal radiator or a blackbody. The spectral intensity of a black body, $I_{\lambda,b}$ (Wm^{-3}), can be determined by Planck's law of radiation,

$$I_{\lambda,b} = \lambda^5 C_1^{-1} [\exp(C_2/\lambda T) - 1] \quad (3.1)$$

where the first and second radiation constants are $C_1 = 3.742 \times 10^{-16}$ (Wm^{-2}), $C_2 = 1.439 \times 10^{-2}$ (Wm^{-2}), λ (m) is the radiation wavelength, and T (K) is the absolute temperature of the blackbody. However, the particles examined are not a blackbody and therefore emit only a fraction of the total radiation exhibited by a blackbody, I_λ (Wm^{-3}). The energy emitted relative to a black body is expressed as the dimensionless emissivity coefficient, defined as:

$$\varepsilon_\lambda = I_\lambda / I_{\lambda,b} \quad (3.2)$$

In addition to the particle emissivity, the transmission factor, τ_λ , of the sodium chloride window will also limit the amount of electromagnetic radiation received by the IR Camera. Accounting for the above parameters, the incident spectral irradiance captured by the IR camera is defined in terms of Equation 3.1 as:

$$I_\lambda = \tau_\lambda \varepsilon_\lambda \lambda^5 C_1^{-1} [\exp(C_2/\lambda T) - 1] \quad (3.3)$$

Both the emissivity and transmission of a material can be directly measured. However, both parameters vary with wavelength and partially with temperature. Therefore, it is necessary to perform a calibration based on the experimental parameters instead of using manufacturer defined values.

3.2 Emissivity and Transmission Calibration

A calibration apparatus was designed by attaching a film heater to a copper plate coated in paint close to the ideal blackbody with low radiation reflection. Near uniform heating was achieved through the high thermal conductivity of the plate. The painted plate was covered with glass particles and multiple bare bead thermocouples were immersed in the particles. The sodium chloride window was positioned just above the particles. Natural convective heat loss and external radiation was reduced by encompassing the setup in a black body box with an opening for the IR camera. The camera was positioned the same distance from the NaCl window as used in the experiments. First, the temperature of the particles were varied and then allowed to reach near isothermal conditions. The differences between the thermocouples and digital level of the IR camera readings were used to produce the calibration curve show shown in Figure 3. Confidence in the resulting calibration curve was found as the curve was in close comparison to a theoretical calibration defined from using the manufactures values for the NaCl transmission and particle emissivity.

3.3 Measurement Procedure

The experimental procedure started by first fluidizing the particles with ambient temperature air at over $3 u_{mf}$ and then incrementally dropping the superficial gas velocity. Once the desired inlet gas flowrate was reached, a period of five minutes was allowed for the gas-solid hydrodynamics to reach steady state conditions. Power was then supplied to the inline mesh heaters producing a transient inlet air temperature curve. Figure 4 shows the inlet air temperature ramp for a single jet in a spouted, fluidized, and fixed bed regime. It should be noted from Figure 4 that the rate of change in the inlet gas temperature varied with the magnitude of the inlet gas velocity. The transient heating of the particles were then recorded with the IR camera for a duration of 60 seconds.

4. Data Analysis

By conservation of energy, the rate of energy transferred from the gas to the bed, \dot{E}_{gb} (W), is equal to the rate of energy stored in the particles, \dot{E}_p (W), if there is no energy lost. The inlet gas was assumed as an ideal gas and therefore has constant specific heat, C_p (J kg⁻¹K⁻¹). A resulting thermal energy equation based on the rate of enthalpy flow through the bed is expressed as:

$$\dot{E}_{gb} = \dot{m}_g C_{p,g} (T_{g,in} - T_{g,out}) \quad (4.1)$$

where \dot{m}_g (kg s⁻¹) is the inlet gas flowrate and subscript g denote to the gas. The total change in energy stored in the particle bed due to intra-particle temperature changes is defined as:

$$\dot{E}_p = \sum_{i=1}^{M_{px}} \sum_{j=1}^{N_{px}} \rho_p C_{p,p} V_{px} (1 - \varepsilon_f) \frac{dT_p}{dt} \quad (4.2)$$

where subscript p denotes the particles, ρ (kg m⁻³) is the density, V_{px} (m³) is the volume of a pixel, ε_f is the local gas void fraction, T_p (K) is the measured particle temperature, and t (sec) is time. Typically, past studies have measured particle temperature with in bed thermocouples and gas temperature with mesh-screen covered thermocouples (Freitas and Freire, 2001; Malek and Lu, 1964). However, the aim of this study is to measure bed heat transfer characteristics without being intrusive to the gas-solid flow. Therefore, an equation was derived to compute the mean gas temperature per cross-sectional bed width, T_g (K). The derivation assumes no energy losses, the mass of the gas is negligible to the overall mass of the particles, and that the particles defined in an interrogation area is constant per captured instance (0.005 sec). By conservation of energy and the above defined assumptions, the rate of energy stored in the particles per unit cross-sectional bed height is equal to the enthalpy change in the gas flow per the same change in height. An energy balance based on the gas-to-particle heat transfer, \dot{E}_{gp} (W), was defined by the discrete differential equation:

$$\dot{E}_{gp} = \sum_{i=1}^{M_{px}} \rho_p C_{p,p} V_{px} (1 - \varepsilon_f) \frac{dT_p}{dt} = \dot{m}_g C_{p,g} dT_g \quad (4.3)$$

The equated gas temperature distribution was applied to compute the overall gas-to-particle convective heat transfer coefficient per bed height as:

$$h_{gp} = \frac{\dot{E}_{gp}}{A_{px}(T_g - T_{p,s})} \quad (4.4)$$

Significant heating of the particles in the dead-zones was not observed in the study. Therefore, only the surface area of the non-stagnant particles, A_{px} (m), was used in Equation 4.4. The particle temperature, $T_{p,s}$ (K), was taken as the cross-sectional average and also neglected the temperature of the stagnant particles. The particle surface area per bed height was defined as:

$$A_{px} = \sum_{i=1}^{NS_{px}} \frac{6(1 - \varepsilon_f)\phi_s}{D_p} V_{px} \quad (4.5)$$

where NS_{px} is the number of pixels per row containing non-stagnant particles, and ϕ_s is the shape factor of the solid particulates. The local gas void fraction distribution and the defined dead-zone regions were taken from the Particle Image Velocimetry (PIV) study of Brown and Lattimer (2012a). A resulting gas-to-particle heat transfer coefficient is computed per bed height and unit time. To compare the ratio of the convective heat transfer to the conductive heat transfer coefficient, Equation 4.4 is also expressed in terms of the dimensionless Nusselt number:

$$Nu_p = \frac{h_{gp}D_P}{k_g} \quad (4.6)$$

where k_g ($\text{Wm}^{-1}\text{K}^{-1}$) is the thermal conductivity of the gas.

5. Results and Discussion

The experimental studies investigate the gas and particle heat transfer characteristics in a fluidized ($1.6 u_{mf}$), spouted ($3.0 u_{mf}$), and fixed ($0.7 u_{mf}$) bed. Instantaneous gas void fraction distributions, taken from Brown and Lattimer (2012a), are given for the spouted and fluidized regime, in Figure 5, to illustrate the concentration of gas in the multiphase flow regimes. Transient particle temperature distributions, rates of energy stored in the particles, and gas-to-particle heat transfer coefficient distributions are quantified and discussed in the following sections.

5.1 Transient Temperature Distributions

Time dependent particle temperature distributions are shown in Figures 6-8 for a single jet fixed, fluidized, and spouted bed respectfully. The dead zones are clearly identified in each figure as the low particle temperature regions surrounding the jet inlet. Low gas void fraction

found in the dead zones (Brown and Lattimer, 2012a) directly resulted in minimal convective gas-to-particle heat transfer in these regions. The small internal spout in the fixed bed of Figure 6 shows the highest particle temperature at the top of the spouting cavity. Here the inlet gas directly impinges upon the stationary particles at the top of the cavity. The width of the internal jet expanded with height until reaching a maximum (Agarwal et al., 2011; Brown and Lattimer, 2012a). The increased width and high gas void fraction at the top of the internal spout allowed for an increased turbulent mixing between the particles and gas.

Figure 7 shows the time dependent particle temporal variations in the fluidized regime. The particle entrainment path of the fluidized bed is seen through the temporal maps as the particles move upward above the jet region and entrain downward in the moving zones surrounding the jet zone. The highest particle temperatures were recorded at the top surface of the bed. This was accredited to three main reasons with respect to the thermal-dynamics of the bed and to the measurement technique applied. The first reason is convective gas-to-particle heat transfer was induced at the top of the bed from the highly turbulent bubble eruptions. Secondly, the particles of the shallow bed have a low residence time, τ_p (sec), in the gas channel. As the contact time between the gas and a particle decreases, the intra-particle temperature gradient became significant. The validity of a lumped capacitance model on a single particle can be determined through the Biot number,

$$Bi = 0.5hD_p k_p^{-1} \quad (5.1.1)$$

provided that the Fourier number, Fo ,

$$Fo = 4\alpha_p \tau_p D_p^{-2} \quad (5.1.2)$$

is greater than the minimum value of 0.2 (Incropera and DeWitt, 2002), where k_p ($\text{Wm}^{-1}\text{K}^{-1}$) is the particle thermal conductivity, α_p (m^2s^{-1}) is the thermal diffusivity of the particles, and h ($\text{Wm}^{-2}\text{K}^{-1}$) is the heat transfer coefficient. The resulting high particle surface temperature limits the gas-to-particle heat exchange rate. Lastly, a high bed-to-wall heat flux was reported by Brown and Lattimer (2012b) at the gas inlet. Energy is lost from both the gas and particles to the wall. The IR camera captures particles temperatures closest to the IR window. If energy is being lost at the wall, then higher temperature particles exist in the depth of the bed. With a bed depth of $9 D_p$, the particles in the internal region of the bed are not captured until being entrained near the NaCl wall or into the open freeboard region.

These same effects are captured in Figure 8 for a spouting regime. Here the particle residence time in the spout is less than the fluidized bed. An even lower Fourier number exists and results in further increased intra-particle temperature gradients. The highest particle temperatures are not precisely at the base of the gas inlet but rather at an increased height into the spout channel. A slight decrease in particle temperature is observed with a further increase in bed height. The temperature continues to drop to a local minimum and then again increases until reaching the fountain core.

The particles entrain from the fountain periphery to the top of the annulus, shown in the timeline temperature distribution of Figure 8. Only a small fraction of the gas entrains downward with the particles into the annulus (Brown and Lattimer, 2012a). A near uniform temperature distribution is seen in the annulus with decreasing bed height. The high particle residence time in the annulus allows for near uniformity between the temperature of the gas and the particulates. The observed heat transfer characteristics in the three main divided regions between the spout channel, fountain, and annulus are important to consider when processing heat sensitive materials.

The gas temperature in the spout channel was computed from Equation 4.3. The resulting calculated outlet gas temperature above the fountain was compared to the two measured air outlet thermocouple readings, $T_{g,out}$. Over the 60 second test a maximum error of 4.5% existed between the computed outlet gas temperature and the experimentally measured $T_{g,out}$. The difference could be due to energy lost, the assumptions made in Equation 4.3, or that the two thermocouples used for $T_{g,out}$ only measure temperature at two discrete points. To compare the gas and particle temperature distribution in the spouted regime per bed height, the instantaneous measured particle temperatures and computed gas temperatures are expressed in a non-dimensional term:

$$\theta_{gp} = \frac{T - \min(T_{p,s}, T_g)}{\max(T_{p,s}, T_g) - \min(T_{p,s}, T_g)} \quad (5.1.3)$$

A 60 second mean temporal distribution per bed height is given in Figure 9 for the air and particulates in the spouted study. The high rate of energy lost from the bed to the wall (Brown and Lattimer, 2012b), increasing spouting diameter (Brown and Lattimer, 2012a), and high solid circulation rate in the spouted bed produced an increase in the particle temperature just above the

gas inlet. The particle temperature distribution, of Figure 9, is then seen to gradually drop with increasing height into the bed. In addition to the previously discussed three-dimensional mixing effects, the decrease in particle temperature is attributed to two additional observations. The first is the annulus surrounding the spout channel act as a heat sink to the spouting gas. Energy is lost from spout as the gas flares into the annulus (Epstein and Mathur, 1971). The second reason comes from the continuous addition of lower temperature particles being feed to the spout channel from the annulus. With further height up the spouted bed, the mean particle temperature is found to increase again due to the high particle temperatures in the annulus.

A global maximum in the particle temperature is observed at the top of the bed. Here the width of the spout channel decreases at the top of the annulus (Brown and Lattimer, 2012a). The denser bulk solid fraction, ($\varepsilon_s = 1 - \varepsilon_f$), zone is associated with the solid entrainment of the annulus (Day et al., 1987). Additionally, hot particle are also present at the top of the annulus as they are entrained from the spout channel, to the fountain, and back to the top of the annulus.

A local minimum in the spout particle temperature again occurs at the base of the fountain in Figure 9. As the particles move to the core of the fountain they temporarily become stagnant due to the change in the vertical velocity direction. The spout channel gas can then directly impinge on the suspended particle clusters. A resulting local maximum of particle temperature is observed at the fountain core and then lowers towards the top of the fountain.

Gas temperature in the spout channel steadily decreased with bed height, shown in Figure 9. The spouted bed effectively exchanges heat between the gas and the particle due to the high surface area of the particles present. In addition, the particles act as a heat sink to the inlet gas due to their relative high heat capacity. As a result the spouting gas follows the temperature of the particles. The overall bed temperature in the spout channel has also been reported to decrease with height in an experimental study using a heated inlet gas source (Malek and Lu, 1964). This again was confirmed in a more recent study using mesh covered thermocouples. Freitas and Freire (2001) concluded that the air temperature drops significantly with axial height in a bottom solid feed spouted bed.

5.2 Energy Stored

When processing heat sensitive materials in a fluidized or spouted bed it is important to know the regions with high and low rates of energy stored. These rates are given in terms of the

intra-particle temperature changes, expressed in Equation 4.2. Over the full bed, the mean error between Equation 4.2 and 4.1 was expressed as:

$$Error = \frac{\dot{E}_{gb} - \dot{E}_p}{\dot{E}_{gb}} \times 100 \quad (5.2.1)$$

Good agreement was found between the two equations with a mean error of 6.8%. The instantaneous energy stored in the particles of the fluidized regime, expressed through Equation 4.2, is shown in Figure 10 over a time span of 2 to 5 seconds. Particle temperature fluctuations in the dead-zones are minimal and therefore did not have a significant impact on the energy stored term. The large surface area of the non-stagnant particles allows for increased heat exchange rates. Higher void fractions are present in the gas channel over the downward moving zones of the fluidized bed (Brown and Lattimer, 2012a). A resulting lower total surface area of the particles exists in the gas channel, making the moving zone the largest contributor to the energy stored term. Gas-to-particle heat transfer rates decrease with lower heights in the moving zones. The increased moving zone residence time and increased bulk solid fraction allowed for gas and particle temperatures to approach near unity.

Increasing the inlet gas velocity to $3 u_{mf}$ lead to the spouting regime in Figure 11. The highest rates of energy stored in the particles near the NaCl window were identified at the top of the annulus and along the spout-annulus border. The high bulk fraction of particles at the spout-annulus border is directly heated by the hot inlet spouting gas. Typically the distance for the gas to travel is on the order of centimeters (Guo et al., 1996) to achieve thermal equilibrium with the solids in the annulus region.

Turbulent mixing was induced by the fountain and resulted in increases particle heat transfer. Additionally, the gas directly impinges upon the temporarily stagnant particle clusters in the fountain core. Particles then follow the parabolic trajectory from the core to the periphery, returning to the surface level of the bed. Here the accumulated particles lead to high bulk solid fractions, and thus increased rates of energy stored.

5.3 Gas-to-Particle Heat Transfer

The spouted bed contains a spout channel where large quantities of gas directly flow through the bed. In some instances, portions of the gas may not come into particle contact. This can be a disadvantage in many applications, but can also be desirable in processes which require

high gas-to-particle exchange rates with low gas residence time. The heat transfer coefficient in the spouted bed per unit height was computed through Equation 4.4. It has been previously shown that the heat transfer coefficient has low independence on the inlet gas temperature (Malek and Lu, 1964; Prachayawarakorn et al., 2006). Furthermore, the bulk solid fraction distribution used in this study was based off the 10 second average finding of Brown and Lattimer (2012a). As a result, the instantaneous calculations of Equation 4.4 were time averaged per one minute to show a generalized heat transfer coefficient distribution.

5.3.1 Heat Transfer Coefficients

The computed gas-to-particle heat transfer coefficients in the spout regime per bed height are shown in Figure 12. High heat transfer rates were achieved in the non-stagnant particulate zones due to the large surface area per unit mass of fluidized particles. The given heat transfer coefficients can seem rather small, as they are based on the large total particle surface area. A near steady heat transfer coefficient of 3 to 4 $\text{Wm}^{-2}\text{K}^{-1}$ is observed in Figure 12 from the gas inlet to about half way up the spout channel. At a further axial position, an increase in h_{gp} is observed from the enlarged heat flux rates in the annulus and the reducing temperature difference between the gas and particles. The heat transfer coefficient continues to increase with bed height, as particles continue to entrain from the annulus back into the spout channel.

Above the spout opening at the top of the annulus, turbulent mixing occurs as the particles are propelled into the freeboard. The solids accumulate in the fountain with the highest bulk solid fraction found in the fountain core (Brown and Lattimer, 2012a). As previously discussed, the spout gas directly impinges upon the temporarily stagnant particle clusters in the fountain core. A high heat flux was observed and the temperature difference between the gas and solids became minimal. As a result the highest heat transfer coefficient was observed at the fountain core. A maximum heat transfer coefficient of 17.3 $\text{Wm}^{-2}\text{K}^{-1}$ is shown Figure 12 at the fountain core. At a further increase in axial height, h_{gp} drops towards the top of the fountain and returns to zero in the freeboard region past the height of the spouted particulates.

5.3.2 Heat Transfer Correlations

The heat transfer measurement technique presented in this study was non-intrusive and provided detailed heat transfer coefficients per spout axial position. In an attempt to compare this study with the average gas-to-particle empirical heat transfer coefficient correlations found in

literature, an integrated average difference in h_{gp} of $9.0 \text{ Wm}^{-2}\text{K}^{-1}$ and the lower spout region heat transfer coefficient of $3.2 \text{ Wm}^{-2}\text{K}^{-1}$ was used.

An early study on a slurry-sprayed spouted bed was performed by Romankow and Rashkovskaya (1968). Glass particles with diameters ranging from 2 to 5 cm were sprayed with a slurry layer and spouted with air. The drying rate of the particles was used with a log mean temperature difference between the dry and wet bulb thermocouples, located at the inlet and outlet of the bed, to evaluate the heat transfer coefficient. Uemaki and Kugo (1968) used a similar approach in an 80 mm and 100 mm diameter column spouted bed. The drying rate of silica gel particles were spouted with air at $50 \text{ }^\circ\text{C}$. A log mean temperature difference was also applied to evaluate the water vapor in the air and particles. Both studies gives empirical correlations but are based off of air-water terms which cannot be properly applied to this study.

A more recent study used a continual through feed of paddy, soybean, and corn in a 600 mm wide pseudo 2-D spouted bed (Prachayawarakorn et al., 2006). The inlet gas was pre-heated in the range of 130 to $150 \text{ }^\circ\text{C}$, and a log mean temperature difference was applied to compute separate overall heat transfer coefficient in the spout and the annulus region. The study resulted in a Nusselt number correlation for each region, but again was unsuitable for comparing to this study as a much higher Reynolds number,

$$Re_i = \frac{u_i D_p \rho_g}{\mu_g} \quad (5.3.1)$$

was investigated in their study. Another study by Uemaki and Kugo (1967) also used a continual through feed of particle in a 92 mm cylindrical spouted bed. Particle diameters ranging from 1 to 4 mm were spouted with inlet air at $70 \text{ }^\circ\text{C}$. A log mean temperature difference was used to obtain heat transfer values range from 3.4 to $17 \text{ Wm}^{-2}\text{K}^{-1}$, and an empirical correlation was defined as:

$$Nu = 0.0005 Re_{ms}^{1.46} \left(\frac{u}{u_{ms}} \right) \quad (5.3.2)$$

where $u_{ms} (\text{ms}^{-1})$ is the minimum spouting velocity, the Reynolds number was defined at u_{ms} , and $\mu_g (\text{kg m}^{-1}\text{s}^{-1})$ in the Reynolds number is the gas dynamic viscosity. Applying Equation 5.3.2 to the spouting study of Figure 12, a resulting average heat transfer coefficient of $1.95 \text{ Wm}^{-2}\text{K}^{-1}$ is obtained. This value was found to under predict the heat transfer coefficients in this

study. A similar finding was also noted by Kmiec (1975), who performed similar experimental tests in a spouted bed.

A column diameter of 90 mm with a conical base angle, γ ($^\circ$), ranging from 30 to 90 $^\circ$ was studied by Kmiec (1975). Silica gel and activated coal particles, with diameters between 0.27 to 3.31 mm, were spouted with an inlet gas temperature of 50 $^\circ\text{C}$. A log mean temperature difference was applied with wet and dry bulb thermocouples. A resulting dimensionless analysis, similar to Romankow and Rashkovskaya (1968), was derived but neglected the water vapor terms, and is defined as:

$$Nu = 0.897 Re_u^{0.464} Pr^{0.333} Ar^{0.116} \left(tg \frac{\gamma}{2} \right)^{-0.813} \left(\frac{H_o}{D_p} \right)^{-1.19} \phi_s^{2.261} \quad (5.3.3)$$

Parameter, H_o (m), is the stagnant bed height, Pr is the Prandtl number, and Ar is Archimedes number:

$$Ar = g D_p^3 (\rho_p - \rho_g) \rho_g \mu_g^{-2} \quad (5.3.4)$$

The bed investigated in this study was flat bottomed without a conical base. If the conical base angle term of Equation 5.3.3 was neglected, a computed heat transfer coefficient of 2.3 $\text{Wm}^{-2}\text{K}^{-1}$ is found. However the large stagnant area of the dead-zones act similar to a conical shaped bed. A dead zone angle, γ_{dz} , of 60.56 $^\circ$ was defined from the PIV study of Brown and Lattimer (2012a). Applying this angle to Equation 5.3.3 a heat transfer coefficient of 3.5 $\text{Wm}^{-2}\text{K}^{-1}$ is computed. The range of values found from accounting for and neglecting the conical angle in Equation 5.3.3 was in close agreement with the near inlet region heat transfer coefficients, of 3.2 $\text{Wm}^{-2}\text{K}^{-1}$, found in this study.

The higher heat transfer coefficients in the fountain region of Figure 12 have not been reported in literature. Many experimental studies are based on an average steady-state value from a log mean temperature difference. Numerical thermal models have also been developed by Kmiec (1980) but neglect the fountain region and only focus on the spout and the annulus. The highly turbulent mixing between the spouting gas and particles provided an increased convective heat transfer coefficient in the fountain. In addition, spout swaying also occurs from the lack of commonly used in bed stabilizers (He et al., 1994). As a result, the fountain better represents a highly turbulent fluidized bed. It was been well noted in literature that fluidized beds have higher heat transfer coefficient than spouted bed (Chatterjee et al., 1983; Klassen and Gishler, 1958;

Malek and Lu, 1964) due to increased gas-particle residence times. In addition, shallower beds have also been found to have higher Nusselt numbers (Kmieć, 1975; Prachayawarakorn et al., 2006).

An empirical correlation for the maximum Nusselt number was given by Pillai (1976) in a shallow fluidized bed from immersing thermocouples into particle spheres. Based off the given correlation:

$$Nu_{max} = 0.365 \left(\frac{T_{bd}}{273} \right)^{0.82} Ar^{0.22} \quad (5.3.5)$$

a maximum Nusselt of 1.14 could result in a shallow fluidized bed under the spouting conditions given in this study; where T_{bd} (K) is the absolute bed temperature. Additionally, Molerus (1993) reported on a maximum gas convective Nusselt number for different solid particles (glass, quartz, bronze, and polystyrene) containing different thermal properties. For an Archimedes number of 800, smaller than the value investigated in this study, Molerus (1993) gave a value of Nu_{max} equal to 1.2.

The two discussed maximum Nusselt number correlations are based off of bubbling fluidized beds and not a spouting regime, but go to help define an upper Nusselt number limit for the increased fountain heat transfer coefficients of Figure 12. The data found in this study should be applied with caution to the above empirical spouted bed correlations, as a two-dimensional flat bottomed spouted bed was investigated in comparison to the typical steady-state cylindrical column found in literature.

6. Conclusion

Gas-to-particle heat transfer characteristics were studied in pseudo two-dimensional fluidized, spouted, and fixed beds. A non-intrusive, high spatial resolution, and time varying experimental measurement technique was applied to capture detailed data need for Discrete Particle Model validations. The analysis was not limited to a single overall gas-to-particle heat transfer coefficient often found in a steady-state analysis. Instead, full field views of transient particle temperature distribution were successfully captured, along with distribution rates of energy stored in the particles. The highest rates of energy, resulting from intra-particle temporal changes, were found in the downward entrainment of particulates in the annulus zone surrounding the spout channel. A differential equation was derived to compute the cross-

sectional average gas temperature per spouting bed height, and was applied to calculate gas-to-particle heat transfer coefficients. The heat transfer coefficients found in the lower portion of the spouted bed were in close comparison to the empirical correlation of Kmiec (1975) when using the angle of the dead-zones to define the conical spouted bed angle. The infrared thermography measurement technique captured new gas-to-particle heat transfer data in the spouting fountain with increased spatial resolution. Here the highest convective heat transfer coefficients were found at the core of the fountain as a result of its highly turbulent mixing nature, and further due to periodic unstable spout swaying.

Acknowledgements

The authors are grateful for the support from the Virginia Tech Institute for Critical Technology and Applied Science (ICTAS).

References

- Agarwal, G., Lattimer, B., Ekkad, S., Vandsburger, U., 2011. Influence of multiple gas inlet jets on fluidized bed hydrodynamics using Particle Image Velocimetry and Digital Image Analysis. *Powder Technol.* 214, 122-134.
- Baeyens, J., Goossens, W.R.A., 1973. Some aspects of heat transfer between a vertical wall and a gas fluidized bed. *Powder Technol.* 8, 91-96.
- Brown, S., Lattimer, B., 2012a. Experimental hydrodynamics of multiple jet systems in a fluidized and spouted bed. (Manuscript submitted for publication). *Int. J. Multiph. Flow.*
- Brown, S., Lattimer, B., 2012b. Transient bed-to-wall heat flux measurements in fluidized and spouted beds. (Manuscript submitted for publication). *International Journal of Heat and Mass Transfer.*
- Chatterjee, A., Adusumilli, R.S.S., Deshmukh, A.V., 1983. Wall-to-Bed Heat-Transfer Characteristics of Spout-Fluid Beds. *Can J Chem Eng* 61, 390-397.
- Day, J.Y., Morgan, M.H., Littman, H., 1987. Measurements of spout voidage distributions, particle velocities and particle circulation rates in spouted beds of coarse particles—II. Experimental verification. *Chem Eng Sci* 42, 1461-1470.
- Englart, S., Kmiec, A., Ludwinska, A., 2009. Heat Transfer in Sprayed Spouted Beds. *The Canadian Journal of Chemical Engineering* 87, 185-192.

- Epstein, N., Mathur, K.B., 1971. Heat and mass transfer in spouted beds - A review. *The Canadian Journal of Chemical Engineering* 49, 467-476.
- Freitas, L.A.P., Freire, J.T., 2001. Heat transfer in a draft tube spouted bed with bottom solids feed. *Powder Technol.* 114, 152-162.
- Guo, Q., Zhang, J., Luo, G., 1996. Porosity Distribution in Two-dimensional Fluidized Bed with a Jet. *Chemical Industry and Engineering* 13, 14-19.
- Hamzehei, M., Rahimzadeh, H., 2009. Experimental and Numerical Study of Hydrodynamics with Heat Transfer in a Gas-Solid Fluidized-Bed Reactor at Different Particle Sizes. *Industrial & Engineering Chemistry Research* 48, 3177-3186.
- He, Y.L., Lim, C.J., Grace, J.R., Zhu, J.X., Qin, S.Z., 1994. Measurements of Voidage Profiles in Spouted Beds. *Can J Chem Eng* 72, 229-234.
- Incropera, F.P., DeWitt, D.P., 2002. *Fundamentals of heat and mass transfer*. J. Wiley, New York.
- Klassen, J., Gishler, P.E., 1958. Heat transfer from column wall to bed in spouted fluidized and packed systems. *The Canadian Journal of Chemical Engineering* 36, 12-18.
- Kmieć, A., 1975. Simultaneous heat and mass transfer in spouted beds. *The Canadian Journal of Chemical Engineering* 53, 18-24.
- Kmieć, A., 1980. *Hydrodynamics of Flows and Heat Transfer in Spouted Beds*. *The Chemical Engineering Journal* 19, 189-200.
- Malek, M.A., Lu, B.C.Y., 1964. Heat transfer in spouted beds. *The Canadian Journal of Chemical Engineering* 42, 14-20.
- Molerus, O., 1993. Arguments on heat transfer in gas fluidized beds. *Chem Eng Sci* 48, 761-770.
- Petrovic, L.J., Thodos, G., 1968. Effectiveness factors for heat transfer in fluidized beds. *The Canadian Journal of Chemical Engineering* 46, 114-118.
- Pillai, K.K., 1976. Heat transfer to a sphere immersed in a shallow fluidized bed. *Letters in Heat and Mass Transfer* 3, 131 - 146.
- Prachayawarakorn, S., Ruengnarong, S., Soponronnarit, S., 2006. Characteristics of heat transfer in two-dimensional spouted bed. *Journal of Food Engineering* 76, 327-333.
- Romankow, P.G., Rashkovskaya, N.B., 1968. *Drying in a Suspended State*. Chem. Publ. House, Leningrad, Russia.
- Uemaki, O., Kugo, M., 1967. Heat transfer in spouted beds. *Kagaku Kagaku* 31, 348-355.

Uemaki, O., Kugo, M., 1968. Mass transfer in a spouted bed. *Kagaku Kagaku* 32, 895.

Yusuf, R., Halvorsen, B., Melaaen, M.C., 2012. An experimental and computational study of wall to bed heat transfer in a bubbling gas–solid fluidized bed. *Int. J. Multiph. Flow* 42, 9-23.

Figures and Tables

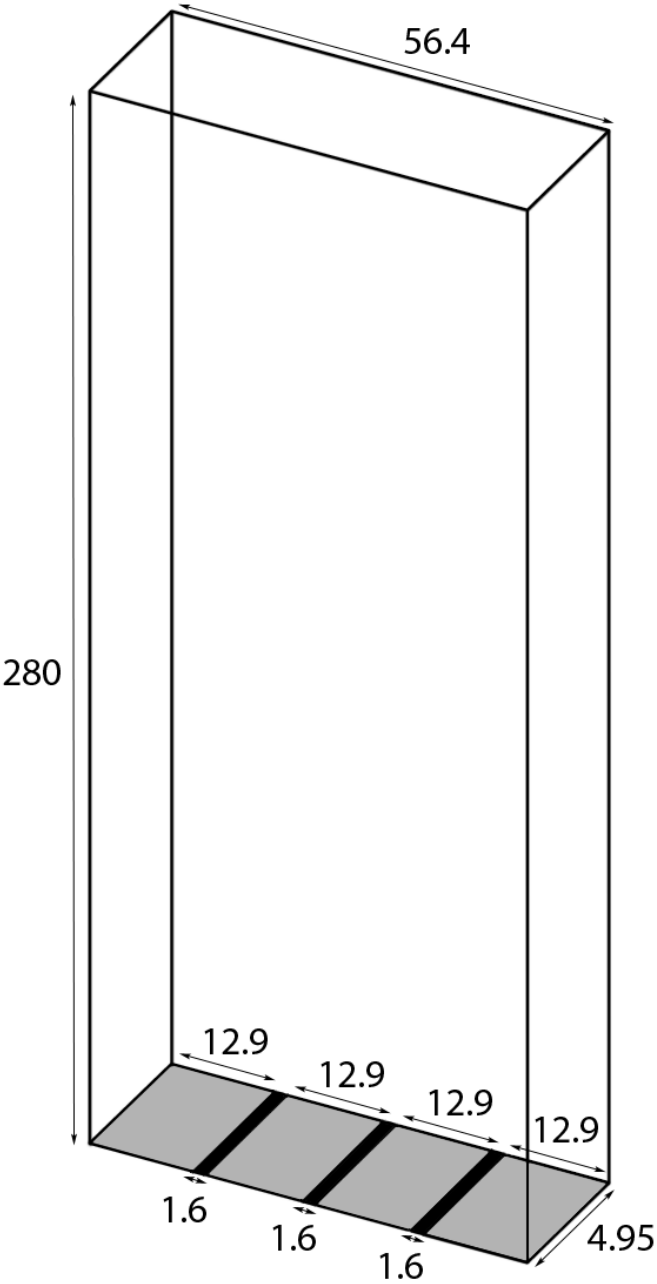


Figure 1: Schematic of the 2-D flat bottom rectangular column setup with dimensions in mm.

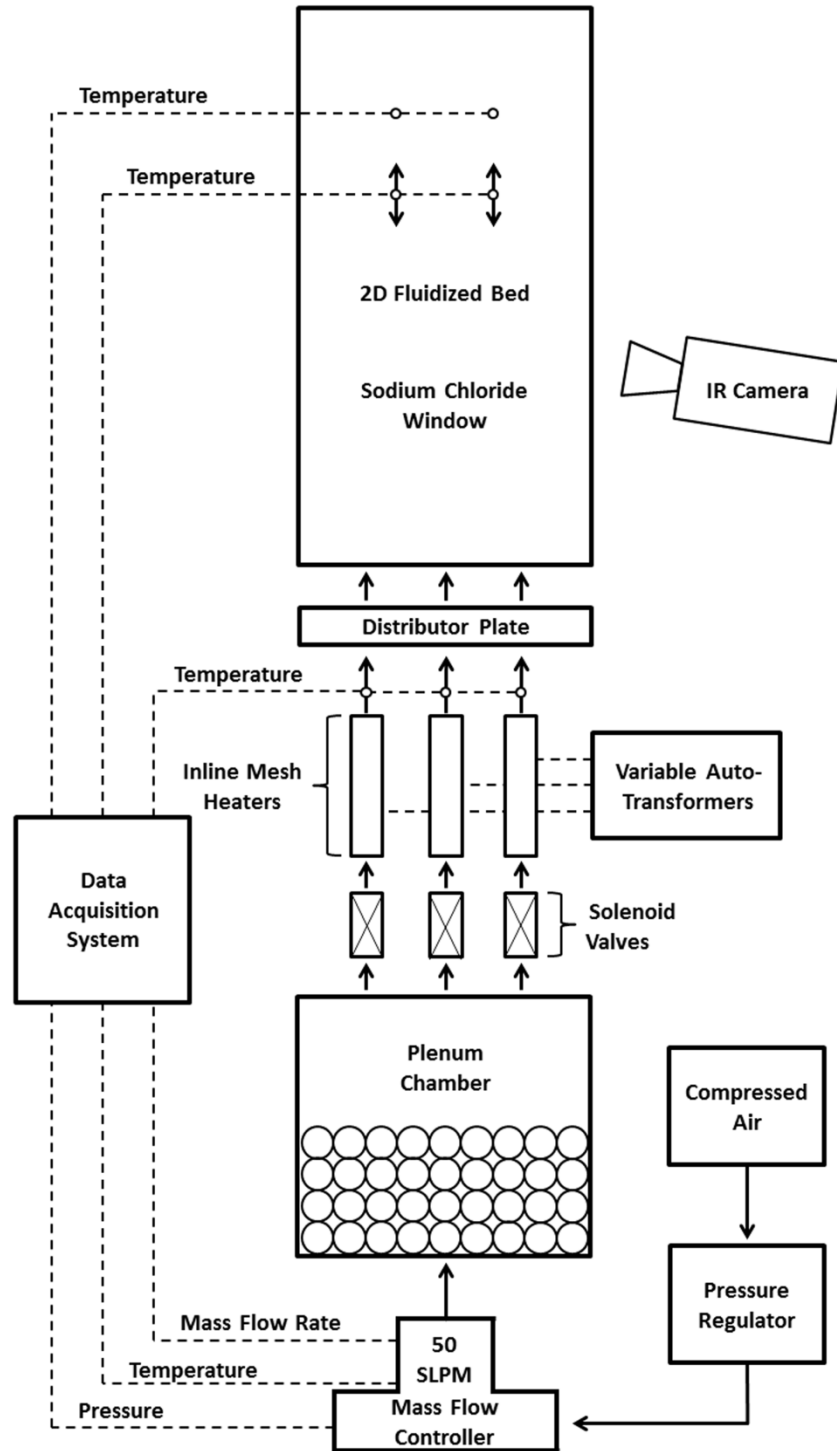


Figure 2: Diagram of the experimental setup.

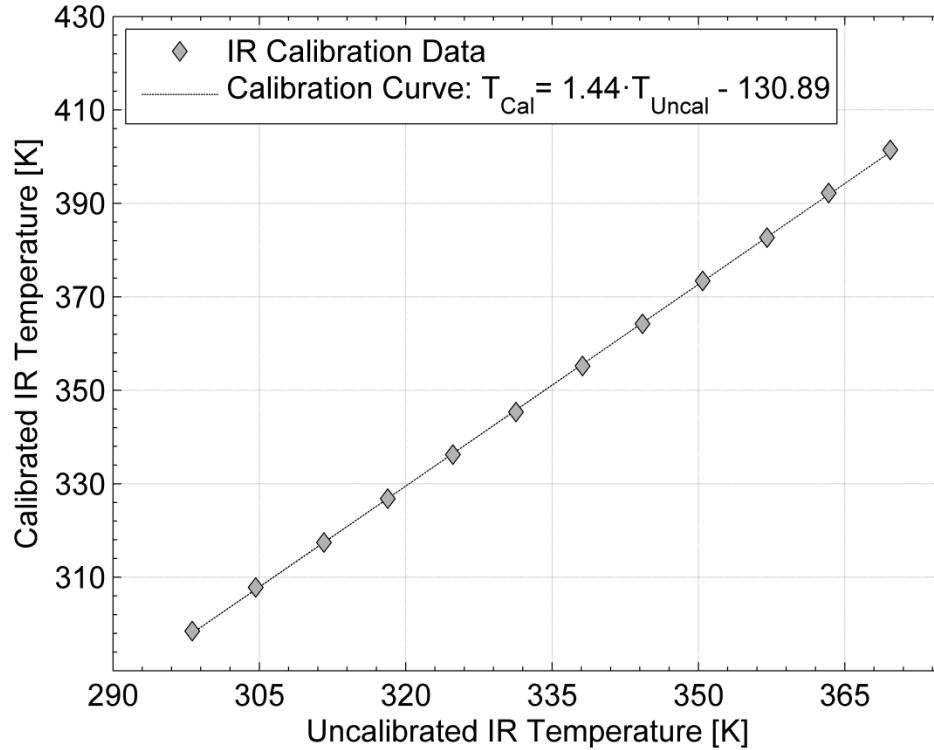


Figure 3: Infrared camera calibration curve for the coupled particle emissivity and transmission of the sodium chloride optical window.

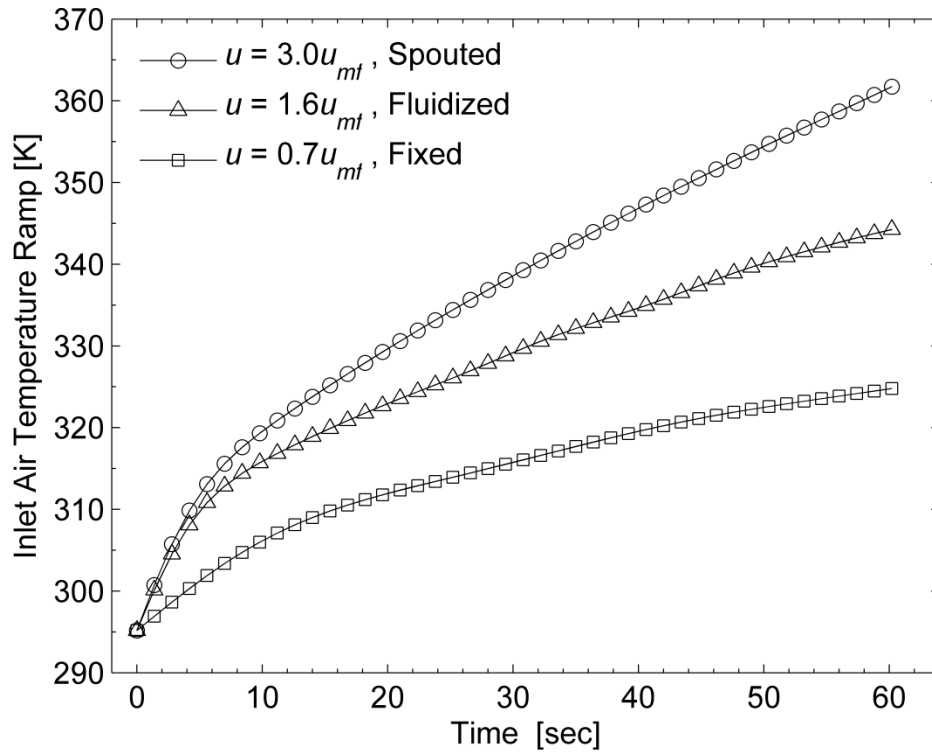


Figure 4: Transient inlet air temperature ramp for the spouted, fluidized, and fixed bed regimes.

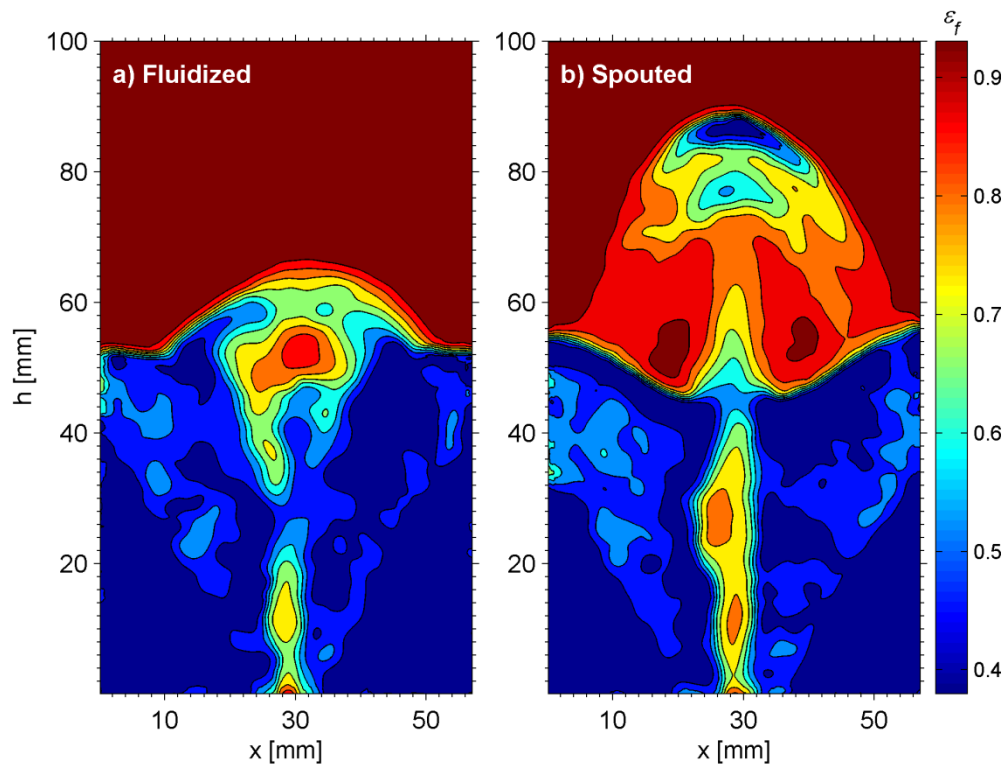


Figure 5: Instantaneous void fraction data for the a) fluidized, and b) spouted regime.

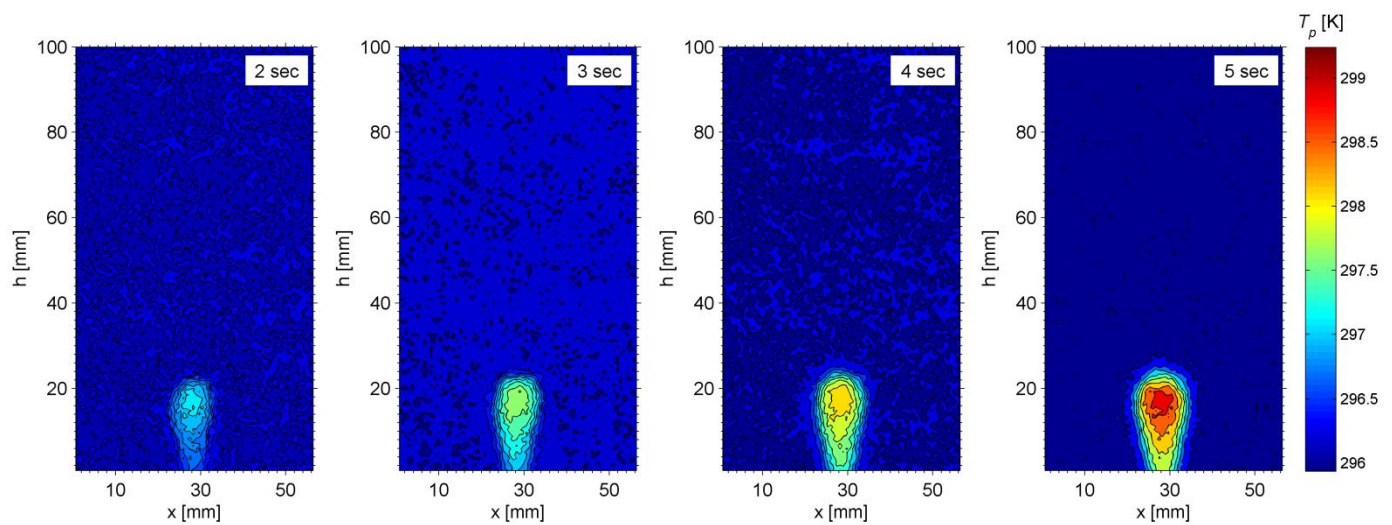


Figure 6: Instantaneous particle time line temperature distribution in a fixed bed with an internal spout at $0.7 u_{mf}$.

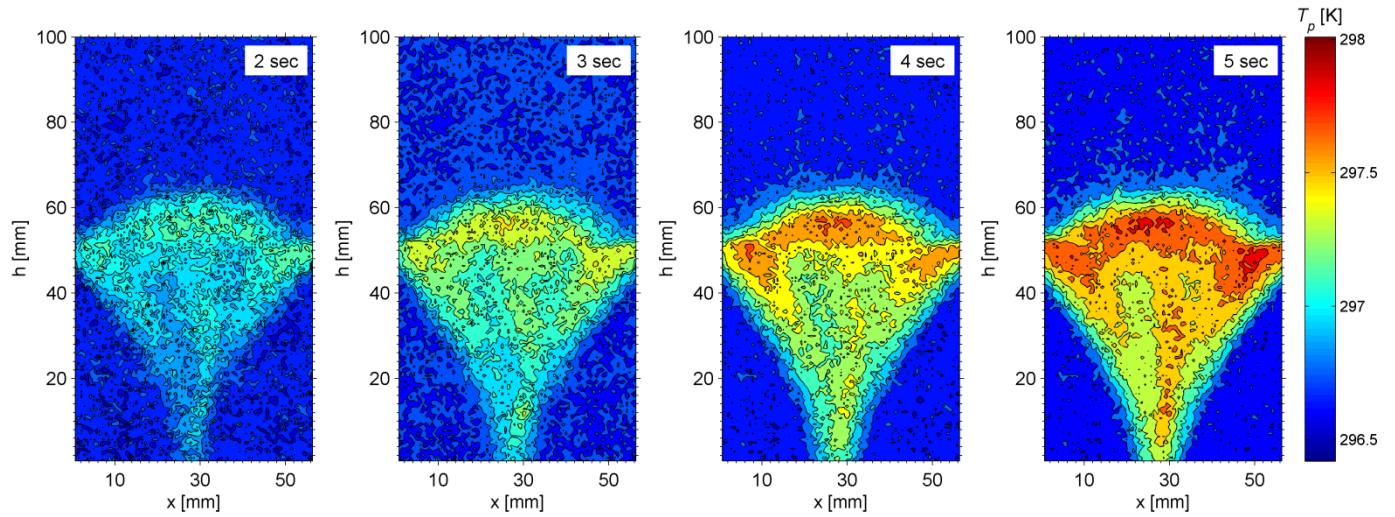


Figure 7: Instantaneous particle time line temperature distribution in a fluidized bed at $1.6 u_{mf}$.

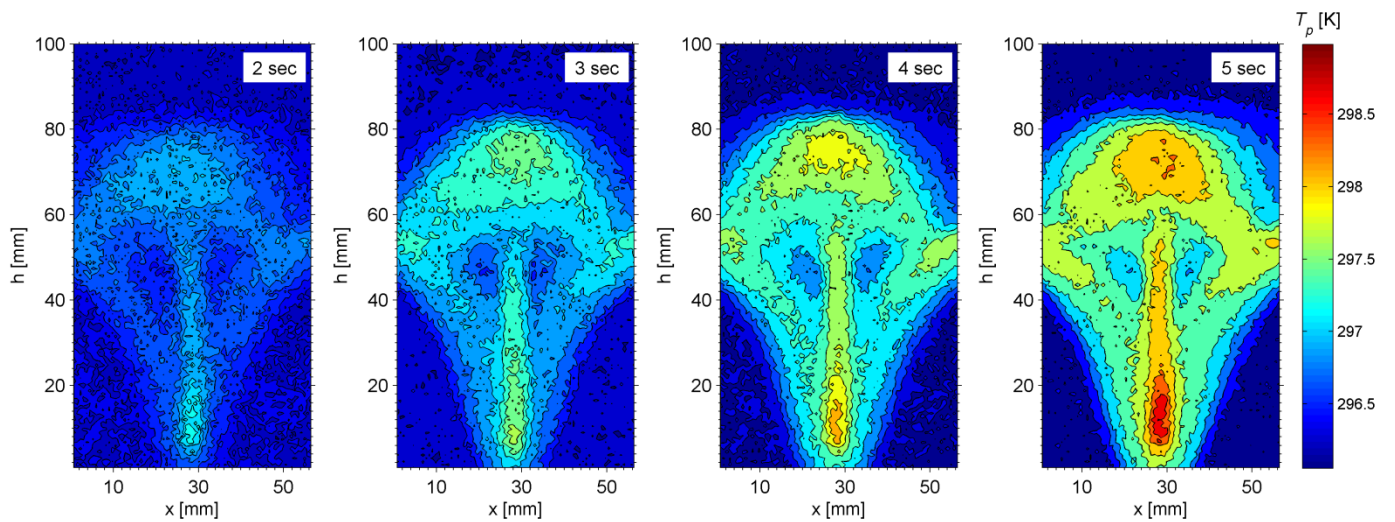


Figure 8: Instantaneous particle time line temperature distribution in a spouted bed at $3.0 u_{mf}$.

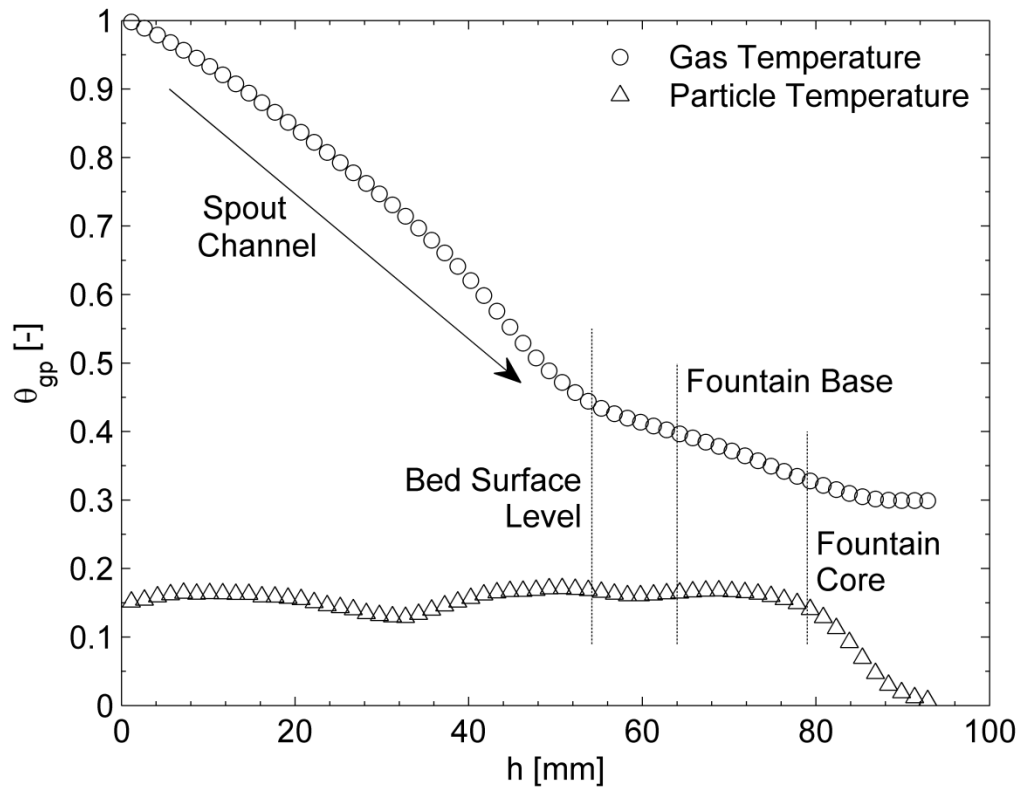


Figure 9: 60 second time averaged dimensionless gas and particle temperature distribution in the spouted bed at $3.0 u_{mf}$.

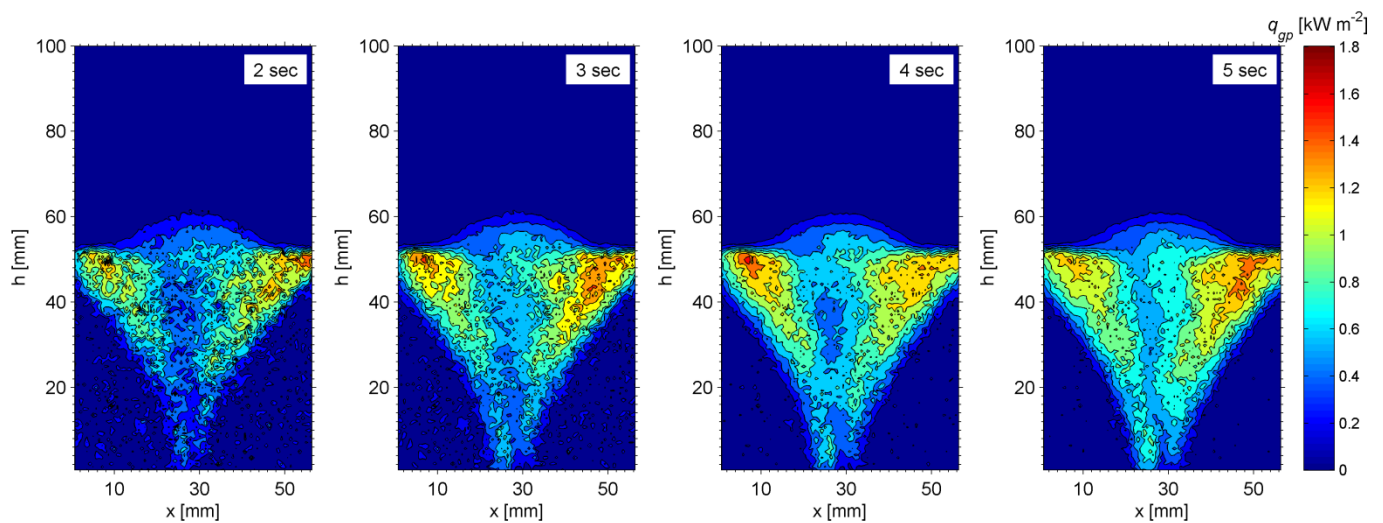


Figure 10: Instantaneous rates of energy stored in the particles under a fluidized regime at $1.6 u_{mf}$.

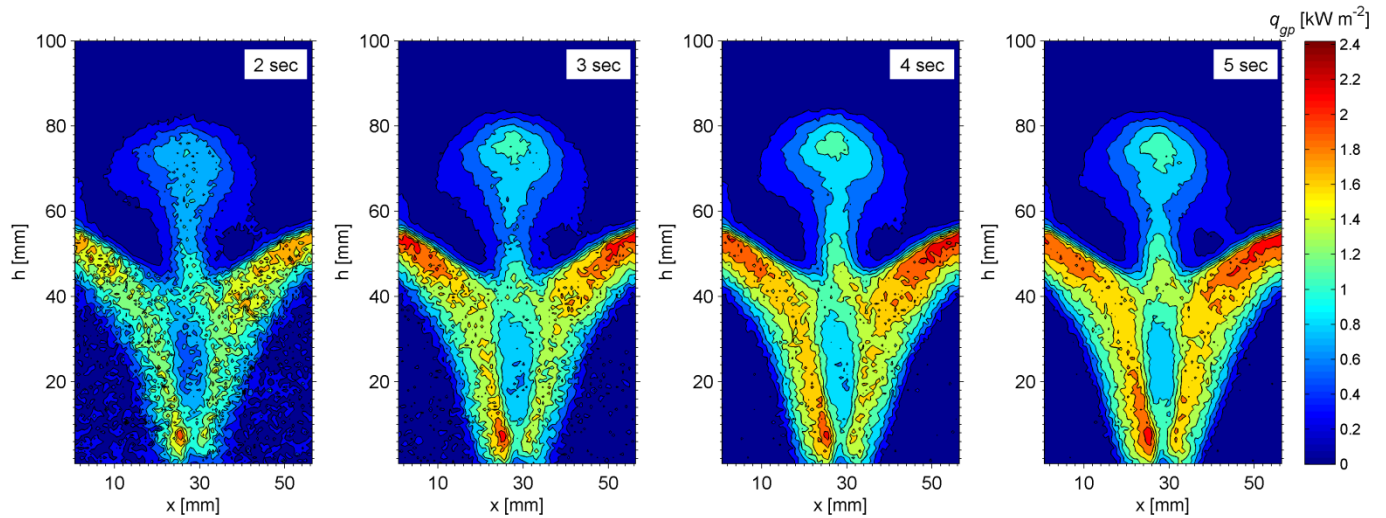


Figure 11: Instantaneous rates of energy stored in the particles under a spouted regime at 3.0

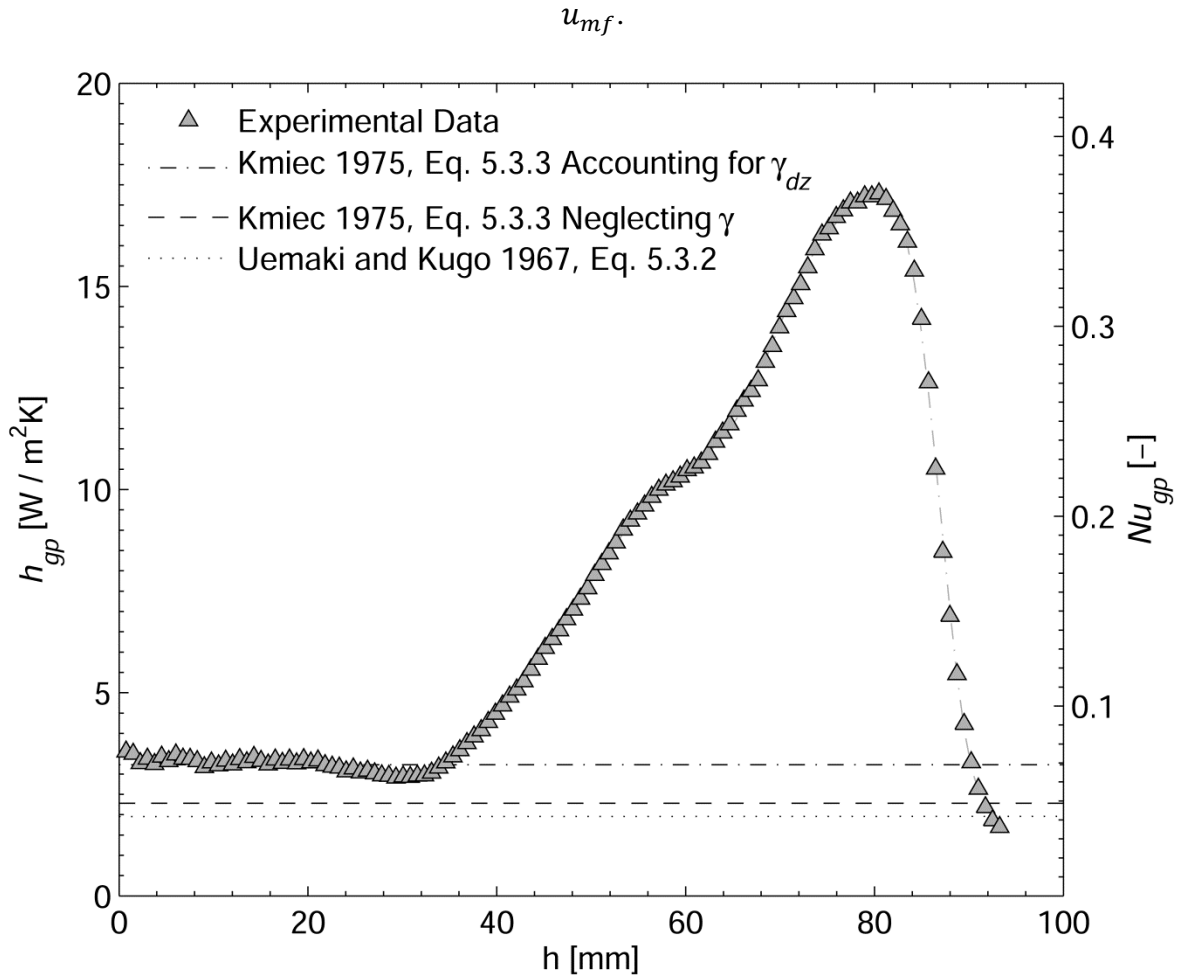


Figure 12: 60 second time averaged gas-to-particle heat transfer coefficients per axial cross-sectional height in a spouted regime at 3.0 u_{mf} .

Table 1: Properties of experimental fluidized bed media.

Property	Particles
Geldart Group	B
Number of Particles	100,000
D_p [μm]	550
ρ_p [kg m^{-3}]	2500
ϕ_s [-]	1
u_{mf} [m s^{-1}]	0.24
H_0 [mm]	49.75
k_p [$\text{Wm}^{-1}\text{K}^{-1}$]	1.05
$c_{p,p}$ [$\text{kJ kg}^{-1}\text{K}^{-1}$]	0.84

Chapter 5

Conclusions and Recommendations

1. Conclusions

The hydrodynamics and heat transfer characteristics of gas-solid fluidization were studied in a small scaled laboratory fluidized bed. The gas-solid dynamics of a multiple jet system were captured through three non-intrusive measurement techniques, viz. Particle Image Velocimetry (PIV), Digital Image Analysis (DIA), and pressure drop spectral analysis. The effects of inlet gas flowrate, Geldart B and D classified particle types, and multiple jet systems were investigated.

The frequency analysis of the differential pressure signal resulted in the classification of four difference flow regimes: Fixed Bed, Internal Spout, Jet Fluidized, and Jet Spouting. Coupling PIV with DIA revealed that an increase in particulate size resulted in increasing jet diameters, solid circulation rates, and increased spouting fountain heights due to the enlarged momentum exchange rates. Contrary to the typical notion, gas void fractions found in the annulus of a spouted bed were found higher than a loosely packed bed. Additionally, the common assumption of implementing additional jets into a fluidized bed did not always directly pertain to a decrease in the total bed dead zones due to jet merging effects.

A novel experimental procedure was introduced to quantifying transient bed-to-wall heat transfer characteristics of the multiple jet system. The technique used an Infrared (IR) camera and applied an Inverse Heat Conduction Problem (IHCP). The procedure was developed to overcome the spatial, time varying, and instrumental intrusive limitation often found in multiphase flow heat transfer experiments. Attention was paid to the amplified noise of the IR camera measurements through applying a discrete analysis to the two-dimensional Laplacian of Fourier's law. The effects of added high emissivity paint in IHCP were found to significantly impact the rates of energy stored at the wall, while the impact on Fourier's law was not substantial. The analysis exposed jet interaction, spout fountain heat flux profiles, and enlarged gas inlet thermal gradients for increased particle size. The dominant source of bed-to-wall heat transfer was found from the convection of the inlet gas and the downward entrainment of solid particles.

An innovative, yet simple gas-to-particle heat transfer measurement techniques was also established. Infrared thermography was applied to capture near wall full field maps of transient particle temperature distributions in the 2-D fluidized bed. The highest rates of energy stored in the particles were identified along the downward particulate entrainment zones surrounding the inlet gas channel. A discrete differential equation was derived to compute the gas temperature in

a spouted bed. The high heat capacity of the solids caused the bed to act as a heat sink to the incoming heated inlet gas. As a result the temperature of the gas was forced to closely follow the temperature of the particles. Cross-sectional averaged gas-to-particle heat transfer coefficients were found per bed height. The resulting detailed data provided increased spatial resolution to the typical analysis for acquiring a single overall gas-to-bed heat transfer coefficient often found in literature. The heat transfer coefficients found in the lower portion of the spout were in close comparison to the empirical correlations given in literature. However, new findings were obtained on the fountain region of the spouted bed. The highly turbulent mixing nature of the gas and solids, along with the period swaying of an unstable spout resulted in enlarge heat transfer coefficients at the top of the bed and the fountain region.

2. Recommendations

Fluidization in slit jet rectangular beds are not well established in literature in comparison to the conventional axisymmetric columns typically studied. Considerable work still remains to quantify the behaviors of these systems. Recommendations for future work include:

- Capturing of the three dimensional effects in a pseudo 2-D bed for the validation of Computational Fluid Dynamic models.
- Tracking of the gas velocity and gas flow distributions throughout the experimental bed.
- Quantifying the hydrodynamic and heat transfer effects of scaling up small scale laboratory sized beds.
- Comparing wall frictional effects between a fully three-dimensional bed to a pseudo two-dimensional fluidized bed.
- Studying the changes in the gas-solid hydrodynamics and heat transfer characteristics in a spouted bed containing in-bed spout stabilizers to a bed lacking stabilizers.
- Changing of the heat transfer boundary conditions between isothermal and constant heat flux distributions to compare with fully transient multiphase flow experiments.
- Measuring multiphase flow hydrodynamics and heat transfer characteristics simultaneously.
- Performing studies with pyrolysis in carbonaceous reacting beds.

- Examining segregation patterns of multi-dispersed particulates with various physical properties in fluidization.

Appendix A

Additional Figures

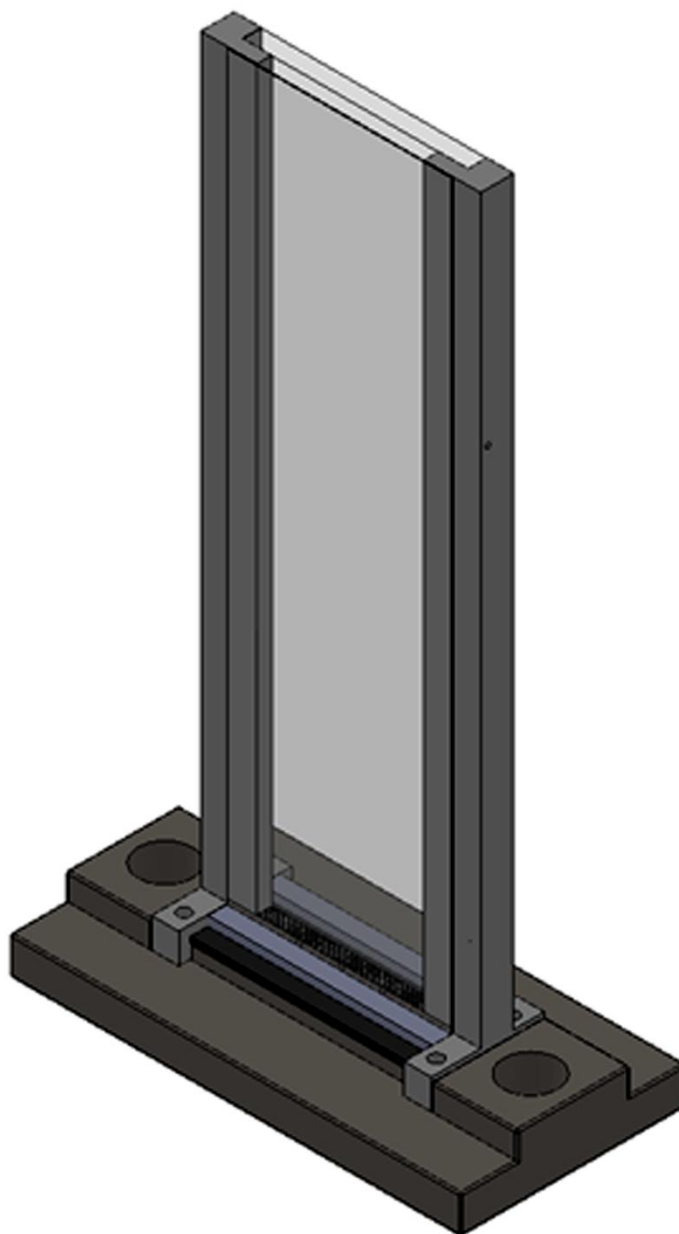


Figure 1: Three dimensional illustration of the pseudo 2-D experimental bed examined.

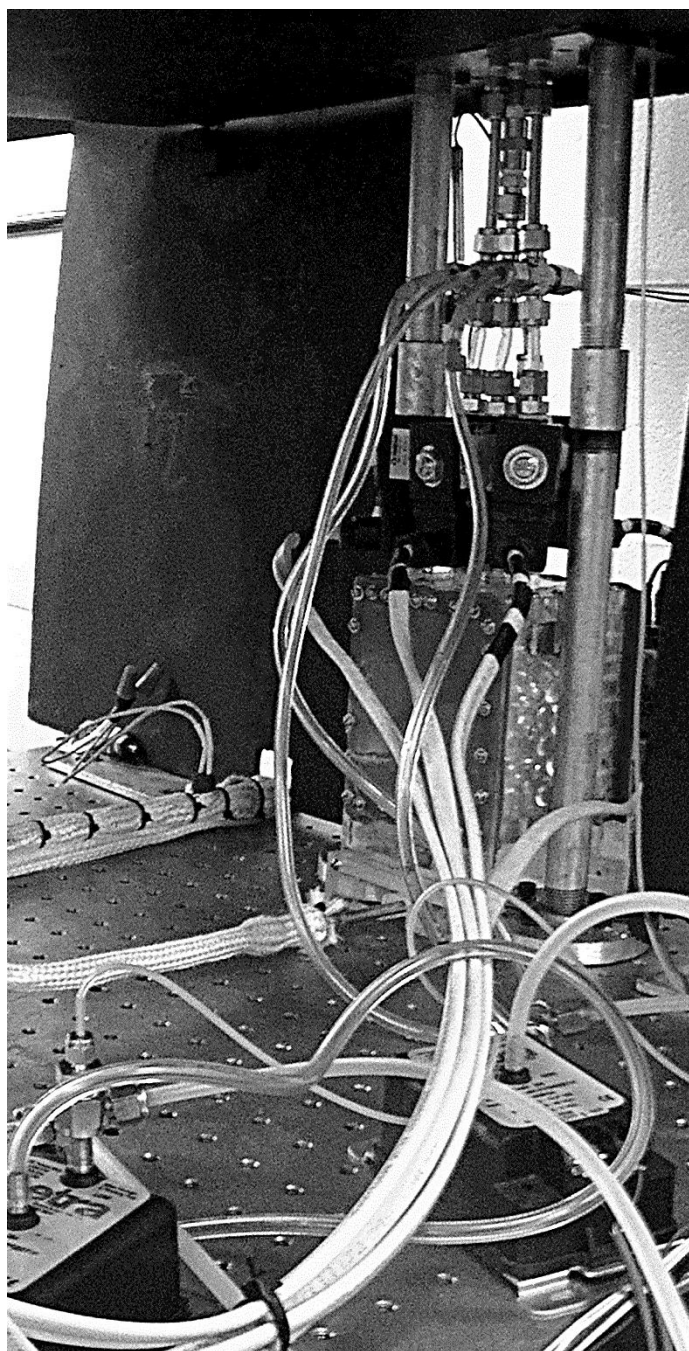


Figure 2: Image of the inlet gas distribution system used in the hydrodynamic experiments of Chapter 2.

Appendix B

Publications and Presentations

Chapter 2:

Brown, S., Lattimer, B., 2012. Experimental hydrodynamics of multiple jet systems in a fluidized and spouted bed. (Manuscript submitted for publication). *Int. J. Multiph. Flow*.

Brown, S., Lattimer, B., 2012. Hydrodynamics of multiple jet systems in a 2d gas solid fluidized bed, Proceedings of the ASME 2012 Fluids Engineering Summer Meeting. ASME, Rio Grande, Puerto Rico.

Chapter 3:

Brown, S., Lattimer, B., 2012. Hydrodynamics and heat transfer measurements of multiple jet systems in a 2d gas solid fluidized bed. (Abstract submitted), International Mechanical Engineering Congress and Exposition. ASME, Houston, TX.

Brown, S., Lattimer, B., 2012. Transient bed-to-wall heat flux measurements in fluidized and spouted beds. (Manuscript submitted for publication). *International Journal of Heat and Mass Transfer*.

Chapter 4:

Brown, S., Lattimer, B., 2012. Transient gas-to-particle heat transfer measurements in fluidized and spouted beds. (Manuscript submitted for publication). *Experimental Thermal and Fluid Science*.